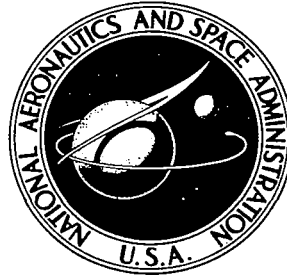


NASA
CR
1912
v.1
c.1



**NASA CONTRACTOR
REPORT**

NASA CR-1

NASA CR-1911

**LOAN COPY: RETURN
AFWL (DOUL)
KIRTLAND AFB, N.M.**



**DEVELOPMENT AND APPLICATION
OF A METHOD FOR PREDICTING
ROTOR FREE WAKE POSITIONS AND
RESULTING ROTOR BLADE AIR LOADS**

Volume I - Model and Results

by S. Gene Sadler

Prepared by
ROCHESTER APPLIED SCIENCE ASSOCIATES, INC.
Rochester, N. Y. 14618
for Langley Research Center

NATIONAL AERONAUTICS AND SPACE ADMINISTRATION • WASHINGTON, D. C. • DECEMBER 1971



0060967

1. Report No. NASA CR-1911		2. Government Accession No.		3. Recipient's Catalog No.	
4. Title and Subtitle DEVELOPMENT AND APPLICATION OF A METHOD FOR PREDICTING ROTOR FREE WAKE POSITIONS AND RESULTING ROTOR BLADE AIR LOADS VOLUME I - MODEL AND RESULTS				5. Report Date December 1971	
				6. Performing Organization Code	
7. Author(s) S. Gene Sadler				8. Performing Organization Report No. 69-11	
9. Performing Organization Name and Address Rochester Applied Science Associates, Inc. 140 Allens Creek Road Rochester, New York 14618				10. Work Unit No.	
				11. Contract or Grant No. NAS1-8448	
12. Sponsoring Agency Name and Address National Aeronautics and Space Administration Washington, D.C. 20546				13. Type of Report and Period Covered Contractor Report	
				14. Sponsoring Agency Code	
15. Supplementary Notes VOLUME II - PROGRAM LISTINGS is contained in NASA CR-1912, 1971.					
16. Abstract <p>Rotor wake geometries are predicted by a process similar to the startup of a rotor in a free stream. An array of discrete trailing and shed vortices is generated with vortex strengths corresponding to stepwise radial and azimuthal blade circulations. The array of shed and trailing vortices is limited to an arbitrary number of azimuthal steps behind each blade. The remainder of the wake model of each blade is an arbitrary number of trailing vortices. Vortex element end points were allowed to be transported by the resultant velocity of the free stream and vortex-induced velocities. Wake geometry, wake flow, and wake-induced velocity influence coefficients are generated by this program for use in the blade loads portion of the calculations.</p> <p>Blade loads computations include the effects of nonuniform inflow due to a free wake, nonlinear airfoil characteristics, and response of flexible blades to the applied loads. Computed wake flows and blade loads are compared with experimentally measured data. Predicted blade loads, response, and shears and moments are obtained for a model rotor system having two independent rotors. The effects of advance ratio, vertical separation of rotors, different blade radius ratios, and different azimuthal spacing of the blades of one rotor with respect to the other are investigated.</p>					
17. Key Words (Suggested by Author(s)) Rotor wake prediction Blade response prediction Free wake program Rotor wake flow			18. Distribution Statement Unclassified - Unlimited		
19. Security Classif. (of this report) Unclassified		20. Security Classif. (of this page) Unclassified		21. No. of Pages 123	22. Price* \$3.00

CONTENTS

	<u>Page</u>
SUMMARY	1
INTRODUCTION	2
SYMBOLS	4
ANALYSIS	9
Wake Geometry Model and Formulation	9
Blade Loads and Response Model and Formulation	17
Computer Program Description and Use	26
RESULTS AND DISCUSSION	28
Results of Preliminary Calculations	28
Full Mesh Wake Model Results	30
Modified Wake Model and Results	31
Wake Flow Results	35
Calculated Wake Geometries	37
Blade Loads and Response Results	42
CONCLUSIONS AND RECOMMENDATIONS	46
APPENDIX	48
REFERENCES	69
TABLES	71
FIGURES	77

DEVELOPMENT AND APPLICATION OF A METHOD FOR
PREDICTING ROTOR FREE WAKE POSITIONS AND
RESULTING ROTOR BLADE AIR LOADS
VOLUME I - MODEL AND RESULTS*

By S. Gene Sadler
Rochester Applied Science Associates, Inc.

SUMMARY

Rotor wake geometries were predicted by a process similar to the start-up of a rotor in a free stream. An array of discrete trailing and shed vortices is generated with vortex strengths corresponding to stepwise radial and azimuthal blade circulations. The array of shed and trailing vortices is limited to an arbitrary number of azimuthal steps behind each blade. The remainder of the wake model of each blade is an arbitrary number of trailed vortices. Vortex element end points were allowed to be transported by the resultant velocity of the free stream and vortex-induced velocities. Wake geometry, wake flow, and wake-induced velocity influence coefficients were generated by this program for use in the blade loads portion of the calculations.

Blade loads computations included the effects of nonuniform inflow due to a free wake, nonlinear airfoil characteristics, and response of flexible blades to the applied loads. The resulting nonlinear equations were solved by an iterative process to determine the distribution of blade shears, bending moments and twisting moments.

Computed wake flows and blade loads were compared with experimentally measured data. Predicted blade loads, response, and shears and moments were obtained for a model rotor system having two independent rotors. The effects of advance ratio, vertical separation of rotors, different blade radius ratios and different azimuthal spacing of the blades of one rotor with respect to the other were investigated.

Wake flow calculations indicate that the wake geometry model provides a satisfactory simulation of wake-induced flow near the rotor disk. Free wake geometry calculations indicate increasing distortion with decreasing advance ratio, intertwining of pairs of tip vortices for rotor systems with nonuniform azimuthal blade spacing, and more vortex-blade interactions than would be expected from a rigid wake model. Blade airload variations are generally consistent with wake geometry calculations, but do not show effects of vortex-blade interactions as might be displayed by a more detailed model.

* VOLUME II - PROGRAM LISTINGS is contained in NASA CR-1912, 1971.

INTRODUCTION

The prediction of rotor-induced aerodynamic flows has recently undergone extensive refinement, primarily due to the need for improved predictions and the availability of high-speed large-capacity digital computers. The need for increased performance, lower noise levels, and other considerations have stimulated the development of improved analytical tools for use in helicopter design. The capabilities of modern computers together with the need for refined analyses has led to more realistically detailed analytical models for calculation of approximate nonuniform wake-induced inflow, blade natural frequencies and mode shapes, and blade loads. The improved approximations for the wake model have provided a fair quantitative measure of the nonuniform wake-induced inflow, and due to this, an improved prediction of the higher-harmonic airloads acting on the blades.

In recent times, the development of a model for nonuniform inflow determination was carried out independently, and at about the same time by Piziali and DuWaldt (ref. 1) and by Miller (ref. 2). The many applications of this theory, such as those of references 3 and 4, have made quite clear the importance of wake structure and geometry in determining blade dynamics. In particular, the outboard portion of the wake of each blade, which rapidly rolls up into a concentrated vortex (usually termed a tip vortex) has a significant influence on higher-harmonic loading (refs. 3 and 5), transient response (ref. 6), rotor noise (ref. 7), and overall performance (ref. 8).

Improved high-harmonic airloads alone are of limited usefulness in response and blade stress analysis unless compatible blade models are used in blade response calculations. In order that the response to higher-harmonic airloads be adequately computed by the use of normal modes of free vibration as generalized coordinates, modes with frequencies corresponding to the larger range of airload frequencies must be used. Current programs allow determination of these quantities for fully coupled modes for rotating blades, so compatible models for blade loads and blade response are available.

The determination of wake-induced flow at the rotor blades has been the most difficult part of the model to develop satisfactorily. This is primarily a result of the sensitivity of wake-induced flow to the magnitude of the relatively small distances between the tip vortex of one blade and the subsequent blade, especially on the advancing side. Similarly, because of the interactions of the various wake elements, the location of the inboard wake structure also has a significant effect on blade loading. Thus a reasonably accurate definition of the wake

geometry is needed in order that wake effects can be properly evaluated.

A rigorous determination of the structure and motion of the wake of a rotor is an extremely arduous task. The flow is unsteady, three-dimensional, and allows no convenient basis for linearization. As a result, the wake has been assumed to be a fixed skewed-helical pattern for forward flight conditions, and wake distortions have generally been neglected. Studies reported in refs. 9 and 10 indicated the possibility of predicting wake distortion effects.

In reference 9, the flow due to a rotor hovering near a ground plane was approximated by the axisymmetric flow due to a succession of vortex rings released from the rotor plane. A direct time integration of the flow was carried out, each vortex being free to convect at the local induced velocity. A fairly good approximation to the physical flow being modeled was obtained. There was clear evidence of wake contraction and the computed and measured flow exterior to the wake envelope agreed well. Near the rotor plane the interior flow was poorly predicted; it is believed that this resulted because the inboard wake structure was not represented.

In reference 10, the flow due to a rotor in forward flight was calculated. The wake of each blade was represented by a single concentrated tip vortex having a finite core of rotational fluid. The wake location for each rotor azimuth was determined by initially positioning the wake at locations approximating a skewed helix, allowing the wake to become free, and then performing continuous time integrations until a periodic flow was established. The calculation of the velocity at which each wake element was convected at a given instant included a term depending on curvature and core size of the vortex to account for local self-induced effects. Good agreement with flow measurements some distance from the rotor plane was obtained. Again, however, it is believed that omission of the inboard wake structure caused large errors in predicting the flow in or near the rotor plane.

Some attempts have been made to account for wake distortion in blade load analysis. In the calculation of VTOL propeller performance in reference 11, determination of wake distortion was made a part of the overall calculation. In this wake, consideration was limited to the hover case which made the flow steady relative to the blade. Reference 12 reports the results of the analysis of hovering performance of rotors as calculated using experimental results to position the wake. In a similar approach, the theoretical results of reference 9 were used in reference 8 to make an estimate of wake contraction for VTOL propellers in yawed flight. Thus, both theoretical and experimental wake distortion effects have been used in attempts to predict more realistic induced velocities. Although the procedures used in these studies are

limited to rather special cases, they do indicate the importance of accounting for wake distortions in the analysis of rotors and propellers.

Calculation of airloads and blade response through higher harmonics is often vital to the analysis of blade shears and moments, blade life and other design considerations. With the advent of new rotor configurations, such as rotors of different physical properties or nonuniform azimuthal blade positioning, a program capable of analysis of such systems became desirable. The present program has the capability of predicting wake geometry and wake flow, including the induced flow in the rotor plane for use in blade loads calculations, for a system of one or two helicopter rotors. If two rotors are used for the helicopter model, they may be arbitrarily located with respect to one another, have blades of different properties, rotate in the same or different directions, and the wakes from all blades are allowed to interact and to affect the induced velocity distribution on each of the rotor blades. The blade loads program uses input from both an independent blade frequency and mode shape prediction program and from the wake geometry program discussed herein to perform calculations of blade loads and blade response by an iterative procedure. Upon termination of these calculations, blade shears and moments are computed.

In addition to the calculation of distorted wake geometries, the effects of such geometries on wake-induced flow, and the resulting blade airloads, shears and moments, the program may also be used to compute other quantities of interest. For example, rotor angle of attack distributions are now computed but not written out, as are approximate blade loads during the wake geometry calculations. Similar predictions for models of helicopter rotor blade response in maneuvers, under gust loading, and similar applications may be possible with modifications to the existing program. By using a starting rotor approach with forward time integration as the basic method for calculation of wake geometry and wake-induced velocity effects, it is expected that this approach and program may be extended to the analysis of non-steady-state flight conditions.

SYMBOLS

a_i	core radius of i^{th} vortex element
$A_T, A_V, A_W,$ A_ϕ, A_ψ	mode shape quantities representing the torque, linear flap deflection, linear lead-lag deflection, angular torsional deflection, and angular lead-lag deflection, respectively. Torque dimensions in meter-newtons, linear deflection in meters, angular deflection in radians.

b	nondimensionalized semichord length
c	chord length, meters
c_d	section drag coefficient
c_l	section lift coefficient
$c_{l\alpha}$	slope of section lift coefficient, $\frac{dc_l}{d\alpha}$
c_m	section moment coefficient (about midchord)
C_T	thrust coefficient, (aircraft weight)/ $(\pi\rho\Omega^2R^4)$
d	perpendicular distance from point of induced velocity to axis of vortex element, meters (see fig. 3)
F_K	generalized force of the K^{th} mode
F_v, F_w	lumped aerodynamic forces acting at blade mass points, newtons
F_x, F_z	aerodynamic forces per unit span acting tangential and normal to the rotor plane, respectively, newtons/meter
I_b	mass moment of inertia of blade about flap hinge, meter-newtons/second ²
I_{x_i}	torsional mass moment of inertia about c.g. of i^{th} section of the lumped parameter blade model, meter-newtons/second ²
k	flap spring stiffness, meter-newtons/radian
l	lift per unit span, pounds/foot
m_b	blade mass, kilograms
m_i	mass of i^{th} section of lumped parameter blade model, kilograms
M	aerodynamic flapping moment on the blade about the blade hinge, meter-newtons
M_N	Mach number
M_0	aerodynamic twisting moment about midchord per unit span, newtons

M_ϕ	lumped aerodynamic twisting moment about elastic axis, meter-newtons
N_A	number of azimuthal steps per revolution
N_R	number of radial load points per blade
NGJ	number of radial load points on all blades
NW	number of azimuthal steps in the wake
\underline{q}	vortex induced velocity, meters/second
q_{s_i}	vortex self-induced velocity, meters/second
Q_v, Q_w, Q_ϕ, Q_ψ	forcing functions corresponding to linear flap, linear lead-lag, angular twist and angular lead-lag motions, used in computing generalized forces
r	radial coordinate, meters or dimensionless
r_0	radial distance to blade chord, meters
R	radial distance, meters
\underline{s}	position vector of vortex element
\underline{s}_p	position vector of point at which induced velocity is computed
\underline{s}_1	position vector, $\underline{s}_p - \underline{s}$
s_1	magnitude of \underline{s}_1 , $ \underline{s}_1 $
S	radius of curvature
t	time, seconds
T	torque, meter-newtons
U	velocity tangential to rotor plane, meters/second
v	linear flapwise blade deflection, meters
V	velocity normal to rotor plane, meters/second
V_f	aircraft forward velocity, meters/second
w	wake-induced velocity, meters/second or linear edgewise blade deflection, meters

\bar{w}	the chordwise average downwash, meters/second
w_1	the chordwise variable downwash, meters/second
w_0	uniform wake-induced inflow, meters/second
w_N	wake-induced inflow due to wake elements having known circulation, meters/second
x_b	spanwise distance to blade center from flap hinge, meters
α_β	tilt of tip path plane due to blade flap, positive forward, radians
α_0	sum of collective and cyclic pitch and blade twist angles
α_s	shaft tilt angle, positive aft, radians
β	blade flapping angle, $\beta = \beta_0 + \beta_1 \sin \Omega t + \beta_2 \cos \Omega t$, radians
$\beta_0, \beta_1, \beta_2$	steady and first harmonic lateral and longitudinal blade flapping components, radians
γ	circulation distribution, meters/second
γ_0	circulation distribution corresponding to uniform downwash, meters/second
γ_1	circulation distribution corresponding to variable downwash, meters/second
Γ	vortex element circulation, meters ² /second
Γ_0	circulation, chordwise integral of γ_0 , meters ² /second
Γ_1	circulation, chordwise integral of γ_1 , meters ² /second
δ	distance between flap hinge and shaft axis, meters
ϵ	chordwise separation of the elastic axis and center of mass, positive forward, meters
ζ_K	generalized coordinate for the K^{th} mode
θ_A, θ_B	angles used in vortex-induced velocity determination, see fig. 3, radians

θ_c	cyclic pitch control input angle, radians
θ_0	rigid body pitch, radians
θ_1	blade twist, radians
μ	advance ratio, $V_f/\Omega R$
ξ	local blade spanwise slope, radians
ρ	air mass density, kilograms/meter ³
σ	wake-induced velocity influence coefficient
ϕ	blade elastic torsional deflection, radians
ϕ	angle between chord and rotor plane, radians
ψ	azimuthal coordinate, positive counterclockwise, zero aft, radians
ψ	blade elastic edgewise bending angle, radians
ω_K	natural frequency of the K th mode, radians/second
Ω	rotor speed, radians/second

Subscripts and Mathematical Terminology

i, ℓ, n	indicate radial station of variable
j, k	indicate azimuthal station of variable
K	indicates vibration mode number
v	indicates force component acting in direction of v-displacement
w	indicates force component acting in direction of w-displacement
x	indicates force acting parallel x-axis
z	indicates force acting parallel z-axis
ϕ	indicates moment component acting in direction of ϕ -displacement

- ψ indicates moment component acting in direction of ψ -displacement
- Δ indicates an increment, i.e. Δt is an increment in time
- $\dot{}$ indicates time derivative, i.e. $\dot{v} = \frac{dv}{dt}$

ANALYSIS

The overall model and program arrangement is shown in Figure 1. The model and problem formulation may be conveniently thought of in two sets, one dealing with the wake model and associated calculations, the other dealing with determination of the aerodynamic blade loads and response. The combination of these analyses and corresponding computer programs are directed toward the prediction of blade loads and associated dynamic response for helicopters in steady forward flight in which the effects of a free wake and flexible blades are included. One or two rotors may be modeled, and if two rotors are used, the blades on one rotor may differ physically from the blades on the other rotor. Blade-wake interactions are allowed, but no mass or elastic couplings between blades on a rotor or between blades on different rotors are allowed. While the number of blades per rotor is arbitrary (subject to practical limits of the dimensioned variables in the computer program), each rotor is assumed to have the same number of blades, and to have the same rotor speed.

Wake Geometry Model and Formulation

The wake geometry is calculated by carrying out a process similar to the startup of a rotor in a free stream. The blades are located at specified azimuthal and flapping positions, without any wake vortices. The blades then rotate through an azimuthal increment, $\Delta\psi$, and shed and trail vortex elements of unknown strength, but with known positions. The strengths of the vortices that are shed immediately behind the blade are then determined, and include the effect of their own self-induced velocities. (If it is desired, an estimate of the blade loads that result can then be determined, without the effects of blade flexibility being included.) All vortex element end points not attached to the blade are then allowed to translate as the blade is stepped forward for a time Δt with velocities as determined by the free stream and induced velocities. Here, $\Delta t = \Delta\psi/\Omega$, where Ω is the rotational speed. This completes a typical first step in the wake geometry calculation.

Subsequent steps are similar. The blades are rotated through an angle $\Delta\psi$ and to new (specified) flapping angles. The vortices at and just behind the blades have unknown strength, while those in the wake have known strength. The strengths of the vortices attached to the blade are then computed, induced velocities at vortex element end points are computed, and end points not attached to the blade are allowed to translate with the resultant velocity due to the free stream and induced velocities. (Again, if desired, approximate blade loads may be computed, once blade circulations are known.) In this manner arrays of discrete shed and trailing vortices are generated immediately behind the blades with strengths which correspond to approximate blade loads. These arrays have stepwise radial and azimuthal strength variations so that total circulation is conserved. The arrays of shed and trailing vortices which are generated immediately behind the blades are referred to as the full mesh wake. Comparisons of wake flows predicted using this wake model for the entire wake with experimental measurements indicated that retention of shed elements with a coarse mesh resulted in poor induced velocity predictions, and that use of a fine mesh increased running time to an unacceptable level. Therefore, the full mesh wake was used to represent the wake immediately behind the blades, and a modified wake model was developed and implemented for use in the representation of the remainder of the wake, as shown in Figure 2.

The modified wake consists of trailing vortices only, so vorticity is not conserved. The locations, circulations, core sizes, etc. of the trailing vortices in the modified wake are determined in terms of the full mesh wake's last sets of trailing vortex locations, circulations, etc. The wake-induced velocities, wake distortions, and other calculations are essentially the same for both the full mesh wake and for the modified wake portions of the wake model.

The wake and blade vortices are assumed to have finite-sized cores of rotational fluid, and the core sizes at the blade are controlled by an input parameter so as to be adjustable to improve agreement between calculated and experimental or theoretical data as desired. All elements are assumed to be straight for purposes of calculations, except where induced velocity calculations are performed for an end point of a vortex element due to an element with one end at that point. At such a point the neighboring elements are assumed to be arcs with curvature determined by three appropriate end points.

The basic mathematical formulations of the wake geometry program are those related to determination of blade flapping motion, calculation of vortex-induced flow, and calculation of blade circulations including self-induced effects.

Determination of the approximate blade rigid-body flapping motions.- If blade flapping motions, collective and cyclic pitch angles, and flight conditions are known, these are input directly to the program. If flight conditions and collective and cyclic pitch angles are known but blade flapping motions are not known, a subroutine is used to compute approximate first harmonic flapping motions. If flight conditions but none of collective and cyclic pitch angles nor blade flapping motions are known, then collective and cyclic and blade flapping motions were approximated in preliminary calculations, using approximate uniform inflow and such that thrust and drag trim resulted.

If blade motions are not known, but collective and cyclic pitch angles and flight conditions are known, the blade motions used during the calculation of wake geometry are determined from the solution of the equation of motion for a rigid blade restrained from flapping by a spring. The spring stiffness is zero for a rotor with a flap hinge; for a rigid rotor the spring stiffness should be adjusted to give a rigid-body natural frequency approximately equal to the first flapwise bending natural frequency. Blade flapping motions are assumed to be forced by aerodynamic loads which are computed by assuming uniform wake-induced inflow and using specified values of the shaft angle and the collective and cyclic pitch angles. It should be noted that approximations to only the steady and first harmonic flapping motions are determined by the above process and used in the wake geometry calculations, and that quantities such as desired thrust (which is used in preliminary calculations) may not be the same as the computed thrust from this program. This is a result of blade motion effects due to blade flexibilities and nonuniform wake-induced velocities.

The equation of motion of a spring-restrained rigid blade, may be written as

$$I_b \frac{d^2\beta}{dt^2} + [k + \Omega^2 (I_b + m_b \delta x_b)] \beta = M \quad (1)$$

where I_b is the mass flapping moment of inertia about the hinge,
 t is time,
 m_b is the blade mass,
 δ is the distance from the shaft axis to the hinge,
 x_b is the distance from the hinge to the blade center of mass,
 k is the spring stiffness (zero for a springless hinge),
 M is the aerodynamic moment exerted about the hinge,
 β is the flapping angle, and
 Ω is the rotor rotational speed.

The moment M is given by

$$M = \int_{r_0}^R \ell (r - \delta) dr$$

where ℓ is the lift per unit span, and is given by

$$\ell = \pi c \rho (\Omega r + V_f \sin \Omega t) \{ \alpha_0 [\Omega r + V_f \sin \Omega t] - w_0 - r \dot{\beta} - V_f \beta \cos \Omega t + V_f \alpha_s + \Omega c \beta / 2 \}$$

Here r is the distance from the axis of rotation,

r_0 is the radius to blade root,

R is the rotor radius,

c is the blade chord,

ρ is the air density,

V_f is the forward flight speed,

α_0 is the sum of collective and cyclic pitch angles and blade twist angle,

α_s is the shaft tilt, positive aft, and

w_0 is the uniform wake-induced inflow, and is given by

$$w_0 = \Omega R \{ .5 [(C_T^2 + \mu^4)]^{.5} - \mu^2 \}^{.5}$$

where $C_T = (\text{aircraft weight}) / (\pi \rho \Omega^2 R^4)$

and $\mu = V_f / \Omega R$.

By letting β be assumed to have the form

$$\beta = \beta_0 + \beta_1 \sin \Omega t + \beta_2 \cos \Omega t ,$$

substituting into the equation of motion, and discarding all but steady and first harmonic terms, there result three equations for β_0 , β_1 , and β_2 which are solved to define the blade rigid-body steady and first harmonic flapping positions.

The natural frequency of free rigid-body flapping motion is given by

$$\omega = \{ [k + \Omega^2 (I_b + m_b \delta x_b)] / I_b \}^{1/2}$$

and for a rigid rotor, the desired spring stiffness, k , may be calculated from

$$k = I_b \omega_1^2 - \Omega^2 (I_b + m_b \delta x_b) \quad (2)$$

where ω_1 is the first flap bending frequency of the blade which is being modeled. (For a cantilevered rotor δ may reasonably be assumed to be the distance from the shaft axis to the first significant flapping flexibility of the blade.)

Determination of wake geometry.- The right-handed Cartesian coordinate system used in the formulation for the wake geometry calculations has the x-axis in the downstream direction (positive toward the rear of the helicopter, $\psi=0$) and the z-axis parallel to the rotor shaft of one rotor and positive up, as indicated in Figure 3. The center of one rotor is located at the origin of the coordinate system. A second rotor, if one is used in the model, may be located arbitrarily within this system. The flapping motions for each rotor's blade are determined independently as discussed previously. Given the flight conditions and appropriate rotor and control parameters, wake geometry calculations are essentially those required to compute vortex element strengths, vortex induced flow, and motion of the vortex elements.

The Biot-Savart law (see ref. 13, for example) is the basic relationship used for calculating vortex induced flows, and gives the fluid velocity \underline{q} at a point located by the vector \underline{s}_p due to a vortex with circulation Γ as

$$\underline{q}(\underline{s}_p) = - \frac{1}{4\pi} \int \frac{\Gamma(\underline{s}) \underline{s}_1 \times d\underline{s}}{s_1^3} \quad (3)$$

where $\underline{s}_1 = \underline{s}_p - \underline{s}$.

In order to compute total vortex induced flow at a point, the integral is taken over all vortex elements in the flow. For a straight element with end points located at A and B the induced velocity, q_w , at C is given by

$$q_w = \frac{\Gamma}{4\pi d} (\cos \theta_A - \cos \theta_B) \quad (4)$$

where Γ is the strength of the element and θ_A , θ_B , and d are as shown in Figure 4. When computing the vortex induced flow at a point due to an adjoining vortex element, equation(4) becomes indeterminate. Crimi, in ref. 10, gives the vortex induced flow due to adjoining finite core radii vortex elements whose end

points are used to define an appropriate radius of curvature, S , (called script \mathcal{R} in ref. 10) of a circular arc by the expression

$$q_{s_i} = \frac{1}{8\pi S} \left\{ \Gamma_{i-1} \left[\ln \left(\frac{8S}{a_{i-1}} \tan \frac{\phi_{i-1}}{4} \right) + \frac{1}{4} \right] + \Gamma_i \left[\ln \left(\frac{8S}{a_i} \tan \frac{\phi_i}{4} \right) + \frac{1}{4} \right] \right\} \quad (5)$$

where Γ , a , and ϕ are the vortex strengths, radii, and angle as indicated in Figure 5. Where it is necessary to compute the induced velocity at the edge of a wake where there are not vortex elements on either side of the point being considered, such as that at the juncture of the shed and trailing vortex elements at the tip (or root) as indicated at point A of Figure 2, the arc radius is computed from the two nearest elements' end points, and the induced velocity includes only the effect of the nearest vortex element. For example, if P_{i-1} in Figure 5 represented the edge of a wake with no element corresponding to P_{i-2} to the left, then S would be the same as in equation (5) but the term involving Γ_i would not be included. The induced velocity of an element end point just shed from the rotor blade includes a component due to the blade (bound) circulations, so that blade downwash effects are more nearly approximated in the region close to the blades.

The interaction of vortex elements is governed by the above equations except where a vortex end point falls inside the finite core of another element. In such cases the theoretically predicted induced velocity may be unrealistically high, and not representative of the true physical situation. In order that this unrealistic situation does not occur, the maximum induced velocity that is allowed is arbitrarily restricted to be less than a specified percentage of the rotor tip speed.

The blade circulations are calculated as follows. The velocities V and U , normal and tangential to the plane normal to the shaft axis, are given approximately by

$$V = V_f (\alpha_s - \alpha_\beta) + w \quad (6)$$

$$U = \Omega r + V_f \sin \psi \quad (7)$$

where α_s is the shaft axis angle with respect to the free stream, positive aft,
 α_β is the forward tilt of the rotor plane with respect to the shaft axis due to flapping, and

w is the induced upwash due to the wake (w=0 at start-up, i.e., there is no uniform downwash at start-up).

The momentum due to the average wake-induced upwash was calculated for some cases, and was within $\pm 15\%$ of the uniform downwash momentum value, depending somewhat on the radial distribution assumed from the outboard load point to the blade tip.

Using small-angle approximations, the lift per unit span is given by

$$l = \frac{1}{2} \rho U^2 c c_{\ell\alpha} [\alpha_0 + V/U] \quad (8)$$

where $c_{\ell\alpha}$ is the lift-curve slope, a constant, α_0 is the sum of collective and cyclic pitch and blade twist angle, and c is blade chord. The "Kutta-Joukowski law" states that (assuming $V/U \ll 1$)

$$l = \rho U \Gamma_b \quad (9)$$

where Γ_b is the blade circulation. Therefore

$$\Gamma_b = .5 c c_{\ell\alpha} [\alpha_0 (\Omega r + V_f \sin \psi) + V_f (\alpha_s - \alpha_\beta) + w] \quad (10)$$

For a set of rotor blades which have stepwise radial and azimuthal circulation variations, the above equations may be thought of as applying to each radial and azimuthal location independently. The wake-induced velocity on the blade, w, is made up of velocities due to known circulations in the wake and to unknown circulations at the blade, and may be written in the form

$$w(r_i, \psi_k) = w_N(r_i, \psi_k) + \sum_{\ell} \sum_j \sigma_{\ell j}(r_i, \psi_k) \Gamma(r_\ell, \psi_j) \quad (11)$$

where $w_N(r_i, \psi_k)$ is the induced velocity due to all known wake circulations,

$\Gamma(r_\ell, \psi_j)$ is the blade circulation at r_ℓ, ψ_j , and

$\sigma_{\ell j}(r_i, \psi_k)$ is an influence coefficient which, when multiplied by the circulation $\Gamma(r_\ell, \psi_j)$ gives the induced velocity of that element at r_i, ψ_k .

The summations over the indices ℓ and j indicate a summation over all radial sections of all blades at their respective azimuthal positions. Then a set of equations for all Γ 's may be obtained, and is of the form

$$\Gamma_{ik} = \frac{c}{2} c_{\ell\alpha} \left[\sum_{\ell} \sum_j \sigma_{\ell j i k} \Gamma_{\ell j} + \alpha_0 (\Omega r_i + V_f \sin \psi_k) + V_f (\alpha_s - \alpha_\beta) + w_N \right] \quad (12)$$

Here Γ_{ik} is equivalent to $\Gamma(r_i, \psi_k)$, and occurs on both sides of the equation. This equation is solved with a simple iterative procedure. The procedure is as follows. The terms on the right-hand side of equation (12) which do not involve the Γ 's are used as an initial estimate for the $\Gamma_{\ell j}$'s. Then the Γ_{ik} 's are evaluated from the equation, and as each is evaluated, it replaces the appropriate $\Gamma_{\ell j}$ (on the right-hand side). Once a complete set of Γ_{ik} 's is determined, it is compared to the previous set, and convergence is assumed when the sum of the squares of the differences of the sets of Γ 's divided by the sum of the squares of the Γ 's is less than an input control constant, approximately 0.00005.

After the blade circulation values are determined for a given azimuthal location of the blades, vortex-induced velocities are computed at all vortex element end points in the wake. The blades are then advanced through an azimuthal increment, $\Delta\psi$, and each vortex end point which is not attached to the blades is allowed to translate for the time period $\Delta\psi/\Omega$, with the resultant velocity due to the free stream and induced velocities. The entire computational process for the new rotor blade positions is then repeated. That is, new wake-induced and free stream velocities at the blades are computed and used to determine new blade circulations. Then new vortex end point velocities are computed, etc. Each blade advance results in an additional set of shed and trailed vortices being added to the wake. The number of revolutions of wake retained for actual computational purposes is restricted by an input to the computer program.

Wake flow and wake-induced velocity influence coefficient calculations.— Calculation of wake flow is done by using the same basic programming which computes flow at a point due to an arbitrarily located vortex element, except that the point is specified by input, and the flow is averaged and nondimensionalized for purposes of comparison with experimental data. Calculation of input for the blade loads part of the program is done by manipulating and properly subscripting numbers equivalent to the $\sigma_{\ell j}(r_i, \psi_k)$ and similar numbers used in the computation of w_K . These numbers are used in the solution of an equation in the blade

loads program which is approximately equivalent to equation (12). Both the wake flow calculations and the evaluation of the input to the blade loads program are computed only after a specified number of revolutions have been done. Thus, the input (including both σ and Γ type quantities as discussed above) from the wake geometry program to the blade loads program is based on approximate (specified) blade motions and an approximately repetitive wake. The repetitive nature of wake-induced effects was determined by visual checking of data to occur after approximately $\Omega R/V\pi$ rotor revolutions.

Blade Loads and Response Model and Formulation

The right-handed coordinate system used in the calculation of (periodic) blade circulations and blade response is located such that the z-axis is fixed to the shaft, directed upward, the x-axis is downstream, blade azimuth angle, ψ , is measured with respect to the x-axis, and the distance radially outward from the axis of rotation on a given blade is denoted by r, as shown in Figure 6.

Determination of aerodynamic loading.- The aerodynamic loading at a given radial and azimuthal station is derived from the flow experienced by the blade section, as sketched in Figure 7. The geometric incidence of the section with respect to the rotor plane is the sum of the rigid body pitch angle $\theta_0(\psi)$, blade twist $\theta_1(r)$, and the torsional deflection $\phi_1(r, \psi)$. The velocity component tangential to the rotor plane, U, is given by

$$U = \Omega r + V_f \cos \alpha_s \sin \psi \quad (13)$$

and that normal to the rotor plane, V, is given by

$$V = -V_f \sin \alpha_s + \dot{h}(r, \psi) - w \quad (14)$$

where \dot{h} is the plunging velocity due to the response of the blade including blade flexibilities, and w is the wake-induced downwash.

As is indicated in Figure 7, the foil section is replaced by a vortex distribution of strength $\gamma(r, \xi, \psi)$ along the chord. This distribution is adjusted to make the flow at the section tangent to the chord, which relates γ to the w and yields the basic relationships governing the aerodynamic loading. The function γ may be written as the sum of two contributions: γ_0 , which is the circulation required for flow tangency with the section subject to a chord-wise uniform downwash, and γ_1 , which is the circulation required for

flow tangency for the section subject to a downwash which is varying chordwise in such a way as to give no average downwash. Thus, the chordwise average of the downwash, \bar{w} , is defined as

$$\bar{w}(r, \psi) \equiv \frac{1}{2b} \int_{-b}^b w(r, \xi, \psi) d\xi .$$

The portion of the downwash which is variable over the chord, w_1 , is given by

$$w_1(r, \xi, \psi) \equiv [w(r, \xi, \psi) - \bar{w}(r, \psi)] - \xi \frac{d}{dt}(\theta_0 + \phi) .$$

Now the flow over an airfoil subject to a chordwise uniform downwash is exactly equivalent to the flow due to angle of attack. The distribution γ_0 , or rather its integral, Γ_0 , which gives the lift, is that quantity which is measured in a wind tunnel, under static conditions. That is, the total circulation, Γ_0 , may be defined in terms of γ_0 as

$$\Gamma_0 = \int_{-b}^b \gamma_0 d\xi ,$$

or in terms of the lift per unit span, ℓ , for incidence α and Mach number, M_N , as

$$\Gamma_0 = \ell(\alpha, M_N) / \rho U$$

where U is the resultant free-stream speed. In terms of the section lift coefficient, c_ℓ ,

$$\Gamma_0 = U b c_\ell(\alpha, M_N) \tag{15}$$

where $c_\ell(\alpha, M_N)$ is an experimentally determined lift coefficient.

The circulation resulting from chordwise variations in downwash is not readily measured, but thin airfoil theory allows evaluation of Γ_1 , the circulation which results from the downwash w_1 , as

$$\Gamma_1 = -2 \int_{-b}^b w_1(r, \xi, \psi) [(b + \xi)/(b - \xi)]^{1/2} d\xi \tag{16}$$

where

$$\Gamma_1 = \int_{-b}^b \gamma_1 d\xi .$$

Then the blade circulation is given by

$$\begin{aligned} \Gamma(r_i, \psi_j) = & b_i (U_{ij}^2 + V_{ij}^2)^{1/2} c_\ell(\alpha_{ij}, M_{ij}) \\ & - 2 \int_{-b_i}^{b_i} w_1(r_i, \xi, \psi_j) [(b_i + \xi)/(b_i - \xi)]^{1/2} d\xi \end{aligned} \quad (17)$$

where i and j range over all radial and azimuthal stations, respectively, and where

$$U_{ij} = \Omega r_i + V_f \cos \alpha_s \sin \psi_j ,$$

$$V_{ij} = \dot{h}(r_i, \psi_j) - V_f \sin \alpha_s - \bar{w}(r_i, \psi_j) , \text{ and}$$

$$\alpha_{ij} = \theta_0(\psi_j) + \phi(r_i, \psi_j) + \theta_1(r_i) + \tan^{-1}(V_{ij}/U_{ij}) .$$

The average wake-induced downwash effects are given by

$$\bar{w}(r_i, \psi_j) = \sum_m \sum_n \sigma_{mn}(r_i, \psi_j) \Gamma(r_m, \psi_n) \quad (18)$$

where the function $\sigma_{mn}(r_i, \psi_j)$, when multiplied by $\Gamma(r_m, \psi_n)$, represents the cumulative contribution to \bar{w} of elements in the wake having strength $\Gamma(r_m, \psi_n)$. The integral over the chordwise-variable downwash is found to be

$$\begin{aligned} & \int_{-b_i}^{b_i} w_1(r_i, \xi, \psi_j) [(b_i + \xi)/(b_i - \xi)]^{1/2} d\xi \\ & = - \frac{\pi b_i}{4} [\theta_0(\psi_{j+1}) + \phi(r_i, \psi_{j+1}) - \theta_0(\psi_{j-1}) - \phi(r_i, \psi_{j-1})] \end{aligned} \quad (19)$$

Equations (17) are a set of $N_R \times N_A$ nonlinear equations in the $N_R \times N_A$ strengths $\Gamma(r_i, \psi_j)$. ($N_R \times N_A$ is the total number of calculation points in the system.) Determination of the circulation is done by an iterative technique as follows. Blade circulations from the wake geometry program are used to compute the wake-induced downwash \bar{w}_{ij} , and are also used to compute aerodynamic forces, from which blade response in terms of normal modes is determined. (The response part of the program is discussed later.) This allows determination of h , ϕ , and other quantities which are a result of blade response. The velocities U_{ij} and V_{ij} , and angle of attack, α_{ij} , are then computed, and for each combination of i and j , $c_l(\alpha_{ij}, M_{ij})$ is determined from an analytical approximation to measured lift coefficient values. Determination of these quantities allows a new set of circulations to be computed from equations (17). The process is repeated, i.e., the new values of $\Gamma(r_i, \psi_j)$ are used to obtain new estimates for Γ_1 , \bar{w} , and α , which in turn allows calculation of another set of $\Gamma(r_i, \psi_j)$'s. The iteration continues until the values of the circulations for two successive iterations agree to within a prescribed amount.

Once blade circulations have been obtained, the lift and moment per unit span are readily calculated. Resolving the forces into components normal and tangential to the rotor plane, F_z and F_x , respectively, results in the following expressions for F_z and F_x (with F_x positive in the normal drag direction):

$$F_z = \rho U \Gamma + \rho \frac{d}{dt} \left\{ b \Gamma + 2c_m b^2 \sqrt{U^2 + V^2} - 2 \int_{-b}^b (w - \bar{w}) \sqrt{b^2 - \xi^2} d\xi \right\} \quad (20)$$

$$+ c_d b V \sqrt{U^2 + V^2} \quad , \text{ and}$$

$$F_x = -\rho V \Gamma + \rho c_d b U \sqrt{U^2 + V^2} \quad , \quad (21)$$

where c_m and c_d are the section moment coefficient (about midchord) and the section drag coefficient, respectively. The moment about midchord, M_0 , is given by

$$M_0 = -\rho U \int_{-b}^b \gamma(\xi, t) \xi d\xi - \frac{\rho}{2} \frac{d}{dt} \int_{-b}^b (b^2 - \xi^2) \gamma(\xi, t) d\xi. \quad (22)$$

The above quantities are functions of radial and azimuthal position, and are understood to have appropriate subscripts. The aerodynamic coefficients are computed from an empirical analytical representation of experimental data for a NACA 0012 airfoil, and are non-linear functions of Mach number and angle of attack. Representation of other airfoils may be implemented by developing subroutines which, given angle of attack and local velocity and Mach number, provide the necessary aerodynamic coefficients (lift, drag, and moment).

Determination of blade response.- The aerodynamic forces and moments, as computed, are not in a convenient form for calculation of blade response. A coordinate transformation and integration of the aerodynamic loads are performed so that generalized forces acting on previously determined flexible blade normal mode shapes may be computed. The moment is transferred to quarter-chord from mid-chord and the nondimensional distributed airloads are made dimensional. The distribution of aerodynamic forces and moments is approximated by straight lines passing through zero at the blade root and tip, and through the computed values at the aerodynamic loads points between the root and tip. Lumped loads to be applied at the lumped parameter blade model mass points are then computed by integrating the distributed loads over appropriate radial lengths. For example, the drag force applied to the i^{th} mass is given by

$$f_x = \int_{R_1}^{R_2} F'_x(r) dr$$

where R_i and R_{i+1} are midway between masses m_{i-1} and m_i , and between m_i and m_{i+1} , respectively, and where $F'_x(r)$ is the straight line approximation to F_x . Loads in the local blade coordinate system result from the coordinate transformations

$$F_v = -f_z \cos \phi - f_x \sin \phi$$

$$F_w = f_z \sin \phi + f_x \cos \phi$$

$$M_\phi = m_0 + z_A F_v$$

where z_A = distance of elastic axis forward of quarter chord. The total forces and moments at the radial positions corresponding to each blade mass point and azimuth are computed. (These loads are applied at the blade elastic axis.) For example, the force at

the i th mass station and j th azimuth, in the direction of blade flapping motions, denoted by $Q_{v_{ij}}$, is given by

$$\begin{aligned}
 Q_{v_{ij}} = & m_i \{ \Omega^2 \sin \phi_{ij} (h_i + \epsilon_i \cos \phi_{ij}) \\
 & + \ddot{\theta}_c [\epsilon_i + h_i \cos (\phi_{ij} - \theta_{0j}) / \cos \phi_{ij}] \\
 & - 2 \Omega \epsilon_i \dot{\psi}_{ij} \sin \phi_{ij} \} + F_{v_{ij}} . \quad (23)
 \end{aligned}$$

Here the first term is the steady acceleration force on the i th mass due to rotation, the second term accounts for control angle acceleration, the third term is a gyroscopic coupling term, and the fourth term is the aerodynamic load on the i th mass. Equivalent expressions are used for Q_ψ , Q_w , and Q_ϕ , which correspond to the elastic deflections ψ , w , and ϕ , the in-plane angular, in-plane linear, and torsional angular elastic deflections, respectively. The Q_ψ is given by

$$\begin{aligned}
 Q_{\psi_{ij}} = & m_i \Omega^2 \epsilon_i r_i \\
 & - 2 \Omega [I_{0i} \sin \phi_{ij} + m_i \epsilon_i h_i \sin \theta_{0j} / \cos \phi_{ij}] \dot{\theta}_{cj} \\
 & - 2 \Omega [I_{0i} \dot{\phi}_{ij} - m_i \epsilon_i (\dot{v}_{ij} \sin \phi_{ij} + \dot{w}_{ij} \cos \phi_{ij})] , \quad (24)
 \end{aligned}$$

Q_w is given by

$$\begin{aligned}
 Q_{w_{ij}} = & m_i \Omega^2 \cos \phi_{ij} (h_i + \epsilon_i \cos \phi_{ij}) \\
 & - [m_i h_i \sin (\phi_{ij} - \theta_{0j}) / \cos \phi_{ij}] \ddot{\theta}_c \\
 & - 2 m_i \Omega \epsilon_i \cos \phi_{ij} \dot{\psi}_{ij} + F_{w_{ij}} , \quad \text{and} \quad (25)
 \end{aligned}$$

$Q_{\phi_{ij}}$ is given by

$$\begin{aligned}
 Q_{\phi_{ij}} = & - \Omega^2 \sin \phi_{ij} (I_{0_i} \cos \phi_{ij} + m_i \epsilon_i h_i) \\
 & - [I_{0_i} + m_i \epsilon_i h_i \cos (\phi_{ij} - \theta_{0_j}) / \cos \phi_{ij}] \ddot{\theta}_c \\
 & + 2 \Omega I_{0_i} \sin \phi_{ij} \dot{\psi}_{ij} + M_{\phi_i}
 \end{aligned} \tag{26}$$

In equations (23) through (26)

m_i = mass at ith radial station,

$I_{0_i} = I_{x_i} + m_i \epsilon_i^2$

I_{x_i} = torsional inertia about c.g. at ith radial station,

ϵ_i = chordwise separation of the elastic axis and center of mass,

r_i = radial distance to the ith mass,

ϕ_{ij} = angle between the chord and the rotor plane,

h_i = horizontal separation of the elastic axis and the pitch axis,

θ_{0_j} = blade angle at blade root,

θ_c = pitch input control angle, and

\dot{w} , \dot{v} , $\dot{\psi}$, and $\dot{\phi}$ are values from the previous iteration.

The generalized force associated with each mode, F_K , is then computed according to

$$F_K(t) = \sum_i \left[Q_{v_i} A_{v_{iK}} + Q_{w_i} A_{w_{iK}} + Q_{\phi_i} A_{\phi_{iK}} + Q_{\psi_i} A_{\psi_{iK}} \right] + \sum_j \sigma_{KJ} \dot{\zeta}_{K1} \tag{27}$$

where the $A_{v_{iK}}$ are mode shape deflections in the v direction, at

the i th mass station, for the K th mode, etc., and the σ_{KJ} , ω_K , and $\dot{\zeta}_{K1}$ are the artificial damping coefficient, natural frequency and generalized coordinate rate for the previous iteration, respectively, for the K th mode. (The mode shape quantities, $A_{V_{iK}}$, etc., and corresponding natural frequency ω_K are provided by an auxiliary program. The corresponding model and formulation is briefly described later.) The generalized coordinate in the K th mode, ζ_K , and its time derivatives are then computed, based on the equation of motion

$$\ddot{\zeta}_K + 2 \sigma_K \omega_K \dot{\zeta}_K + \omega_K^2 \zeta_K = F_K(t) \quad (28)$$

and the requirement that ζ_K be periodic. Response variables of interest, such as the flapping velocity due to elastic motions, $\dot{v}_i(t)$, are then computed from expressions of the form

$$\dot{v}_i(t) = \sum_K A_{V_{iK}} \dot{\zeta}_K(t) \quad (29)$$

Blade dynamic response quantities are then used to define, by appropriate transformations and interpolations, quantities to be used in blade load calculations such as $\dot{h}(r_i, \psi_j)$, as given by

$$\begin{aligned} \dot{h} = & \frac{1}{\Omega R} \{ \dot{v} \cos \phi - \dot{w} \sin \phi + z_A \dot{\phi} \cos \phi \\ & + [z_A - h] [\dot{\theta}_c - \Omega(\xi \cos \phi + \psi \sin \phi)] \} \\ & + \mu \cos \alpha_T \cos \Omega t (\xi \cos \phi + \psi \sin \phi) \end{aligned} \quad (30)$$

The process is then repeated, with new blade circulations being computed with the inclusion of the effects of the new blade motions. The iteration process is terminated when (1) a specified maximum number of iterations between blade circulations and blade motions have been performed, (2) the values of blade circulations for successive iterations agree to within a certain constant, (3) the iteration procedure begins to diverge, or (4) the time or output line or page limit as controlled by the computer program job card are exceeded. Upon convergence, divergence, or reaching the limit

on the number of iterations of the iteration procedure between blade circulations and blade response, shear and moment quantities are computed from mode shape quantities. For example, the torque, T , is given by

$$T(r_i, \psi_j) = \sum_K A_{T_{iK}} z_K(\psi_j) \quad (31)$$

Both aerodynamic forces and shear and moment quantities are harmonically analyzed, and are printed in terms of harmonic coefficients as well as functions of radial and azimuthal position.

Determination of initial estimates.- Due to the iterative solution for a compatible set of blade loads and blade response, good estimates of load and response quantities are helpful to prevent divergence, and if properly chosen enhance convergence.

Estimates of blade flapping motion for use in blade loads calculations may be computed by a method equivalent to that used in determining blade flapping motions for the wake geometry and wake-induced velocity influence coefficient calculation. When the shaft axis is chosen to be perpendicular to the tip path plane, blade flapping motions are assumed to be zero. Estimates for blade (bound) circulations for the blade loads program are input from the wake program, and are those values associated with the last steps of the wake program calculations.

Blade natural frequency and mode shape determination model and formulation.- The program which calculates blade natural frequencies and mode shapes is an independent program which was developed by RASA and could be replaced by any approximately equivalent program. The necessary output for any such program in order that it might be used as input for the blade loads program are the natural frequencies together with the corresponding mode shape quantities, i.e., flapping and edgewise displacements, angles, shear forces, and moments, and torsional deflection and torque. These mode shape quantities are to be defined at the location of the point masses of the lumped parameter model, with mode shape magnitudes adjusted to give unity generalized mass. The lumped parameter model lengths, mass and inertias, mass eccentricities, offsets of elastic axis from pitch axis and midchord, twist distribution (but not model bending or torsional stiffnesses) are used in the blade loads-response program.

The blade frequency program developed by RASA is described in references 14 and 15, and the model used, development of input data, and operation of the blade frequency program are discussed in more detail in those reports. Briefly, the model used for the real blade is a lumped parameter approximation consisting of

uniform massless elastic beam sections under tension due to centrifugal loads, with point masses and inertias located at the ends of the massless lengths. A modified transfer matrix approach is used in determining the natural frequencies and mode shapes. (See, for example, ref. 16). The natural frequencies and corresponding mode shape quantities are used in the calculation of the response of the flexible blades to aerodynamic and inertia loads in the blade loads and response part of the program.

Computer Program Description and Use

The computer programs used for the implementation of the model constitute more than one separate program, and may be classified as those used for preliminary calculations, that used for wake geometry and wake flow or wake influence coefficient calculations, and that used for computation of blade loads and blade response. The preliminary calculations, some of which were done by computer programs, included determination of blade control inputs and determination of blade dynamic properties as described by a limited number of fully coupled free vibration mode shapes and corresponding natural frequencies. The flow diagram shown in Figure 1 indicates the general procedure used in the calculation of results. After available flight conditions, control settings, blade properties, etc. are obtained, this data is used to develop input to the wake program and the blade loads and response program. Equations which were programmed for calculation are given in the Appendix.

The necessary data for input, including program control variables, is given in the Program Documentation, which is available as RASA Report 69-9. Experimentally measured or theoretically or empirically calculated data may be used for such data as blade cyclic and collective pitch settings, blade flapping motions, blade natural frequencies, etc. The blade control settings and approximate flapping motions for cases where such data is available may be taken from such data. Where experimental data isn't available, performance-type programs, charts, or tables may be used to provide this data, as appropriate. Blade mode shapes and frequencies may be computed by any method desired, but must give mode shapes with a generalized mass of unity for use in the blade response calculations. The blade vibration characteristics used in the calculations discussed herein were obtained with an independent program which computes fully coupled (flapwise, edgewise, torsion) free vibration mode shapes and natural frequencies. Airfoil characteristics used in the calculations were for a NACA 0012 airfoil, and are determined in a subroutine by algebraic approximations to experimental data. If desired, this subroutine could be replaced by similar subroutines or table look-up procedures for other airfoil sections, for models which include rate effects, etc. The calculation or tabulation of airfoil data in a form suitable for use in the wake and loads programs may be thought of

as a preliminary calculation, since at the present time it is operational for a NACA 0012 airfoil section, only, and any different models would have to be developed in a similar manner before being used.

After the necessary input quantities have been determined, the wake geometry program may be run to obtain wake geometry data and wake flow data or wake influence coefficients for use in blade loads. Ordinarily, if wake flow data is desired, wake influence coefficients are not, and vice versa, but both may be obtained if desired.

The blade loads and response program does not require wake influence coefficients for operation; omission results in blade loads and response which do not include free wake effects; rather an assumed uniform wake-induced inflow is used. It is necessary to input at least one natural frequency and mode shape from the blade free vibration analysis, as well as flight conditions, helicopter blade control settings, and program control variables. The blade loads and response program may be conveniently thought of as two large subroutines, one which computes blade loads, and one which computes the response to those loads. Nonlinear effects are included in the model, so starting estimates for some quantities are made either by input or by the programs, and iterations between load and response calculations are required in order to compute a compatible set of blade loads and response variables. The maximum number of iterations allowed is limited by input. Convergence within that number of iterations is determined by the relative change in bound circulation from one iteration to the next, as compared to an input number. Output of load and response data is provided when any of the following situations occurs: (1) the convergence criteria between loads and response is satisfied, (2) divergence of loads from one iteration to the next occurs, or (3) the maximum number of iterations is reached. This output data in the first situation is the desired final output, while in the other cases the output serves as a source of information which may be used to determine reasons for failure to converge.

Listings of the program used to compute the wake geometry and wake flow or wake induced velocity influence coefficients, and the program used to compute blade loads and response are given in Volume II. Listings of the programs used to perform preliminary calculations, including the blade free vibration program are not presented, inasmuch as they were not part of the contract effort and are proprietary programs. It should be noted that the program input and output requires the use of English unit quantities, rather than metric unit quantities.

RESULTS AND DISCUSSION

This section presents and discusses the results of preliminary calculations, the comparison of predicted and measured wake flows and the effects of various numerical parameters of the program on the representation achieved by the model. The predicted blade load and response quantities for a model rotor are then presented and discussed. The effect on blade loads of geometric and flight conditions including advance ratio, vertical blade separation, azimuthal blade separation, and blade radius ratios are discussed. All calculations of blade load and response quantities include the effects of a free wake. The free wake and corresponding approximate blade loads were computed with the same basic program which was used to compute wake flows. Blade loads and response for flexible blades as computed included the effect of a free wake for specified blade motions, and the effects of flexible blades as contained in the mode shapes and natural frequencies of a fully coupled (flapwise, torsion, edgewise degrees of freedom) lumped parameter model of a rotating beam. Various wake parameters chosen during and prior to the wake flow runs (which were made for comparison of predicted and measured flows), such as number and spacing of trailing vortices and azimuthal step size in the full mesh and modified wake, were used for subsequent wake geometry and blade loads calculations. The problems involved in the use of a full mesh model for the entire wake have been mentioned previously, and will be discussed in more detail hereafter. The blade free vibration calculations include the effects of rotor speed (flapwise and chordwise centrifugal stiffening), nonuniform mass, inertia, twist, and stiffness distributions, and spanwise variations of the center of gravity and the elastic axes with respect to the pitch axis. It does not include the effects of steady blade lag or coning (i.e., the free vibration equilibrium position has zero lag and coning angles), nor gyroscopic coupling terms (which would necessitate the use of complex numbers in the calculations, and would result in complex mode shapes). Gyroscopic coupling terms were accounted for in the calculation by including them in the generalized forcing function for each mode in the blade loads - response portion of the computer program.

Results of Preliminary Calculations

Preliminary calculations for the wake geometry and blade loads calculations included determination of a lumped parameter model of the various rotor blades and the corresponding fully coupled natural frequencies and normal modes. These calculations were performed by an independent program, and results were used as input in the blade loads-blade response program. The various blade models are sketched in Figure 8, blade properties are given in Table 1, and their

corresponding natural frequencies and mode shapes are given in Table 2 through 5. The changes in blade models are based on changes in tip radius or airfoil cutout. The first spanwise section torsional stiffness value includes the effects of a control stiffness adjusted so as to give a control torsion frequency ratio, ω/Ω , of 3.50, for the standard blade. The second edgewise bending mode is in the frequency range of the other modes only for the case of the blade which has an airfoil cutout to 0.4R. However, for completeness this mode was calculated and used in the early blade response computations for all blades. It was evident in the first calculations for case 9, that the relatively low chordwise and torsional bending stiffnesses of blade model 4 inboard of $r=0.4R$ (given in Table 1) resulted in excessive torsional and lead-lag deflections. The intent of the calculations with this configuration was to determine the aerodynamic effects of such a rotor configuration. Thus, it was decided that the blade stiffnesses, as contained in the blade normal mode shapes and frequencies, should be those of the blade with airfoil cutout to $r=0.1$, so that aerodynamic effects, and not elastic or dynamic effects would dominate. The "very flexible" blade properties as given for case 9 in Tables 1 and 5 are given for completeness, but were not used in the final blade loads runs of this configuration; rather, mode shapes and frequencies as determined for blade model 1 were used, together with airfoil chord size, cutout to $r=0.4$, etc., from blade model 4.

A performance-type calculation was made to determine collective and cyclic pitch and first flap bending amplitude for all of the flight conditions except case 1. Experimentally measured data was used to obtain input parameters for case 1. The model used in the performance calculation is essentially an isolated rotor for which values of collective and angle-of-attack of the plane of no feathering were adjusted to give approximate drag and thrust trim, with fuselage drag included. Cyclic pitch angles in the shaft oriented axis system were determined from the angle of attack of the plane of no feathering and an assumed shaft angle. The shaft was assumed to be perpendicular to the tip-path plane in subsequent calculations. Quantities used as input for the free wake and blade loads calculations are given for various flight conditions in Table 6. These include blade model identification (as given in Table 1 and Figure 8) advance ratio, blade chord, vertical separation (Δz), azimuthal separation ($\Delta\psi$), shaft angle, and collective and cyclic pitch control angles. Two rotors were used in all calculations, and these were numbered 1 and 2. Rotor number 1 has the standard blade tip radius in all cases, and Δz and $\Delta\psi$ are positive for cases where rotor number 2 is positioned above and ahead of rotor number 1, respectively. Other quantities are as defined in the previously discussed figures and equations. For case number 11, the collective and cyclic pitch angles are given for rotors number 1 and 2, in that order. All other cases were run with the

same collective and cyclic values for both rotors. (It may be noted that cases 1 and 2 could have been run as a 4-bladed single rotor instead of as 2-bladed double rotors.) All wake geometry and blade loads calculations were run for $NA=16$ in which the blade azimuth interval is 22.5° . It was found during the first blade loads run of case 7 that the rotor was badly out of trim. The performance calculations for case 7 were greatly affected by stall, which resulted in very high computed values of collective and lateral cyclic pitch. In contrast, the blade loads calculations indicated considerably less stall, revealing that lower values of collective and lateral cyclic pitch were necessary. These lower values were then used in the final run for case 7, and are those given in Table 6. Downwash momentum values were approximately the same as theoretical values, depending somewhat upon assumed distribution from the outboard load point to the blade tip.

Full Mesh Wake Model Results

Wake flow with full mesh model.- As mentioned previously, predicted and measured wake flow comparisons revealed such serious undesirable characteristics of the full mesh model that a change in the wake model was made. The nature of the discrepancy between the predicted and measured wake flows can be seen in the plot of the time-averaged wake induced flow shown in Figure 9. This shows unacceptably large variations in the predicted flow in the inner portion of the rotor disc along a port to starboard line at $x=0$ (i.e., at the rotor hub). No such variations were observed at $0.5R$ forward of the rotor hub, but similar variations were predicted along a line at $0.5R$ aft of the rotor hub. After detailed investigations of both the computer program and output, it was concluded that the large fluctuations in predicted average wake flow were due to shed vortex elements in the wake model. The shed vortex elements which contributed to the fluctuations were approximately aligned in the free stream direction and, because of azimuthal variations in bound circulation, had sufficient strength to cause the significant velocities. For example, shed elements contributing to large fluctuations at position $x=0.0R$ and $x=0.5R$ were noted, in general, to be those shed from the blade as it moved in the region $\psi=135^\circ - 225^\circ$ which in turn were carried back by the free-stream velocity to these positions. The alignment of the vortex elements in the free stream direction allows the element to induce velocities in the same direction for the entire time over which the average is taken. Two methods for alleviation of this unrealistic characteristic were considered. The full mesh wake model would be a satisfactory model provided that a sufficiently small azimuthal step size were used to yield shed vortices of low strengths and corresponding low induced velocities. The number of shed vortices needed to accomplish this was estimated to be greater than fifty, and the running time (or costs) of such a model would be prohibitive. Previous investigations have indicated that the shed vorticity immediately behind the blade is

important in computation of blade loads on that blade which sheds the vorticity, but is not as important in computation of loads on other blades. Dropping the shed vortices and reducing the number of trailing vortices was the second alternative which was investigated. The tip (trailing) vortex, of course, is known to be important for computation of all blade's loads wherever blade-vortex interactions occur. Previous investigations indicate that inboard wake representation can also be important.

Modified Wake Model and Results

The model, as shown in Figure 2, which was successfully used to overcome the problem of large fluctuations in average velocity, was one in which the full mesh wake was retained for a few azimuthal steps behind each blade, and then replaced by a modified wake, containing only trailing vortices. The number and location of trailing vortices in both the full mesh wake and in the modified wake are arbitrary, within dimension restrictions, and are determined by input. Other changes in the wake model include program modifications to account for vortex stretching effects, vortex element representations of vortex sheets, and vortex element induced velocity limits for wake flow and blade loads effects.

Vortex stretching.-The vortex stretching effect is that associated with a vortex which has been deposited in the wake with a length approximately $r\Delta\psi$, and which changes length due to free stream and wake-induced velocity effects. For high advance ratios, the inboard vortex elements on the advancing side tend to get stretched significantly as they are deposited in the wake, and such stretching results in stronger induced velocities from these elements than experiments indicate exist. The program now accounts for vortex stretching by multiplying induced velocities from individual elements by the ratio (ℓ_0/ℓ) where ℓ_0 is the length $r\Delta\psi$ (the approximate length of a vortex trailed from radial position r , for azimuthal step sizes of $\Delta\psi$) and ℓ is the current element length. This modification showed some beneficial effect at $\mu = 0.235$, and is expected to provide increasingly more realistic wake models with increasing advance ratio. The model now approximately preserves the total vorticity associated with each element, where before the vorticity per unit length was conserved.

Vortex core-smearing.-Use of vortex elements for the inboard wake gave correct trends in wake-induced flow, but resulted in peaks where such vortices were transported by a wake flow calculation point in an approximately fore-and-aft orientation. This effect is observed experimentally for the tip vortex, but not for the inboard wake. A comparison of the induced velocity field from a set of vortex sheets with that computed for a set of finite core elements having the same total strength indicated that a realistic finite core vortex element representation of a vortex sheet was

obtained by using vortex core radii with the dimensions of one-half the sheet span which they represent. The wake-induced velocity field for a set of four sheets of uniform strength and four finite core vortices with the same total vorticity is shown in Figure 10, and demonstrates the improved representation of a sheet by finite core vortices which may be expected with this model.

The induced velocities as shown in Figure 10 are for a distance from the plane of the sheet of one-fourtieth of the sheet width. For distances larger than this, there is improved agreement between small core element and sheet-induced velocities, and at a distance of one-fourth the sheet width, the two velocity plots are coincident. At distances less than one-fourtieth the sheet width the disagreement between smeared core and sheet-induced velocities becomes more pronounced near the edges of the sheet. The agreement between sheet and smeared-core velocities in the interior remains good for essentially all distances from the sheet. In general, it may be seen that the usual finite core vortex elements give two large peaks of opposite sign near the center of the span which it represents, while the smeared core and sheet both give peak velocities near the sheet edges. Differences between smeared core and sheet velocities in the interior region tend to be reduced by the cancellation of the large velocities due to neighboring sections having these velocities with opposing signs at the section interface.

Inboard modified wake vortex core radii are determined by input so that this or other models may be used as desired, provided that the radii do not have azimuthal variation. Wake flow runs showed some improvement with this modification, and it is expected that the improvement would be more significant for flight conditions such that the inboard wake passes close to the blade load points, wake flow points, or other wake element end points, where the induced velocity from the "smeared" core vortex element model will be a better representation of the inboard sheet than the previously used "small" core vortex element model. (The tip vortex core has a "small" core, and is determined as described in the Appendix.)

Induced velocity limit.-The use of a velocity limit for the induced velocity from an individual vortex element is a feature which was found to be necessary in order to allow computation of reasonable average velocities at wake flow points, and which is also expected to give reasonable blade loads. (It is suggested that this limiting should be done differently for future runs where blade-vortex interactions with the blade and vortex parallel or more nearly parallel than perpendicular are expected to occur.) Figures 11 and 12 show velocity time histories with and without velocity-limiting which, due to the finite azimuthal step size, result in different averaged velocities. The non-limited-velocity curve, as sketched, is more realistic, but the averaged velocity, \bar{v} is biased by the location of the vortex element with respect to the flow computation point near $\psi = 150^\circ$, i.e., \bar{v} is incorrect due to the time

spacing used to obtain $v(t)$ values to compute \bar{v} . The limited $v(t)$ curve, while not physically realistic, gives a more acceptable value of average velocity. The same general behavior is expected to be shown for blade loads. That is, values of wake-induced velocities are determined only a finite number of times, at equal time increments. Use of a small number of times (or azimuthal steps) is essential for economical program operation, but may result in an incorrect average velocity, an incorrect loading for blade loads, and incorrect wake distortion. The type of inaccuracies which occur with computation of \bar{v} are seen from Figure 11. The blade loads inaccuracy, with the use of normal modes as generalized coordinates, is one whereby the use of a small number of azimuthal steps may tend to cause lower frequency modes to be excited more than would be excited by the real vortex-blade interaction. Since this study did not include the use of high frequency modes, the same type of vortex-induced velocity limiting as was used to calculate \bar{v} is appropriate to keep lower modes from being incorrectly excited in the blade loads program. The wake flow and blade loads physical situations where this limiting is necessary are where a vortex passes by a wake flow or blade load calculation point such that the vortex is approximately perpendicular to the free stream or parallel to the blade, respectively, and where the wake flow or blade load calculation points are near the vortex core at one calculation time. This situation was present for wake flow calculations on the advancing side just below the rotor disc. Use of velocity limiting gave much more realistic \bar{v} versus space plots for those situations where vortices passed close by wake flow points, and did so for a reasonably small number of azimuthal points.

The magnitude of the velocity limit is arbitrary as far as program operation is concerned, and is input as a function of the radial position of the vortex element. In the wake flow runs the velocity limit used was five times the momentum value of uniform wake-induced velocity, v_0 . This velocity is a function of thrust coefficient, advance ratio, and rotor control angle, and is defined (see ref. 17) as

$$v_0/\Omega R = 1/2 C_T / (1 - 3/2\mu^2) (\mu^2 + \lambda^2)^{1/2}$$

It is felt that this is a reasonable limit, based on the wake flow calculation results. It is suggested that a multiple of v_0 be used for both wake flow and blade loads types of runs. (A limit of 10 v_0 was used in the blade loads runs.)

The computer program used to obtain the results reported here allowed considerable flexibility in choice of various model characteristics. It should be noted that the same model was used to obtain wake flow results for three different advance ratios, and that only parameters which depended on advance ratio were changed

for different advance ratios. The following assumptions were used in the wake flow and blade loads calculations, and were determined to be reasonable on the basis of both theoretical and experimental data.

Model parameter determination.- Wake flows and wake-induced effects for blade loads were assumed to be periodic by the time that wake elements deposited at the forward edge of the rotor disc reached the aft edge of the rotor disc. In terms of the number of revolutions of the rotors, N , this occurs for $N = 1/\mu\pi$. The velocity-limit of $5 v_0$ was observed to give satisfactory results for wake flow calculations. Input values were not varied with advance ratio, except for variables which depend on advance ratio, such as thrust coefficient, cyclic and collective pitch. etc. Inboard vortex element core sizes were "smeared" in the modified wake, vortex stretching effects were included, the same number and location of vortex elements in the full mesh and modified wake, and the same number of azimuthal steps were done for all the advance ratios. Various combinations of these parameters were used in preliminary wake flow runs, and the effects of these variations are discussed later. Velocity contributions from distant vortices were neglected in the wake geometry runs used to generate input for the blade loads runs. Preliminary calculations showed that such approximations were both reasonable physically and advantageous economically.

Various methods for determining the location and number of trailing vortices in the full mesh and modified wakes were used. The final method for determining full mesh trailing vortex location was one which assumes a loading and velocity distribution linear in radial coordinate, divides the blade into NR sections with equal total load, and locates the trailing vortices within each section so as to conserve impulse of vorticity. The modified wake trailing vortices were found to be best located by placing the tip vortex at the full mesh tip vortex, replacing the full mesh root vortex by two modified wake vortices located so as to conserve impulse, and placing one (or more) additional vortices so as to conserve impulse of the remaining sections of the full mesh wake. The number of full mesh and modified wake trailing vortices is arbitrary, as specified by input; but present dimensions allow 5 or fewer full mesh vortices and 4 or less modified wake vortices. These numbers of vortices were used for the wake flow runs, and appear to give satisfactory results. Fewer trailing vortices in the full mesh would make radial blade load variations difficult to predict, while fewer trailing vortices in the modified wake could result in unrealistic wake flow in the interior region immediately below the rotor disc.

Wake Flow Results

Wake-induced flow in the region immediately below the rotor disc was computed and compared with the experimentally measured average flow as reported in reference 17. The plots are for two vertical positions for each of the three survey lines shown in Figure 13, as indicated in the figures, and present the nondimensionalized average velocity as a function of y , y being the starboard to port coordinate, $+y$ being on the advancing side of the rotor, and all dimensions being nondimensionalized by rotor radius. Computations for advance ratios of 0.097, 0.141 and 0.235 were performed and the resulting plots of average wake-induced velocity are shown in Figures 14 through 22. Calculated velocities computed for a single tip vortex as reported in reference 10 are shown for the 0.141 advance ratio case. The overall agreement between computed and measured average wake-induced flow for the present model is good. Both the region near the disc edges and the inboard region have now been quite accurately modeled, with the inclusion of a more realistic inboard wake representation. The improvement achieved by including the inboard wake is particularly noticeable when compared with the tip-vortex-only model results at $x = 0.5$ and $z = -0.07$, as shown in Figure 19.

There is generally better agreement between computed and measured flow along the forward survey lines than along the mid-rotor and aft survey lines. The presence of the rotor shaft and of the other structures associated with the experimental tests was not modeled in the calculated flow. The presence of the rotor mast precluded measurements near $y = 0$ at the mid-rotor survey line, and could influence the apparent disagreement between calculated and measured flows in this region, which disagreement appears to be worst for $\mu = 0.235$. The largest discrepancies between computed and measured flows are noted along the aft survey line, particularly for $\mu = 0.097$ and $\mu = 0.235$. In both cases the flow magnitude is underpredicted near $y = -1.0$, and for $\mu = 0.097$ there is a predicted "bump" between $y = -0.5$ and $y = -0.7$ which has the same trend as the measured flow, but which is much higher. The wake is highly distorted for this case, and it is possible that some of the wake distortion effects are not adequately represented, leading to the prediction of this "bump". Use of more azimuthal steps with corresponding changes in averaged velocity values may more adequately represent the flow in this case. For the $\mu = 0.235$ case, the disagreement near $y = -1$ could be due to incorrect wake flow point location. The measured data was reported to be taken parallel the tip path plane, but lateral rigid body flap was measured. The predicted flows were computed by assuming no lateral flapping and placing the wake flow points parallel the resulting tip path plane. If, in fact, the measured data was taken in a plane not parallel the tip path plane, the small relative lateral flapping could have resulted in flow asymmetries that are observed in the measured data at $\mu = 0.235$, which are much more severe than for the other advance ratios.

Velocity limiting effects.- The effect of velocity-limiting for wake flow comparisons may be seen by comparing the predicted flow shown in Figure 19 (for $x = 0.5$, $z = -0.07$) with the predicted flow shown in Figure 23. On the advancing side, the rather severe variations in \bar{v}/v_0 with y have been traced to the tip vortex-induced velocity being close to some of the wake flow calculation points for only one azimuthal step. The resulting \bar{v}/v_0 quantities, as discussed in the previous section and shown in Figures 11 and 12, result in the variations shown in Figure 23, and were removed by limiting the induced velocity contribution at any computational point to have magnitude less than or equal to $5 v_0$ (v_0 is the momentum value of uniform inflow), in all cases. This limit, though somewhat arbitrary, was used for all flight conditions, and appears to be a realistic limit.

The wake-induced flows shown in Figure 23 do not contain other model characteristics which were used for the final wake flow calculations, such as vortex stretching and vortex smearing. The effects of the variation of various parameters on wake flow calculations were noted during preliminary wake flow runs. It was observed that the number of azimuthal steps influences the location of \bar{v}/v_0 variations due to vortex location when velocity limiting is not done, and that a significant increase in this number (from 12 to on the order of 100) is necessary to obtain realistic \bar{v} values without velocity limiting when the wake flow points are such that a tip vortex passes close by them at an oblique angle. Running time is increased significantly with an increased number of azimuthal steps. The number of radial trailing vortex elements required to compute reasonable radial aerodynamic load distributions is felt to be five or more, five being the upper limit of the present program due to core storage restrictions. The number of trailing vortices in the modified wake was varied from one to four, and the placement of these vortices was also varied. One trailing vortex gives the best results when placed near the tip, but does not consistently predict the flow in the interior of the disc immediately below the rotor, as can be seen from Figures 17, 18, and 19. Use of two trailing vortices generally resulted in poor prediction of the interior flow also, with either very little difference from the tip vortex only model, for small circulation values of the inboard element, or large spacial variations in \bar{v} for large circulation values. Three trailing vortices gave similar results. It should be noted, however, that runs with only two or three trailing vortices were made without vortex smearing, and vortex smearing could improve the results considerably for such cases. The best representation was obtained by using four trailing vortices in the modified wake model previously described. Other models, in which the full mesh root vortex was not divided into two modified wake vortices, gave large spacial variations in \bar{v} near the location where the root vortex is in an approximately fore and aft orientation. Again, no results were obtained with only vortex smearing but without division of the full mesh root vortex.

Calculated Wake Geometries

Free wake effects.- Wake geometries, as are important for analysis of wake effects on blade loads, are not necessarily well displayed by plots of averaged velocity. If it is accepted that the present model is physically realistic (based on the average wake-induced flow comparisons), then the distorted wake geometry should also be realistic. The existing measurements are not sufficient to allow "final" evaluation of the model's acceptability. Instantaneous velocity measurements would provide a much more complete data set for evaluation of wake geometry programs. Such measurements would be extremely difficult to obtain, of course, and do not exist at this time. Distorted wake geometries for the three advance ratios for which flow calculations were made are shown in Figures 24 through 26. In the x-z plots, (the side view, looking from port to starboard) the z-coordinate scale is expanded 5 times. The plots show only one tip vortex, which is drawn as a continuous curved element. The computer model used straight elements and has twelve azimuthal steps per revolution (for these cases). As is seen from these plots, there is considerable wake distortion, much more in the lower advance ratio than in the higher advance ratio cases. The importance of the wake distortion depends on what is being studied, flight conditions, rotor configurations, etc. For example, the plots of Figures 24 and 25 indicate that the rotor is operating such that it may pass through its own wake, for these particular flight conditions and this rotor configuration. There is not any blade-tip vortex intersection for this particular wake-rotor position combination, but it appears that such intersections do occur where the wake has been distorted up through the rotor disc. Wake distortion effects could be important, it appears, for many rotor combinations and flight conditions. Fixed skewed helical wake geometries would not allow prediction of such blade-vortex intersections as the present model appears to predict for single rotor helicopters, for example. It should be noted that the wake geometries shown in Figures 24 through 26 are for lightly loaded rotors, with values of C_T on the order of .0035 and for disc loadings of approximately 48 newton/meter². Considerably higher disc loadings and thrust coefficients are common on helicopters, and may result in higher downwash with correspondingly less chance for blade-wake intersections.

Instantaneous velocity measurement data is not known to be available, so no comparisons on that basis may be made at the present time. However, instantaneous velocities at two positions, as a function of time, were given in reference 10. Figure 27 shows a comparison of the measured average velocity, computed average velocities, and computed instantaneous velocities using the single vortex model of reference 10 and the multiple vortex model discussed herein. The calculated $v(t)$'s are more similar for $z = -0.07$ than for $z = -0.2$. The $v(t)$ calculated at $z = -0.07$ with a single tip vortex shows a slightly smaller range of values

than the $v(t)$ calculated with the system discussed herein; the phasing of the largest variation is practically identical, and the overall shapes are similar. The $v(t)$ calculated at $z = -0.2$ with a single tip vortex shows a much wider range of values than the $v(t)$ calculated with the more realistic wake model, which indicates that a vortex passed close by $z = -0.2$ in the tip-vortex-only model, but was not as close in the full mesh-modified wake model. The single-tip vortex model gives averaged velocities on the order of 20% higher than the measured average velocity, while the model presented here gives an averaged velocity less than 1% lower than the measured average velocity. As may be seen from Figure 19, there are a few points at which the single tip vortex predicted \bar{v} more closely than the present model, but values of $v(t)$ for other points were not presented in reference 10, so comparisons at other points cannot be made.

Vortex blade interactions.- The possibility of vortex-blade loading due to radial motion of the point of interaction was discussed in reference 18. Such problems led to suggestions for helicopter rotor systems with shaftwise separation of rotors, rotors having different lengths (and other physical differences), and nonuniform azimuthal blade spacing, in hopes that such systems may be useful in alleviating blade-vortex interaction problems. Wake geometry and wake-induced velocity influence coefficients were computed for several such rotor systems, and wake geometry plots for some of those systems are shown in Figures 28 through 33. Only two of the four tip vortices are shown, to reduce the complexity of the plots. The vortices are shown as continuous curves, but are based on sixteen steps per revolution. All coordinates are nondimensionalized by the reference rotor radius.

Table 6 shows the various model parameters used for the wake runs. Figure 28 shows the free wake for Case 2, which is a standard four-bladed helicopter configuration. The model used for this case was one with two two-bladed rotors with no shaftwise separation, 90° azimuthal spacing, advance ratio of 0.2, and with rotors rotating in the same direction. Figures 29 and 30 show the free-wake geometry for two rotor systems each with shaftwise separation of one chord for Cases 3 and 4, which are for physically identical blades, advance ratio of 0.2, and where Case 3 has an azimuthal separation of 90° and Case 4 a separation of 30° , respectively. Figure 31 shows the geometry for Case 7, which is for a system the same as shown in Figure 30, with an advance ratio of 0.3. Figures 32 and 33 show geometries for rotor systems with rotors of different lengths. Figure 32 presents the geometry for Case 10, which is for a system with an advance ratio of 0.2, a one chord shaftwise separation, a 30° azimuthal separation, and with the upper, forward rotor length being 0.85 of the reference rotor length. Figure 33 shows the geometry for Case 9, which is for a system with an advance ratio of 0.2, no chordwise separation, 90° azimuthal spacing, one rotor

with blades having no airfoil inboard of $0.4R$, and the other rotor having a length of 0.7 of the longer rotor. In all cases, the rotor system cyclic and collective values were intended to result in a lift of $17,800$ newtons and drag trim for a fuselage flat plate area of about 0.74 meters². These values of collective and cyclic were input, as were values of blade coning and first harmonic flapping. For Figures 28 through 33 the shaft axis is perpendicular to the tip-path plane.

There are both differences and similarities in the various wake geometries shown. The self-induced effects of the wake elements upon themselves due to their gross geometrical arrangements and circulation distributions appear to be the dominant source of free wake distortions. These gross distortion patterns are similar for all advance ratios and rotor configurations. Generally, near the rotor disc the horizontal distortions appear to be less severe than the vertical distortions. The edge of the wake, near $y = \pm 1$, tend to roll upward, and there are smaller upward distortions near $y = 0$ at both forward and aft areas of the wake. In the region either side of $y = 0$, vortices corresponding to the wake deposited near the leading edge of the rotor disc generally appear to pass from below to above the rotor blades as they move aft. The x -position where they move through the disc depends on advance ratio. One or more vortex-blade interactions could result from such distortions. The loops near $y = \pm 1$ generally extend from below to above the rotor disc and are inside the edges of the disc. These loops begin to form almost immediately after the tip vortex is deposited. After approximately one revolution the side loops have begun a gross roll-up pattern, especially on the advancing rotor side. Except at low advance ratios, the portion of the wake having this roll-up pattern has been transported aft of the rotor disc, so is not a region of potential vortex-blade interaction for the rotor systems and flight conditions investigated herein. The free wake distortions become increasingly pronounced with decreasing advance ratio. Figures 30 and 31 are wake geometries for identical rotor systems with advance ratios of 0.2 and 0.3 , respectively, and the computed distortions are much smaller for the 0.3 advance ratio than for the 0.2 advance ratio.

There are some characteristics which vary from case to case, and which may influence the type or severity of vortex-blade interactions. The wake from two rotors of equal lengths with 90° blade spacing, as shown in Figures 28 and 29, indicate that the distortion of the tip vortices near $y = 0$ is approximately the same from each blade. That is, the vortices are approximately at the blade tip elevation near $y = 0$ approximately one revolution after they were deposited in the wake near $x = -1$. In contrast to this, the wakes from rotors of equal length but with the upper rotor less than 90° ahead of the lower rotor show that this rotor configuration results in this region of the tip vortex from the upper rotor being transported lower than the tip vortex from the lower rotor in approximately the same time. Such distortions can be seen for

Cases 4 and 7 in Figures 30 and 31, respectively. The same types of distortions were also observed for Cases 5 and 6, where $\Delta\psi$ was 20° and 10° , respectively. This type of distortion is that which would be expected from the intertwining of two tip vortices, and is a direct result of the nonuniform azimuthal spacing. It is possible that such intertwining could result in different types or severity of vortex-blade interactions. (Such results were not observed from the subsequent blade loads runs, as will be discussed later.) Wake distortions for systems having rotors of different lengths generally showed more severe distortions than for systems having rotors of the same length. Figure 32 shows the wake geometry for Case 10, which is similar to Case 4 (shown in Figure 30) except that the upper rotor is 0.85 as long as the lower rotor, and the chords on both rotors were increased to retain the same amount of blade area for the total system. The intertwining process appears to be present, but it does not appear to have progressed as rapidly as for the cases with rotors of equal length. This is probably due to the tip vortices being positioned further apart (shortly after they are deposited), and thus resulting in less interaction. The wake geometry shown in Figure 33 is for Case 9. Tip vortex distortions are more severe for this case than for any other case with an advance ratio of 0.2. This appears due to the interaction of the short blade's tip vortex with that from the preceding long blade, near $y = 0$. Two of the tip vortices have been omitted from Figure 33. The location of the tip vortex from the long blade which is not shown is such that interactions with the following short blade's tip vortex are possible.

Calculations of wake-induced velocity influence coefficients for all cases were made with built-in limits on the magnitude of the off-diagonal elements of the influence coefficient matrix. The number of times in which the limit was used to reduce the size of the off-diagonal elements was small. The use of such a limit was found to be necessary in some cases during preliminary calculations in order to allow convergence of the blade loads iterative solution methods. Such limits were not felt to be overly restrictive, but could diminish the severity of vortex-blade interaction effects, and thus represent a limitation of the present model and calculated results.

Wake geometries shown in Figures 28 through 33 correspond to only one of sixteen reference blade azimuthal positions. Wake geometry plots could also be developed for any or all of the other blade azimuthal positions, and the tip vortices for other blades could also be shown. It is felt that presentation of such plots would add little to the basic understanding of the wake geometry model obtained from the plots already presented. Figure 34 presents the wake for all four blades for Case 4 (corresponding to Figure 30). The tip vortex intertwining process is observed for all four vortices. The vortex elements from the retreating blades which have been deposited for approximately one-half

revolution have approximately the same elevation at the front near $y = 0$, but with the originally "upper" vortex now slightly lower than the originally "lower" vortex. It appears that the intertwining process does not continue after the initial exchange of positions, and that the vortices near $y = 0$ which were deposited near $x = -1$ (forward part of rotor) may in some cases be sufficiently distorted to cause subsequent vortex-blade interactions near $x = +1$ at the rear of the rotor. Such interactions appear to be likely, as seen from Figure 34, between the upper blade and the lower blade's tip vortex, near $x = +0.7$ or $+0.8$.

In general, it does not appear that the various rotor systems provide a significant reduction in the number of vortex-blade interactions. However, the spacing (in time or azimuthal angle) and possibly the severity of the interactions are influenced by the various rotor systems. The present study indicates that some types of previously suggested vortex-blade interactions may not occur in the manner which would be expected for rigid wake models. For example, the type of traveling-force vortex-blade interaction suggested in reference 18 may occur, but the results of this study indicate that such traveling-force interactions may be limited to a smaller portion of the radius than rigid wake models would predict. This does not mean that the resulting blade response would necessarily be milder. If this type of interaction occurred over only a limited radial range, but occurred near the blade tip where the dynamic loads are high and at a rate such that blade response was high, a smaller radial range of interaction could be significant. It does appear that vortex-blade interactions may occur for more flight conditions and over more regions of the rotor disk than would be predicted by a rigid wake model.

Comparison of computed and measured average wake flows (reference 17) indicates that the present model is acceptable for average wake flow calculations, and implies that it is acceptable for wake geometry and wake-induced velocity influence coefficient calculations. The model uses a limited number of trailing vortices and azimuthal steps, which is important in obtaining numerical results at reasonable cost. The basic wake model is very flexible. It may be used for any two-rotor system which has equal rotor speeds on each rotor. It provides a basis for extensions to non-steady-state flight conditions and steady-state maneuver flight conditions. Running times are strongly dependent on the total number of elements generated. Wake flow runs for two and three revolutions of wake with four trailing vortices per blade in the modified wake and twelve azimuthal steps per revolution ran on an IBM 360/65 for about 9 and 18 minutes CPU time, respectively. Calculation of wake-induced velocity influence coefficients were made (after considerable program streamlining) on a CDC 6600, using overlay features to keep core storage requirements below 70,000 octal; all runs were made with four

trailing vortices in the modified wake and sixteen steps per revolution. Runs of one and one-half, two and one-half, and three and one-half revolutions required CPU times of approximately 2.5, 11, and 28 minutes, respectively. Thus, for moderate to high advance ratios, the present program and extensions of it would provide a flexible tool for use in further studies of one of the most complex problem areas associated with rotary wing aircraft operations - that of determining the free-wake geometry and its effects on blade airloads.

Blade Loads and Response Results

Blade loads were computed for twelve rotor systems - flight condition combinations, with more than one set of data being used for some cases. Output from the wake geometry program was used in all cases to provide starting values for bound circulations and wake-induced velocity influence coefficients. Blade properties and model parameters as previously discussed, together with blade natural frequencies and mode shapes provided the additional model properties used in the calculations. The convergence criterion for the program was based on the relative change in bound circulation values from one iteration to the next. This tends to insure convergence of blade airloads. It does not insure convergence of blade torsional or bending moments and shears in all cases. Runs for all but two cases of the twelve satisfied the convergence criterion that the bound circulation relative magnitude change be less than 0.05. Cases 1 and 9 did not converge, according to this measure of convergence.

Case 1.- In Case 1, the circulations' minimum relative magnitude change was about 0.16, which was sufficient to result in reasonably good airload estimates, but which was not sufficient to result in converged generalized coordinates. The predicted airloads for Case 1 and the measured airloads for the approximately corresponding flight case are shown in Figure 35. Gross characteristics appear to be reasonable, i.e. steady and low frequency components are approximately the same at both radial stations. The detailed agreement is significantly better near $r = 0.55$ than near $r = 0.85$. The differences at both r 's may be due to the different climb rates, which was zero in the calculations and 350 ft/min in the measured data. The measured airload at $r = 0.85$ appears to contain effects of blade-wake interactions near $\psi = 225^\circ$ and 315° . These localized variations were not predicted, and could be due to omission of climb rate from the model. Computed and measured blade shears and moments did not agree for this case, although steady flap and lag motions were approximately correct. Measured and calculated blade moments did not agree, possibly because the generalized coordinates had not converged. Finally, the response formulation used for these calculations had the lead-lag damper effects included in the generalized force rather than contributing to the damping term in the equation of motion. This

permitted lead-lag variations which were large, but which coupled only weakly with the air loads. Thus, the lead-lag modes were diverging while the circulations were converging. The program has subsequently been modified so that lead-lag damping can be included in the damping term, and so that convergence depends upon convergence of both circulations and motions.

Case 9.- The model used for Case 9 calculations was that with a standard radius rotor with no airfoil inboard of $0.4R$, and a rotor of length $0.7R$ at the same shaftwise elevation, and with 90° blade azimuthal spacing. The rotors' chords were equal, and were adjusted to keep the total blade areas the same as in other calculations. Neither airloads nor generalized coordinates converged for this case. Several combinations of blade cyclic and collective angles and blade torsional damping were used in an attempt to obtain a converged, trimmed-out calculation. Program limitations on damping magnitude, σ_K , in equation (28), (over-critical damping was not allowed) restricted these efforts somewhat. Output from both preliminary calculations and from the non-converged runs indicated that the longer rotor was carrying approximately two-thirds of the total load. Flapping and torsional oscillations on the long rotor tended to become more severe as the iteration procedure between airloads and response progressed. It appeared that the expected lift (and corresponding drag and moment) were too severe for the system.

Cases 2 thru 8, 10, and 11.- Blade loads for Cases 2 through 8, 10, and 11 are given in Figures 36 through 44, in terms of the magnitudes of the harmonics of the root shears and moments. Generally, the shears and moments corresponding to blade flatwise bending, V_y and M_z , respectively, had a large steady component, a first harmonic on the order of 30% to 50% of the steady, and very small higher harmonics. The shears and moments corresponding to the chordwise bending, V_z and M_y , respectively, generally had a large steady component, relatively large first and second harmonic components, and, in most cases, a rather large seventh harmonic component, with other harmonic components being relatively small. In all cases, the third through sixth harmonic torsional moment components were higher in proportion to the steady than for the other moments. For cases with identical rotors with various rotor arrangements, the variations of azimuthal spacing resulted in less extreme variations in blade shears and moments than did variations in advance ratio, as may be seen from Cases 4 through 8. Converged cases with rotors of different lengths were similar except that the second harmonic component of the second rotor's chordwise shear and moment was extremely high.

Beyond these generally similar characteristics each case has distinguishing details. As a check, Case 2 is a two-bladed rotor model of a single four-bladed rotor system and this gave almost identical airloads, shears, and moments on both rotors. This agreement between rotors is a measure of the numerical and

model accuracy. As seen from Figure 36, the numerical and model accuracy appears to be excellent. This does not prove that the model is correct. It does indicate that sufficient rotor revolutions were used in the wake program calculations to yield periodic wake effects, and that the blade response program gives consistent results for this system of "identical rotors". Case 3 and subsequent cases in which rotor systems were non-identical showed differences for the different rotors, as would be expected. In Cases 3 through 6, these differences are due to shaftwise rotor separation or nonuniform azimuthal spacing. All these cases had identical advance ratios, cyclic and collective pitch angles and shaft angles on both rotors, as shown in Table 6. In some instances the harmonics of rotor loads differed by as much as a factor of two for the same harmonic on the different rotors. Usually the two rotors' loads were quite similar. Calculated differences for shaftwise separation of one chord, as seen in Figures 35 and 36 were small, with the upper rotor having slightly higher first harmonic loads, and with other load harmonics being slightly different for the two rotors. The differences between harmonic magnitudes for the two rotors generally increased with decreasing azimuthal blade spacing, $\Delta\psi$, as may be seen from Figures 37 through 40. Figures 38, 41, and 42 show loads for Cases 4, 7, and 8, where only the advance ratios were different and had values of 0.2, 0.3, and 0.1, respectively. The higher advance ratio case had the largest differences in harmonic load magnitudes for the different rotors and these occurred in the first harmonic loads. The third and fourth torsional moment harmonics were lower for the high advance ratio than for the intermediate and lower advance ratio. This may be an indication of fewer vortex-blade interactions for the high advance ratio case, which would be consistent with the wake geometries generated for these runs. Finally, the second harmonic chordwise shears and moments increased with advance ratio, as would be expected from the airloads. Results for Cases 10 and 11 are shown in Figures 43 and 44, respectively. Case 10 had equal collective on both rotors. The long rotor thrust is approximately 1.5 times the short rotor thrust, and except for the second harmonic loads, the long rotor had higher loading harmonics than the short rotor. Case 11 had approximately equal thrust on both rotors. Again, most other load harmonics, except the second, were larger on the long rotor. The unusually high shears and moments for the second harmonic of the short rotor's chordwise shear and moment for both Cases 10 and 11 are a result of aerodynamic excitation of the first chordwise elastic mode. The natural frequency for this mode for the short rotor is 2.04 times the rotor speed. All cases had significant second harmonic chordwise shears and moments, as would be expected for helicopters in forward flight. However, the natural frequency of the first chordwise mode of the longer rotor was 1.51 times the rotor speed, so it was not aerodynamically excited. These exceedingly large loads could be reduced significantly with stiffness changes near the blade root so as to remove the

chordwise natural frequency from the second harmonic range. (Similarly, mass changes on the outer portion of the blade could be used to change this frequency from near 2Ω .)

Case 12.- Case 12 was run to try to determine the effects of flexible blade motion on wake geometry, and thereby on the wake's contribution to blade loads. All other cases, for example, used a wake geometry that was generated by blades with initially specified motions. Case 12 calculations were done instead by using blade positions as determined from Case 2 blade loads in a subsequent wake geometry run. The blade positions at which wake-induced effects were calculated were not changed. However, the elevation at which the trailing vortices were deposited corresponded to the flapping positions of the flexible blade. These were determined in the Case 2 blade loads run. In this manner, higher harmonic blade motion effects were approximated in the wake geometry program's computations. (These higher harmonic variations, however, were relatively small.) The wake-induced velocity influence coefficients from this wake geometry run were then used to compute blade loads and response. The time histories of the airloads on the reference rotor for Cases 2 and 12 are shown in Figure 45. The general trends were very similar, but there were differences over the aft half of the rotor disc. These differences were due entirely to differences of wake-induced influence coefficients. It is apparent, then, that rotor blade position did have an affect on airload time histories, and it appeared that the aft half of the rotor disc was most affected, and that the higher harmonics of airloads were influenced more than the lower harmonics. Such results indicated that where wake-rotor interactions are important, it may be necessary to use more realistic blade positions in wake geometry calculations than are permitted by definition of coning and first harmonic flapping motions as given by the present performance program. Blade coning (wake position) was computed to be lower by the blade loads program than by the performance (blade position) program. It was felt that this was the dominant source of the differences in the resulting wake geometry and airloads. The general characteristics of the wake geometries were very similar, except that the blade coning angle was much smaller.

Study of the time histories of the radial distribution of shears and moments provided additional information which could be utilized in this study. Figures 46 and 47 show radial distributions of the blade flatwise bending moments as a function of azimuth which were computed for the rigid rotor of Cases 2 and 7. For both cases, the moment values peak at the root, with an outboard peak for some azimuthal positions which is near the outboard peak of the third flatwise normal mode. The two rotors had essentially identical time histories for Case 2, but were somewhat different for Case 7. There were no severe peaks in the outboard flatwise moment distributions for any cases. There

were also no clear indications of traveling-wave-type interactions. The use of only three flatwise modes may not be sufficient to clearly display such a phenomenon, however. More radial load points and more flatwise bending normal modes may be required before such a phenomenon could be displayed by such time histories.

CONCLUSIONS AND RECOMMENDATIONS

The following conclusions may be stated as a result of this investigation:

1. The wake geometry, wake flow, wake-induced velocity model is a satisfactory model for advance ratios of approximately 0.1 to 0.3.
2. The wake program allows considerable flexibility for considering rotor systems of different designs.
3. The basic wake formulation permits extension to other steady-state flight conditions in addition to level forward flight. As a real-time analysis, it also permits extensions to non-steady flight conditions.
4. Wake program running times and storage requirements, for advance ratios of more than 0.1, are moderate enough to allow program usage in design problems.
5. While the blade loads program provided reasonable results for converged cases, some limitations were found where convergence was difficult to obtain for certain rotor systems and flight conditions.
6. The blade loads formulation permits the program to be extended to other steady-state flight conditions in addition to forward flight, i.e. maneuvers.
7. The blade loads program requires small running times and moderate storage. This allows the program to be easily and economically applied for design problems.
8. Calculated time-average wake flows were satisfactory.

Recommendations with respect to two areas are suggested. The blade loads program as presently formulated has limitations which restrict its usefulness and generality. The following changes are suggested:

1. Develop and program solutions to the governing equations for damping values which exceed critical damping.

2. Develop and program solution of the governing equations for the generalized coordinates as a coupled set of equations. As a minimum, damping coupling should be provided but preferably complete coupling. This means permitting use of non-orthogonal modes.

3. Remove linear damping effects from the forcing function and include these effects as damping terms in the governing equations.

4. Introduce in-plane wake-induced velocity effects on blade airloads in both the blade loads and wake geometry programs.

Recommendations for further research are suggested as follows:

1. Generalize the wake program to simulate transient as well as steady-state flight conditions.

2. Study the effects of a freely deformed wake on airloads and blade response under transient conditions including gusts and transition from one steady-flight condition to another.

3. Investigate the simulation capabilities of the wake program at low advance ratios (to hover), and establish the program's capabilities for such flight conditions.

4. Investigate simulation capabilities of both the wake program and the blade loads program at higher advance ratios (above 0.3).

5. Generalize the wake and blade loads programs to permit simulation of main rotor-tail rotor interaction effects and the helicopter fuselage and/or tail fin surfaces.

APPENDIX

Equations Programmed for Computation

Equations which were programmed for computation, and which are a result of equations discussed in the analysis section of this report are given here for completeness.

Equations Used in Wake Calculations

Blade flapping motions.- Blade flapping motions are obtained from the solution of the equations for β_1 , β_2 , and β_3 in subroutine BETAS, where

$$\begin{bmatrix} \beta_1 \\ \beta_2 \\ \beta_3 \end{bmatrix} = \begin{bmatrix} K_1 - M_{10} & -M_{11}/2 & 0 \\ -M_{11} & K_2 - M_{10} & \Omega M_{20} - M_{13}/2 \\ -M_{12} & -\Omega M_{20} - M_{13}/2 & K_2 - M_{10} \end{bmatrix}^{-1} \begin{bmatrix} M_{00} \\ M_{01} \\ M_{02} \end{bmatrix} \quad (A1)$$

where

$$M_{00} = \rho_1 V^2 A_0 / 2 + \rho_2 [\Omega V (\alpha_1 + \alpha_S) - \Omega w_i - A_R V^2 / 2] + \rho_3 \Omega^2 A_0 - r_5 \Omega^2 A_R \quad ,$$

$$M_{01} = \rho_1 (3V^2 \alpha_1 / 4 - V w_i + V^2 \alpha_S) + 2\rho_2 V A_0 + \rho_3 \Omega (\Omega \alpha_1 - 2A_R V) \quad ,$$

$$M_{02} = \rho_1 V^2 \alpha_2 / 4 + \rho_3 \Omega^2 \alpha_2 \quad ,$$

$$M_{11} = \rho_1 V c \Omega / 2 \quad ,$$

$$M_{12} = -\rho_2 V \Omega \quad ,$$

$$M_{13} = -\rho_1 V^2/2 \quad ,$$

$$M_{20} = -\rho_3 \Omega \quad ,$$

$$K_2 - M_{10} = K_1 - M_{10} - \Omega^2 I_0 \quad ,$$

$$K_1 - M_{10} = k + \Omega^2 (I_b + m_b x_b \delta - \rho_2 c/2) \quad ,$$

$$\rho_i = r_{i+1} - \delta r_i \quad \text{for } i = 1, 2, 3,$$

$$r_i = \pi \rho c (R^i - r_0^i)/i \quad ,$$

$$A_R = \alpha_R / (R - r_0) \quad ,$$

$$A_0 = \alpha_0 + \alpha_R r_0 / (R - r_0) \quad ,$$

α_R = total blade twist, radians, positive for decreasing angle of attack with radius,

α_1, α_2 = amplitude of lateral and longitudinal cyclic pitch, respectively, radians,

and all other quantities are as defined in the list of symbols.

Wake-induced velocities.— The computational equations for the velocity components induced by the blade and vortex elements are given in reference 19, and are included here, with minor changes in notation, for completeness. All quantities used in the computation of wake-induced velocities are in nondimensional form. Lengths are nondimensionalized by the radius of the longest blade, R ; velocities by ΩR ; time by $1/\Omega$; and circulations, Γ , by ΩR^2 .

The points in a nondimensionalized reference system of location of trailing vortices from the blades, given by x_{1j} , y_{1j} , and z_{1j} are determined by the blade flapping positions, azimuthal blade position, and input control numbers. If the vortex element end point P_{ij} has coordinates (x_{ij}, y_{ij}, z_{ij}) and if $v_x(x, y, z, \psi)$, $v_y(x, y, z, \psi)$, $v_z(x, y, z, \psi)$ denote the dimensionless fluid velocity components at the point (x, y, z) corresponding to the rotor at

azimuth position ψ , then wake displacements are given by

$$\begin{aligned}x_{i+1,j}(\psi + \Delta\psi) &= x_{ij}(\psi) + v_x(x_{ij}, y_{ij}, z_{ij}, \psi) \Delta\psi \\y_{i+1,j}(\psi + \Delta\psi) &= y_{ij}(\psi) + v_y(x_{ij}, y_{ij}, z_{ij}, \psi) \Delta\psi \\z_{i+1,j}(\psi + \Delta\psi) &= z_{ij}(\psi) + v_z(x_{ij}, y_{ij}, z_{ij}, \psi) \Delta\psi\end{aligned}\tag{A2}$$

for $i = 1, 2, \dots, NW$ and $j = 1, 2, \dots, NGJ$,

where NW is the number of trailing wake elements per blade and NGJ is the number of trailing vortices from all blades; and $\Delta\psi = 2\pi/NA$, where NA is the integer number of evenly spaced azimuthal stations into which the rotor plane is divided. The fluid velocities are given by

$$\begin{aligned}v_x &= V_x + \mu \cos \alpha_s \\v_y &= V_y \\v_z &= V_z + \mu \sin \alpha_s\end{aligned}\tag{A3}$$

where V_x , V_y , and V_z are contributions from the wake, μ is the advance ratio, and α_s is the shaft tilt angle.

The strengths of vortex elements once formed are assumed to remain unchanged as the wake develops, therefore only subscripting changes need be done, i.e.,

$$\Gamma_{ij}(\psi + \Delta\psi) = \Gamma_{i-1,j}(\psi)\tag{A4}$$

for $i = 2, 3, \dots, NW$, and $j = 1, 2, \dots, NGJ$. The circulations Γ_{1j} are determined as discussed in the analysis part, where the Γ 's in equation (12) correspond to the Γ_{1j} 's. The core sizes in the full mesh wake are assigned according to

$$a_{ij}(\psi + \Delta\psi) = [L_{i-1,j}(\psi)/L_{ij}(\psi + \Delta\psi)]^{1/2} a_{i-1,j}(\psi)\tag{A5}$$

for $i = 2, 3, \dots, NW$ and $j = 1, 2, \dots, NGJ$, which conserves the volume of rotational fluid. The core sizes at the blade ($i=1$) are assumed to be of the form

$$a_{ij} = AKI * (\Delta\Gamma)^{1/2}$$

with the constant of proportionality, AKI , specified by input data. Here $\Delta\Gamma$ is the spanwise difference of the blade's bound Γ 's, and represents the vortex element's circulation. Trailing vortex lengths, L_{ij} , are given by

$$L_{ij} = [(x_{i+1,j} - x_{ij})^2 + (y_{i+1,j} - y_{ij})^2 + (z_{i+1,j} - z_{ij})^2]^{1/2} \quad (A6)$$

while shed vortex lengths, D_{ij} , are given by

$$D_{ij} = [(x_{i,j+1} - x_{ij})^2 + (y_{i,j+1} - y_{ij})^2 + (z_{i,j+1} - z_{ij})^2]^{1/2} , \quad (A7)$$

and shed vortex core radii are computed as in equation (A5) but with D_{ij} replacing L_{ij} , etc. Let $q_{x_{ij}}$, $q_{y_{ij}}$, and $q_{z_{ij}}$ be defined as

$$\begin{aligned} q_{x_{ij}} &= v_x^G , \\ q_{y_{ij}} &= v_y^G , \\ \text{and} \quad q_{z_{ij}} &= v_z^G , \end{aligned} \quad (A8)$$

where

$$\begin{aligned} v_x &= (y - y_{ij})(z_{ij} - z_{i+1,j}) - (z - z_{ij})(y_{ij} - y_{i+1,j}) , \\ v_y &= (z - z_{ij})(x_{ij} - x_{i+1,j}) - (x - x_{ij})(z_{ij} - z_{i+1,j}) , \\ v_z &= (x - x_{ij})(y_{ij} - y_{i+1,j}) - (y - y_{ij})(x_{ij} - x_{i+1,j}) , \end{aligned}$$

$$G = \frac{\Gamma_{ij}(r_{ij} + r_{i+1,j})}{2\pi r_{ij} r_{i+1,j} [(r_{ij} + r_{i+1,j})^2 - L_{ij}^2]}$$

and $r_{ij} = [(x - x_{ij})^2 + (y - y_{ij})^2 + (z - z_{ij})^2]^{1/2}$.

If point (x,y,z) does not lie on a vortex element then vortex-induced velocity components are given by

$$V_x(x,y,z) = \sum_{i=1}^{NW} \sum_{j=1}^{NGJ} q_{x_{ij}} \tag{A9}$$

and similarly for V_y and V_z . If the point P_{rs} is a vortex element end point with coordinates (x_{rs}, y_{rs}, z_{rs}) then

$$\begin{aligned} V_x(x_{rs}, y_{rs}, z_{rs}) = & \sum_{i=1}^{NW} \sum_{\substack{j=1 \\ j \neq s}}^{NGJ} q_{x_{ij}} \\ & + \sum_{\substack{i=1 \\ i \neq r-1, r}}^{NW} q_{x_{is}} + q_{s_x} \end{aligned} \tag{A10}$$

and similarly for V_y and V_z , where q_{s_x} , q_{s_y} , and q_{s_z} account for self-induced effects. If $r > 1$ and P_{rs} is not on the "edge" of a wake,

$$q_{s_x} = m_x F$$

$$q_{s_y} = m_y F$$

and $q_{s_z} = m_z F \tag{A11}$

where

$$m_x = (y_{r-1,s} - y_{rs})(z_{rs} - z_{r+1,s}) - (z_{r-1,s} - z_{rs})(y_{rs} - y_{r+1,s})$$

$$m_y = (z_{r-1,s} - z_{rs})(x_{rs} - x_{r+1,s}) - (x_{r-1,s} - x_{rs})(z_{rs} - z_{r-1,s})$$

$$m_z = (x_{r-1,s} - x_{rs})(y_{rs} - y_{r+1,s}) - (y_{r-1,s} - y_{rs})(x_{rs} - x_{r-1,s})$$

$$F = [\Gamma_{r-1,s}(\ln e_1 + 1/4) + \Gamma_{rs}(\ln e_2 + 1/4)]/b$$

$$b = 8\pi S[m_x^2 + m_y^2 + m_z^2]^{1/2}$$

$$e_1 = 8Sf/a_{r-1,s}$$

$$e_2 = 8Sg/a_{rs}$$

(the S factor, called R in reference 10, was omitted in error from the e terms)

$$S = \frac{L_{r-1,s} L_{rs} \delta_{rs}}{[4L_{r-1,s}^2 L_{rs}^2 - (L_{r-1,s}^2 + L_{rs}^2 - \delta_{rs}^2)]^{1/2}}$$

$$\delta_{rs} = [(x_{r-1,s} - x_{r+1,s})^2 + (y_{r-1,s} - y_{r+1,s})^2 + (z_{r-1,s} - z_{r+1,s})^2]^{1/2}$$

$$f = \left\{ \begin{array}{l} \left[2S - \sqrt{4S^2 - L_{r-1,s}^2} \right] / L_{r-1,s} \quad \text{for } L_{r-1,s}^2 \leq \delta_{rs}^2 + L_{rs}^2 \\ \left[2S + \sqrt{4S^2 - L_{r-1,s}^2} \right] / L_{r-1,s} \quad \text{for } L_{r-1,s}^2 > \delta_{rs}^2 + L_{rs}^2 \end{array} \right\}$$

$$g = \left\{ \begin{array}{l} \left[\frac{2S - \sqrt{4S^2 - L_{rs}^2}}{L_{rs}} \right] \text{ for } L_{rs}^2 \leq \delta_{rs}^2 + L_{r-1,s}^2 \\ \left[\frac{2S + \sqrt{4S^2 - L_{rs}^2}}{L_{rs}} \right] \text{ for } L_{rs}^2 > \delta_{rs}^2 + L_{r-1,s}^2 \end{array} \right\}$$

If $r=1$, inclusion of blade-induced effects is accounted for by defining

$$q_{s_x}(x_{1s}, y_{1s}, z_{1s}) = q_{s_x}(x_{2s}, y_{2s}, z_{2s}) \Big|_{\Gamma_{2s}} \equiv 0$$

similarly for q_{s_y} , and

$$q_{s_z}(x_{1s}, y_{1s}, z_{1s}) = q_{s_z}(x_{2s}, y_{2s}, z_{2s}) \Big|_{\Gamma_{2s}} \equiv 0 + \frac{\Delta\psi}{2\pi R r_s} \sum_{j=A}^B \Gamma_j \ln p_j \quad (A12)$$

$$\text{where } p = \left(1 + \sqrt{1+\beta_1^2}\right) \left(1 + \sqrt{1+\alpha_2^2}\right) / \left[\left(1 + \sqrt{1+\beta_2^2}\right) \left(1 + \sqrt{1+\alpha_1^2}\right)\right]$$

$$\text{and where } \beta_1 = r_s \Delta\psi / d_{1j}$$

$$\beta_2 = r_s \Delta\psi / (d_{1j} - D_{1j})$$

$$\alpha_1 = 3b_s / 4d_{1j}$$

$$\alpha_2 = 3b_s / 4(d_{1j} - D_{1j})$$

where r_s is the radius to the point P_{1s} , b_s is the blade semi-chord at that radius, and d_{1j} is the distance from P_{1s} and the furthest removed point on element $1j$. If P_{rs} is on the edge of a wake, so that, for example $P_{r,s-1}$ and P_{rs} are on the same blade's wake, but $P_{r,s+1}$ is on another blade's wake, then

$$q_{s_x}(x_{rs}, y_{rs}, z_{rs}) = q_{s_x}(x_{r,s-1}, y_{r,s-1}, z_{r,s-1}) \Big|_{\Gamma_{rs} = 0}$$

and similarly for q_{s_y} and q_{s_z} . In equations (A11) and (A12) the notation $q_{s_x}(x,y,z) \Big|_{\Gamma_{ij} = 0}$ means that this is the value

$q_{s_x}(x,y,z)$ would have if Γ_{ij} were set to zero. Thus, the curvature is determined from the three nearest end points, and the induced velocity is determined by the adjoining vortex elements only. This type of calculation is necessary at both inside and outside edges of the wake, as well as at the blade.

Modified wake parameters.- The method used to specify the locations, strengths, core radii, and velocity influence coefficients is flexible and consistent, but is not the only possible method. Implementation of the method used is done within subroutines, and different methods may be implemented by programming and using different subroutines. The positions of the modified wake element end points which "attach" the modified wake to the full mesh wake are determined by the matrix relationship

$$[xm] = [A] [x]$$

where xm is a column of NTVM x-coordinate elements,
 A is an NTVM by NTV matrix, and
 x is a column of NTV elements, and
 similarly for ym and zm .

The A is the same for all blades. Ordinarily $NTVM < NTV$, and A has nonzero terms only on the diagonal and just off the diagonal, with one or two nonzero elements in each row. In this case the modified element end points are on a straight line between two of the elements of the full mesh wake.

Circulation values are assigned in a similar manner, and give modified wake circulation values, Γ_m , of trailed vortex elements based on full mesh wake circulation values, Γ , according to

$$[\Gamma_m] = [B] [\Gamma]$$

where Γ_m is a column having NTVM elements,
 B is an NTVM by (NTV-1) coefficient array, and
 Γ is a column having (NTV-1) elements.

The B matrix elements are defined by input. Modified wake element core sizes are defined by input, except for the tip vortices which are defined to be the same as the corresponding full mesh wake tip vortex core radii.

Velocity influence coefficients for the full mesh wake, σ , are conveniently used by the blade loads program, rather than velocity influence coefficients for a combination of full mesh and modified wake representations. The definition of σ 's which is consistent with the definition of modified wake circulations is given by

$$[\sigma] = [B]^T [\sigma_m]$$

where σ is a column having (NTV-1) elements
 σ_m is a column having NTVM elements, and
 $[B]^T$ is the transpose of $[B]$.

Equations Used in Blade Loads and Response Calculations

Blade and wake circulation equations.- The equations which were used to compute blade circulation are also in nondimensional form and may be written as

$$\frac{\Gamma(r_i, \psi_j)}{b_i} = (U_{ij}^2 + V_{ij}^2)^{1/2} \left\{ c_{\ell}(\alpha_{ij}) + \frac{[U_{ij} a(\alpha_{ij}) + V_{ij} c_{\ell}(\alpha_{ij})] \bar{w}_{ij}}{U_{ij}^2 + V_{ij}^2} \right\}$$

$$+ \pi b_i \{ \xi(r_i, \psi_j) + [\theta_0(\psi_{j+1}) - \theta_0(\psi_{j-1})] / 2\Delta\psi \}$$

$$- \left\{ \frac{[U_{ij} a(\alpha_{ij}) + V_{ij} c_{\ell}(\alpha_{ij})]}{(U_{ij}^2 + V_{ij}^2)^{1/2}} \sum_m \sum_n b_m \sigma_{mn}(r_i, \psi_j) \left[\frac{\Gamma(r_m, \psi_n)}{b_m} \right] \right\}$$

(A13)

where

$$\bar{w}_{ij} = \sum_m \sum_n b_m \sigma_{mn} (r_i, \psi_j) \left[\frac{\Gamma(r_m, \psi_n)}{b_m} \right] , \quad (A14)$$

the Γ 's in the expression for \bar{w}_{ij} are from the previous iteration, $c_\ell(\alpha_{ij})$ is the lift coefficient, and is a function of Mach number, as well as angle of attack, $a(\alpha_{ij})$ is the slope of the lift coefficient versus angle of attack curve, and is also a function of Mach number,

$$U_{ij} = r_i + \mu \cos \alpha_s \sin \psi_j , \quad (A15)$$

$$V_{ij} = \dot{h}(r_i, \psi_j) - \mu \sin \alpha_s - \bar{w}_{ij} , \quad (A16)$$

$$\alpha_{ij} = \theta_0(\psi_j) + \phi(r_i, \psi_j) + \theta_1(r_i) + \tan^{-1}(V_{ij}/U_{ij}) , \quad (A17)$$

and other quantities are as defined in the list of symbols.

Airfoil characteristics.- The lift, drag, and moment coefficients, and the slope of the lift curve are computed by analytical approximations to experimental data for the NACA 0012 airfoil, in the subroutine SERIES, as follows:

$$c_\ell(-\alpha, M_N) = -c_\ell(\alpha, M_N) \quad \text{and is given for ranges in } \alpha \text{ as}$$

$$0 \leq \alpha < .22689(1-M_N) \quad , \quad c_\ell = 5.7296\alpha / \sqrt{1-M_N^2}$$

$$.22689(1-M_N) \leq \alpha < .34906 \quad , \quad c_\ell = \frac{.29269(1-M_N) + (1.3M_N - .59)\alpha}{(.12217 + .22689M) \sqrt{1-M_N^2}}$$

$$.34906 \leq \alpha < 2.7402 \quad , \quad c_\ell = \frac{1}{\sqrt{1-M_N^2}} (.080373 \sin \alpha + 1.04308 \sin 2\alpha - .011059 \sin 3\alpha + .023127 \sin 4\alpha)$$

$$\begin{aligned}
2.7402 \leq \alpha < 3.0020 \quad , \quad c_\ell &= (.4704 + .10313\alpha) / \sqrt{1-M_N^2} \\
3.0020 \leq \alpha < \pi \quad , \quad c_\ell &= (-17.550 + 5.5864\alpha) / \sqrt{1-M_N^2} \quad ; \quad (A18)
\end{aligned}$$

$c_d(-\alpha) = c_d(\alpha)$ and is given for ranges in α as

$$\begin{aligned}
0 \leq \alpha < .22689(1-M_N) \quad , \quad c_d &= (.0060 + .13131\alpha^2) \\
.22689(1-M_N) \leq \alpha < \pi \quad , \quad c_d &= \frac{1}{\sqrt{1-M_N^2}} (1.1233 - .029894 \cos \alpha \\
&\quad - 1.00603 \cos 2\alpha + .003115 \cos 3\alpha \\
&\quad - .091487 \cos 4\alpha) \quad (A19)
\end{aligned}$$

$c_m(-\alpha) = -c_m(\alpha)$, evaluated for (chord/2), and is given for ranges in α as

$$\begin{aligned}
0 \leq \alpha < .22689(1-M_N) \quad , \quad c_m &= 1.4324\alpha / \sqrt{1-M_N^2} \\
.22689(1-M_N) \leq \alpha < .34906 \quad , \quad c_m &= \frac{.29269(1-M_N) + (1.3M_N - .59)\alpha}{[.48868 + .90756M_N] \sqrt{1-M_N^2}} \\
.34906 \leq \alpha < 2.7402 \quad , \quad c_m &= \frac{1}{\sqrt{1-M_N^2}} (-.02827 \sin \alpha + .14022 \sin 2\alpha \\
&\quad - .00622 \sin 3\alpha + .01012 \sin 4\alpha) \\
2.7402 \leq \alpha < 3.0020 \quad , \quad c_m &= (.4786 + .02578\alpha) / \sqrt{1-M_N^2}
\end{aligned}$$

$$3.0020 < \alpha < \pi, \quad c_m = (-12.5109 + 3.9824\alpha) / \sqrt{1 - M_N^2}; \quad (A20)$$

$$a(-\alpha, M_N) = a(\alpha, M_N)$$

and for all ranges of α may be obtained from $c_\ell(\alpha, M_N)$ according to

$$a(\alpha, M_N) = \frac{\partial c_\ell(\alpha, M_N)}{\partial \alpha} \quad (A21)$$

The $\sigma_{mn}(r_i, \psi_j)$ quantities are input from the wake program. The equation for the (Γ/b) quantities is solved by an iterative process, during which values of w_{ij} , V_{ij} , α_{ij} , etc. are recomputed as the sets of (Γ/b) quantities are recomputed.

Blade loads quantities.— When the Γ 's have converged, blade load quantities are computed according to the equations

$$\begin{aligned} \frac{F_z(r_i, \psi_j)}{\rho \Omega^2 R^3 b_i} = & \frac{U_{ij} c_\ell(\alpha_{ij}) u_{ij}}{b_i} + \frac{1}{2\Delta\psi} \left\{ b_i \left[\frac{\Gamma(r_i, \psi_{j+1})}{b_i} - \frac{\Gamma(r_i, \psi_{j-1})}{b_i} \right] \right. \\ & + 2b_i \left[c_m(\alpha_{i,j+1}) \sqrt{U_{i,j+1}^2 + V_{i,j+1}^2} \right. \\ & \left. \left. - c_m(\alpha_{i,j-1}) \sqrt{U_{i,j-1}^2 + V_{i,j-1}^2} \right] \right\} \\ & + c_d(\alpha_{ij}) V_{ij} \sqrt{U_{ij}^2 + V_{ij}^2}, \quad (A22) \end{aligned}$$

$$\frac{F_x(r_i, \psi_j)}{\rho \Omega^2 R^3 b_i} = - \frac{V_{ij} c_\ell(\alpha_{ij}) u_{ij}}{b_i} + c_d(\alpha_{ij}) U_{ij} \sqrt{U_{ij}^2 + V_{ij}^2}, \quad (A23)$$

$$\text{where } u_{ij} = \sqrt{U_{ij}^2 + V_{ij}^2}$$

$$\begin{aligned}
\frac{M_0(r_i, \psi_j)}{\rho \Omega^2 R^4 b_i^2} &= 2c_m(\alpha_{ij})(U_{ij}^2 + V_{ij}^2) - \frac{b_i}{8\Delta\psi} \left\{ b_i \left[\frac{\Gamma(r_i, \psi_{j+1})}{b_i} - \frac{\Gamma(r_i, \psi_{j-1})}{b_i} \right] \right. \\
&+ \frac{3\pi b_i}{\Delta\psi} \left[\theta(r_i, \psi_{j+1}) - 2\theta(r_i, \psi_j) + \theta(r_i, \psi_{j-1}) \right] \\
&\left. + \frac{3\pi b_i}{2\Delta\psi} \left[\xi(r_i, \psi_{j+1}) - \xi(r_i, \psi_{j-1}) \right] \right\} \quad (A24)
\end{aligned}$$

Blade response.- Conversion of the aerodynamic loads to a form suitable for response calculations is done by lumping the distributed loads at the mass points of the lumped parameter blade model. The distributed aerodynamic moment is transferred to quarter-chord, then the distributed loads are integrated, using a straight-line approximation between load points, to obtain lumped loads at the mass points. The drag force at the i^{th} mass point, for example, is

$$f_{x_i} = \int_{R_i}^{R_{i+1}} F'_x(r) dr \quad (A25)$$

where R_i and R_{i+1} are midway between masses m_i and m_{i+1} , and between m_{i+1} and m_i , respectively, and where $F'_x(r)$ is the straight-line approximation to the distributed drag load. Coordinate transformations are then applied which result in loads in the local blade coordinate system, and are given by

$$\begin{aligned}
F_{v_i} &= -f_{z_i} \cos \phi_i - f_{x_i} \sin \phi_i \quad , \\
F_{w_i} &= f_{z_i} \sin \phi_i - f_{x_i} \cos \phi_i \quad , \\
M_{\phi_i} &= m_{i0} + z_{a_i} F_{v_i} \quad (A26)
\end{aligned}$$

where z_{a_i} = distance of the elastic axis forward of quarter chord.

The computation of the total force and moment at each mass, for every azimuthal and radial location is done according to

$$Q_v = m\Omega^2 \sin \phi (h + \epsilon \cos \phi) + m\ddot{\theta}_c [\epsilon + h \cos (\phi - \theta_0) / \cos \phi] \\ - 2m\Omega \dot{\psi} \epsilon \sin \phi + F_v \quad ,$$

$$Q_\psi = m\Omega^2 \epsilon r - 2\Omega \dot{\theta}_c [(I_x + m\epsilon^2) \sin \phi + m\epsilon h \sin \theta_0 / \cos \phi] \\ - 2\Omega \dot{\phi}_i (I_x + m\epsilon^2) + 2m\Omega \epsilon (\dot{v} \sin \phi + \dot{w} \cos \phi)$$

$$Q_w = m\Omega^2 \cos \phi (h + \epsilon \cos \phi) - m h \ddot{\theta}_c \sin (\phi - \theta_0) / \cos \phi \\ - 2m\Omega \epsilon \dot{\psi} \cos \phi + F_w$$

$$Q_\phi = - \Omega^2 \sin \phi [(I_x + m\epsilon^2) \cos \phi_i + m\epsilon h] \\ - \ddot{\theta}_c [I_x + m\epsilon^2 + m\epsilon h \cos (\phi - \theta_0) / \cos \phi] \\ + 2\Omega \dot{\psi} \sin \phi (I_x + m\epsilon^2) + M_\phi \quad (A27)$$

where the Q's, ϕ , $\dot{\psi}$, ϕ , v , \dot{w} and the F's and M_ϕ are understood to be subscripted by i and j; m , h , ϵ , r , and I_x are understood to be subscripted by i, and θ_0 and θ_c and its time derivatives are understood to be subscripted by j. Here, θ_c , the cyclic pitch is given by

$$\theta_c = A_c \sin \Omega t + B_c \cos \Omega t \quad ;$$

h , the horizontal separation between the elastic axis and the pitch axis, say at the i^{th} station, is given by

$$h_i = \sum_{\ell=1}^i l_{z_\ell} \cos \phi_{\ell-1}$$

l_z is the change in distance of the elastic axis forward of the pitch axis in the local blade coordinate system; ϕ_{ij} is the total angle between the rotor plane and the chord at the i^{th} radial and j^{th} azimuthal position, and is given by

$$\phi_{ij} = \theta_{0j} + \sum_{\ell=1}^i \Delta \phi_\ell$$

where θ_0 is the nominal pitch angle, and $\Delta\phi_\ell$ is the increase in twist angle at the ℓ^{th} station. Also, r_i , the radius to the i^{th} mass is given by

$$r_i = \delta + \sum_{n=1}^i \ell_n$$

and other quantities are as defined in the list of symbols. The values of \dot{v} , \dot{w} , $\dot{\phi}$, and $\dot{\psi}$ in the above equations are from the previous iteration. To account for a lag damper, the following is added to Q_{v_2} and Q_{w_2} , respectively:

$$\Delta Q_{v_2} = (k_\ell / \ell_2) \dot{\psi}_1 \sin \phi_2$$

$$\Delta Q_{w_2} = (k_\ell / \ell_2) \dot{\psi}_1 \cos \phi_2$$

where k_ℓ is the lag damping coefficient, ft-lb/rad/sec.

The generalized forces acting on each normal mode are computed for each azimuth, according to

$$F_K(t) = \sum_i (Q_{v_i} A_{v_i}^{(K)} + Q_{w_i} A_{w_i}^{(K)} + Q_{\phi_i} A_{\phi_i}^{(K)} + Q_{\psi_i} A_{\psi_i}^{(K)}) + \sum_J \sigma_{KJ} \dot{\zeta}_J \quad (\text{A28})$$

where $\dot{\zeta}_K$ is from the previous iteration,

$$\sigma_{KJ} = -c_{D\dot{\theta}} A_{\phi_1}^{(K)} A_{\phi_1}^{(J)} \quad \text{for } J \neq K$$

$$\sigma_{KK} = 2 \tilde{\sigma}_K \omega_K$$

$\tilde{\sigma}$ is the average damping coefficient for the K^{th} mode (read as input), and

$A_{q_i}^{(K)}$ is the mode shape quantity for the "q" type of elastic deformation, at the i^{th} radial location, for the K^{th} mode.

The σ_{KJ} terms may be thought of as damping coupling terms. The damping term, σ_K , is presently defined in terms of the mode shape quantities as

$$\sigma_K = \tilde{\sigma}_K + c_{D\theta} \left[\frac{A_{\phi_1}^{(K)}}{\phi_1} \right]^2 / 2\omega_K$$

Note that the average damping coefficient, $\tilde{\sigma}_K$, occurs on both sides of the governing equation for $\zeta_K(t)$, so effectively cancels with convergence. (It should also be noted that the present program is inoperable for $\sigma_K > 1$, as calculation of $\sqrt{1-\sigma_K^2}$ then results in a fatal error.)

The governing equation for the K^{th} generalized coordinate, ζ_K , is given by

$$\ddot{\zeta}_K + 2\sigma_K\omega_K \dot{\zeta}_K + \omega_K^2 \zeta_K = F_K(t)$$

The solution of this equation is obtained in integral form. The solution assumes periodicity of both forcing function and response. The generalized coordinate, ζ_K , and its first time derivative, $\dot{\zeta}_K$, are given explicitly below. The second time derivative of the generalized coordinate, $\ddot{\zeta}_K$, is obtained from the governing equation itself, after solution for ζ_K and $\dot{\zeta}_K$.

Then, ζ_K and $\dot{\zeta}_K$ are computed from

$$\zeta_K(t) = \frac{1}{\bar{\omega}_K} \int_0^t e^{-\sigma_K\omega_K(t-\tau)} \sin \bar{\omega}_K(t-\tau) F_K(\tau) d\tau$$

$$\begin{aligned}
& + \frac{e^{-\sigma_K \omega_K t}}{\bar{\omega}_K (s_K^2 + c_K^2)} \left[\left(s_K I_{c_K} + c_K I_{s_K} \right) \cos \bar{\omega}_K t \right. \\
& \qquad \qquad \qquad \left. + \left(c_K I_{c_K} - s_K I_{s_K} \right) \sin \bar{\omega}_K t \right] , \quad (A29)
\end{aligned}$$

$$\begin{aligned}
\dot{\zeta}_K(t) = & -\sigma_K \omega_K \zeta_K(t) + \int_0^t e^{-\sigma_K \omega_K (t-\tau)} \cos \bar{\omega}_K (t-\tau) F_K(\tau) d\tau \\
& + \frac{e^{-\sigma_K \omega_K t}}{(s_K^2 + c_K^2)} \left[- \left(s_K I_{c_K} + c_K I_{s_K} \right) \sin \bar{\omega}_K t \right. \\
& \qquad \qquad \qquad \left. + \left(c_K I_{c_K} - s_K I_{s_K} \right) \cos \bar{\omega}_K t \right] , \quad (A30)
\end{aligned}$$

where

$$\bar{\omega}_K = \omega_K \sqrt{1 - \sigma_K^2} ,$$

$$s_K = e^{-\sigma_K \omega_K T} \sin \bar{\omega}_K T ,$$

$$c_K = 1 - e^{-\sigma_K \omega_K T} \cos \bar{\omega}_K T ,$$

$$I_{s_K} = \int_0^T e^{-\sigma_K \omega_K (T-\tau)} \sin \bar{\omega}_K (T-\tau) F_K(\tau) d\tau ,$$

$$I_{c_K} = \int_0^T e^{-\sigma_K \omega_K (T-\tau)} \cos \bar{\omega}_K (T-\tau) F_K(\tau) d\tau ,$$

$$T = 2\pi/\Omega ,$$

and the integrations are performed by an approximation known as Filon's rule. (See, for example, appendix of ref. 20.) Response variables are then computed from

$$\dot{v}(t) = \sum_K A_v^{(K)} \dot{\zeta}_K(t) \quad ,$$

$$\phi(t) = \sum_K A_\phi^{(K)} \zeta_K(t) \quad ,$$

and similarly for \dot{w} , $\dot{\phi}$, $\dot{\psi}$, ψ , and \mathcal{J} ($\mathcal{J} = \partial v / \partial r$).

Conversion of the response data to a form suitable for loads calculations is then done by computing loads input data by interpolation of response data. The mass points on either side of the aerodynamic points, r_i , are determined, and response quantities at r_i are computed by linear interpolation from the mass points. Thus, dimensionless response quantities, i.e., the plunging velocity \dot{h} , the pitch θ , and slope ξ , are given by

$$\dot{h} = [\dot{v} \cos \phi - \dot{w} \sin \phi + z_a \dot{\phi} \cos \phi + (z_a - h)(\dot{\theta}_C - \Omega \xi)] / \Omega R$$

$$+ \xi \mu \cos \alpha_T \cos \Omega t \quad , \quad (A31)$$

$$\theta = \theta_0 + \theta_C + \phi, \text{ and} \quad (A32)$$

$$\xi = - (\mathcal{J} \cos \phi + \psi \sin \phi). \quad (A33)$$

These values of \dot{h} , θ , and ξ (computed at all aerodynamic radial and azimuthal positions) are used in the next iterative calculations of blade loads.

Once convergence has been established between blade loads and response, blade shears and moments are computed in subroutine SHEAR according to

$$T(t) = \sum_K A_T^{(K)} \xi_K(t) \quad (A34)$$

for the torsional moment, and similarly for the flapwise and edge-wise bending moments M_z and M_y and for the flapwise and edgewise shears V_y and V_z .

Initial estimates.- During the first step of the various portions of the program which involve iterations due to nonlinearities in the unknown quantities, estimates are used to improve convergence. Subroutine WBAR computes an average wake-induced velocity \bar{w} which is uniform over the rotor disc, and which is given by

$$\bar{w} = \{ .5 [\sqrt{(\mu \cos \alpha_T)^4 + c_T^2} - (\mu \cos \alpha_T)^2] \}^{1/2} \quad (A35)$$

where μ is the advance ratio, c_T is the thrust coefficient and α_T is the angle of attack of the rotor tip path plane. The first estimate for blade circulations for the blade loads program are input from the wake program, and are those values associated with the last steps of the wake program calculations. The subroutine START computes the first estimates for various blade motion quantities which are used in the first blade loads estimates. The plunging velocity, \dot{h} , is a function of both radial and azimuthal coordinate, and is given by

$$\begin{aligned} \dot{h} = & \bar{r}(\kappa_1 \sin \psi - \eta_1 \cos \psi) \\ & - (b/2) [(A_c - \kappa_1) \cos \psi - (B_c + \eta_1) \sin \psi] \\ & - \mu \cos \psi (\kappa_0 + \kappa_1 \cos \psi + \eta \sin \psi) \quad , \end{aligned} \quad (A36)$$

the torsional deflection θ varies only azimuthally, and is given by

$$\theta = \theta_0 + A_c \sin \psi + B_c \cos \psi \quad , \quad (A37)$$

the slope, ξ , also varies only azimuthally, and is given by

$$\xi = \kappa_0 + \kappa_1 \cos \psi + \eta_1 \sin \psi \quad , \quad (A38)$$

and the time derivative of the generalized coordinates, assuming that only the primary flapping mode (say $\kappa=1$) responds, are given by

$$\dot{\zeta}_1(\psi) = (\Omega R/A_{V_N}^{(1)}) (\kappa_1 \sin \psi - \eta_1 \cos \psi)$$

and
$$\dot{\zeta}_k(\psi) = 0 \quad \text{for} \quad k > 1 . \quad (A39)$$

Here $A_{V_N}^{(1)}$ is the tip flap deflection of the normalized mode shape for the primary flapping mode. In the above equations, κ_0 , κ_1 , and η_1 , are given by

$$\eta_1 = \eta_2/\eta_3 ,$$

where

$$\eta_2 = (d_0-1)(a_2 d_0 - d_1 a_0) - (a_1 d_0 - c_1 a_0)(d_2/2 - c_0)$$

and

$$\eta_3 = (d_0-1)[d_0(d_0-1) - d_1^2/2] - (d_2/2 - c_0)[d_0(d_2/2 + c_0) - d_1 c_1/2] ;$$

$$\kappa_1 = (1/d_0-1)[a_1 - c_1 a_0/d_0 - (d_2/2 + c_0 - d_1 c_1/2 d_0)\eta_1]$$

and

$$\kappa_0 = (a_0 - d_1 \eta_1/2)/d_0 .$$

In these equations

$$c_0 = k_I/4$$

$$c_1 = \mu k_I/3$$

$$d_0 = \bar{\omega}_\beta^2 - b_1 k_I/3$$

$$d_1 = -\mu b_1 k_I/2$$

$$d_2 = \mu^2 k_I/4$$

$$a_0 = [\theta_0(1+\mu^2)/4 + \mu A_c/3 - \mu B_c b_1/4$$

$$- (\bar{\omega} + \mu \alpha_T)/3 + \beta_N(1/5 + \mu^2/6)] k_I$$

$$a_1 = [(1/4 + \mu^2/8)B_C + A_C b_1/3]k_I$$

$$a_2 = [2\mu\theta_0/3 + (1/4 + 3\mu^2/8)A_C - B_C b_1/3 \\ - \mu(\bar{\omega} + \mu\alpha_T) + \mu\beta_N/2]k_I$$

b_1 = blade semichord at radial station 1,

β_N = twist angle at tip,

$$k_I = 2\pi\rho bR^4/I_2 ,$$

$$\bar{\omega}_\beta^2 = 1 + \delta I_1/I_2$$

$$I_1 = \int_{\delta}^R m(r) (r-\delta) dr$$

$$I_2 = \int_{\delta}^R m(r) (r-\delta)^2 dr$$

$m(r)$ = radial mass distribution per unit span, and other symbols are as defined in the list of symbols. The k_I and $\bar{\omega}_\beta^2$ are inputs to the blade loads program.

REFERENCES

1. Piziali, R.; and DuWaldt, F.: A Method for Computing Rotary Wing Airload Distribution in Forward Flight. Cornell Aero. Lab. Report BB-1495-S-1, TCREC TR 62-44, Nov. 1962.
2. Miller, R.: On the Computation of Airloads Acting on Rotor Blades in Forward Flight. J. Am. Helicopter Soc., vol. 7, no. 2, Apr. 1962.
3. Rabbott, J.P.; Lizak, A.A.; and Paglino, V.M.: A Presentation of Measured and Calculated Full-Scale Rotor Blade Aerodynamic and Structural Loads. USAAVLABS Tech. Report 66-31, July 1966.
4. Balcerak, J.C.: A Method for Predicting the Aerodynamic Loads and Dynamic Response of the Rotor Blades of a Tandem-Rotor Helicopter. USAAVLABS Tech. Report 67-38, June 1967.
5. Scheiman, J.; and Ludi, L.H.: Qualitative Evaluation of Effect of Helicopter Rotor-Blade Tip Vortex on Blade Airloads. NASA TN D-1637, May 1963.
6. Segel, L.: Rotor Airloads, Blade Motion and Stress Caused by Transient Inputs of Shaft Torque as Related to Stoppable Rotor Operation. USAAVLABS Tech. Report 67-18, May 1967.
7. Cox, C.R.; Hamzeh, S.M.; et al.: A Study of the Origin and Means of Reducing Helicopter Noise. TCREC Tech. Report 62-73, Nov. 1962.
8. Trenka, A.R.: Development of a Method for Predicting the Performance and Stresses of VTOL-Type Propellers. USAAVLABS Tech. Report 66-26, June 1966.
9. Brady, W.G.; and Crimi, P.: Representation of Propeller Wakes by Systems of Finite Core Vortices. Cornell Aero. Lab. Report No. BB-1665-S-2, Feb. 1965.
10. Crimi, P.: Theoretical Prediction of the Flow in the Wake of a Helicopter Rotor. Cornell Aero. Lab. Report No. BB-1994-S-1, Sept. 1965.
11. Erickson, J.C.; and Ordway, D.E.: A Theory for Static Propeller Performance. Proceedings of the CAL/USAAVLABS Symposium on Aerodynamic Problems Associated with V/STOL Aircraft, vol. I, June 1966.
12. Rorke, J.B.; and Wells, C.D.: The Prescribed Wake-momentum Analysis. Proceedings of the Third CAL/AVLABS Symposium on Aerodynamics of Rotary Wing and V/STOL Aircraft, vol. I, June 1969.
13. Robinson, A.; and Laurman, J.A.: Wing Theory. Cambridge Univ. Press, London, 1956.
14. Sadler, S.G.: Rotating Blade Natural Frequency and Mode Shape Program. RASA Report No. 67-11, Nov. 1967.
15. Sadler, S.G.: Rotating Blade Natural Frequency and Mode Shape Program for Coupled and Uncoupled Modes. RASA Report No. 69-3, Mar. 1969.
16. Pestel, E.C., and Leckie, F.A.: Matrix Methods in Elastomechanics. McGraw-Hill Book Co., Inc., 1963.

17. Heyson, H.H., and Katzoff, S.: Induced Velocities Near a Lifting Rotor With Nonuniform Disc Loading. NACA Report 1319, 1957.
18. Ward, John F.; and Snyder, William J.: The Dynamic Response of a Flexible Rotor Blade to a Tip-vortex Induced Moving Force. AIAA/AHS VTOL Research, Design, and Operations Meeting. Paper no. 69-203, February 1969.
19. Crimi, P.: Theoretical Prediction of the Flow in the Wake of a Helicopter Rotor. Cornell Aero. Lab. Report No. BB-1994-S-2, Sept. 1965.
20. Tranter, C.J.: Integral Transforms. Wiley Interscience (New York), 1956.

TABLE 1.

ROTOR BLADE MODEL PROPERTIES, CONTINUOUS FORM

Blade property	Numerical value	Blade station range
mass distribution	6.2419 kilogram/meter	0.0762 meters to tip
torsional inertia distribution	0.02593 kilogram/ meter	0.0762 meters to tip
flatwise stiffness	1.9696×10^4 newton- meter ²	0.0762 meters to tip
chordwise stiffness	111.977×10^4 newton- meter ²	0.0762 meters to tip
torsional stiffness	3.9393×10^4 newton- meter ² 2.0816×10^4 newton- meter ²	0.0762 meters to 0.5334 meters 0.5334 meters to tip
location of pitch and elastic axes (coincident)	center line of shaft 0.085725 meters from airfoil leading edge	0.0762 meters to 0.5334 meters 0.5334 meters to tip
location of center of gravity forward of blade twist	0.0 meters 0.006858 meters	0.0762 meters to 0.5334 meters 0.5334 meters to tip
blade twist	none	0.0762 meters to tip

TABLE 2.
FREE VIBRATION DATA FOR MODEL BLADE NUMBER 1 (STANDARD BLADE)

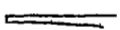
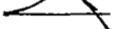
Natural frequency ω/Ω , for $\Omega=5.9167\text{HZ}$	Tip deflection, per unit flap deflection		Mode type, as indicated by sketches			Mode type name
	w/v m/m	ϕ/v rad/m	Flap, v m	Edgewise, w m	Torsion, ϕ rad	
1.045	0.158	-.0898				1st flapwise bending
1.511	-7.61	-.1076				1st edgewise bending
2.776	-.0009	0.390				2nd flapwise bending
5.230	0.0004	0.348				3rd flapwise bending
3.525	-.0129	331.				1st (control) torsion
9.062	-672.	0.0295				2nd edgewise bending

TABLE 3.

FREE VIBRATION DATA FOR MODEL BLADE NUMBER 2

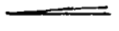
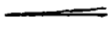
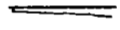
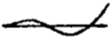
Natural frequency ω/Ω , for $\Omega=5.9167\text{HZ}$	Tip deflection, per unit flap deflection		Mode type, as indicated by sketches			Mode type name
	w/v m/m	ϕ/v rad/m	Flap, v m	Edgewise, w m	Torsion, ϕ rad	
1.081	0.0611	-.0745				1st flapwise bending
2.041	-19.9	-.115				1st edgewise bending
3.006	-.0018	0.404				2nd flapwise bending
6.230	0.0002	0.334				3rd flapwise bending
3.862	0.0086	231.				1st (control) torsion
12.354	-922.	-.0420				2nd edgewise bending

TABLE 4.
FREE VIBRATION DATA FOR MODEL BLADE NUMBER 3

Natural frequency ω/Ω , for $\Omega=5.9167\text{HZ}$	Tip deflection, per unit flap deflection		Mode type, as indicated by sketches			Mode type name
	w/v m/m	ϕ/v rad/m	Flap, v m	Edgewise, w m	Torsion, ϕ rad	
1.137	0.0237	-.0616				1st flapwise bending
2.977	-55.1	-.195				1st edgewise bending
3.451	-.0029	0.525				2nd flapwise bending
7.773	0.0001	0.361				3rd flapwise bending
4.304	-.007	153.				1st (control) torsion
17.844	-1890.	-.0472				2nd edgewise bending

TABLE 5.

FREE VIBRATION DATA FOR MODEL BLADE NUMBER 4

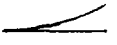
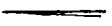
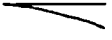
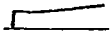
Natural frequency ω/Ω , for $\Omega=5.9167\text{HZ}$	Tip deflection, per unit flap deflection		Mode type, as indicated by sketches			Mode type name
	w/v m/m	ϕ/v rad/m	Flap, v m	Edgewise, w m	Torsion, ϕ rad	
1.071	-.168	-.0765				1st flapwise bending
0.3646	-5.61	-.0708				1st edgewise bending
2.777	0.0303	0.1004				2nd flapwise bending
5.225	0.0035	-.214				3rd flapwise bending
3.613	-.0222	76.1				1st (control) torsion
3.324	-12.6	0.420				2nd edgewise bending

TABLE 6.
PARAMETERS FOR VARIOUS FLIGHT CASES

Case No.	Blade model (no.)	Advance ratio $V/\Omega R$	Chord m	Separation		Shaft angle deg.	Collective angle deg.	Cyclic angles		Radius ratio R_2/R_1
				$\frac{\Delta z}{c}$	$\Delta\psi$ deg.			lat. deg.	long. deg.	
1	H-34	.2	0.417	0	90	-1.91	15.79	-6.9	3.05	1.0
2	1	.2	0.343	0	90	-2.22	5.25	-2.43	0	1.0
3	1	.2	0.343	1	90	-2.22	5.25	-2.43	0	1.0
4	1	.2	0.343	1	30	-2.22	5.25	-2.43	0	1.0
5	1	.2	0.343	1	20	-2.22	5.25	-2.43	0	1.0
6	1	.2	0.343	1	10	-2.22	5.25	-2.43	0	1.0
7	1	.3	0.343	1	30	-4.88	7.7	-4.06	1.0	1.0
8	1	.1	0.343	1	30	-.556	5.04	-1.14	0	1.0
9	4,3	.2	0.514	0	90	-2.33	5.0	-2.27	0	0.7
10	1,2a	.2	0.374	1	30	-2.22	5.44	-2.60	0	0.85
11	1,2b	.2	0.343	1	30	-2.22	5.25,12.5	-2.43, -6.53	0	0.85
12	1	.2	0.343	0	90	-2.22	5.25	-2.43	0	1.0

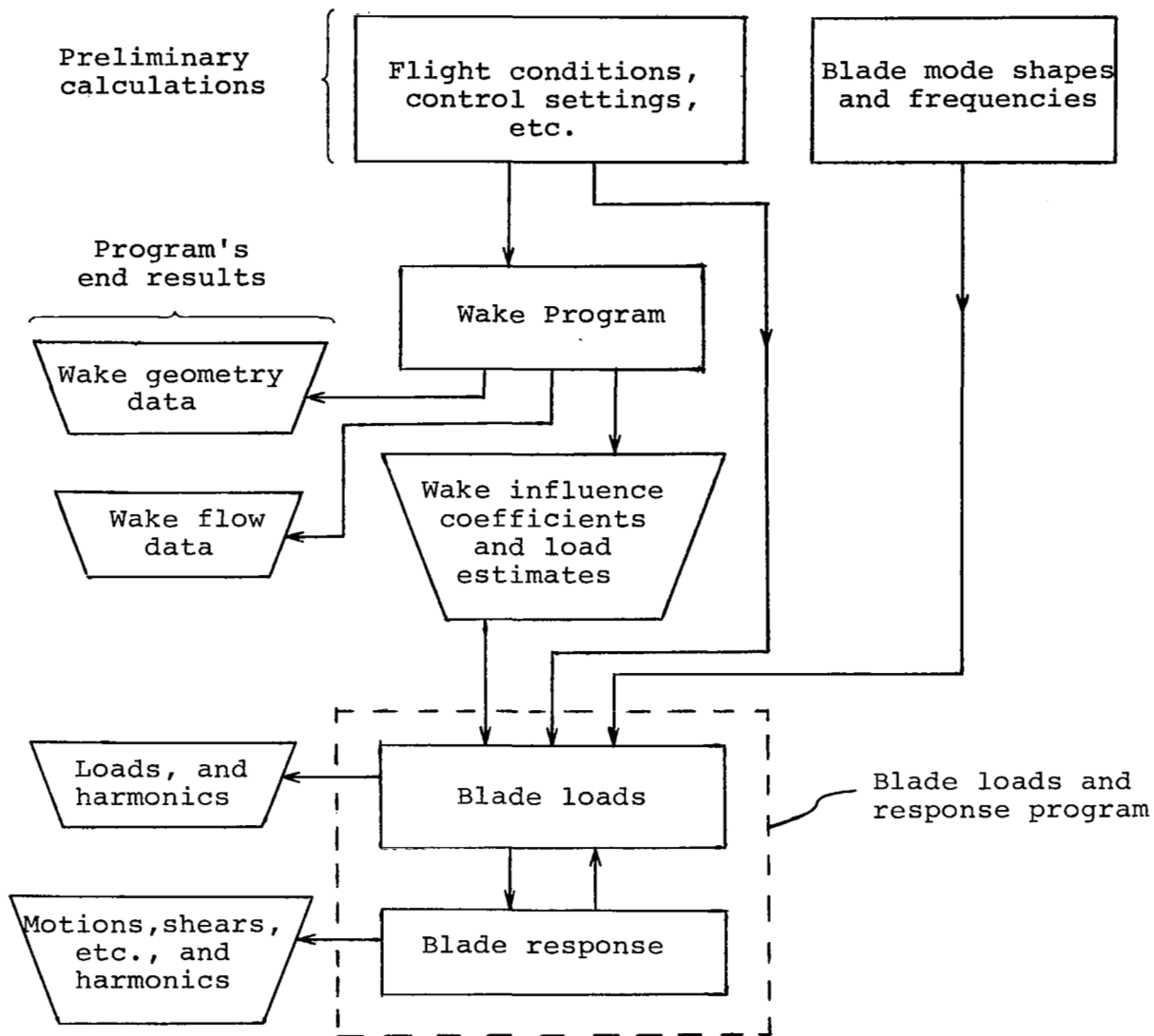


Figure 1. Flow diagram of program usage

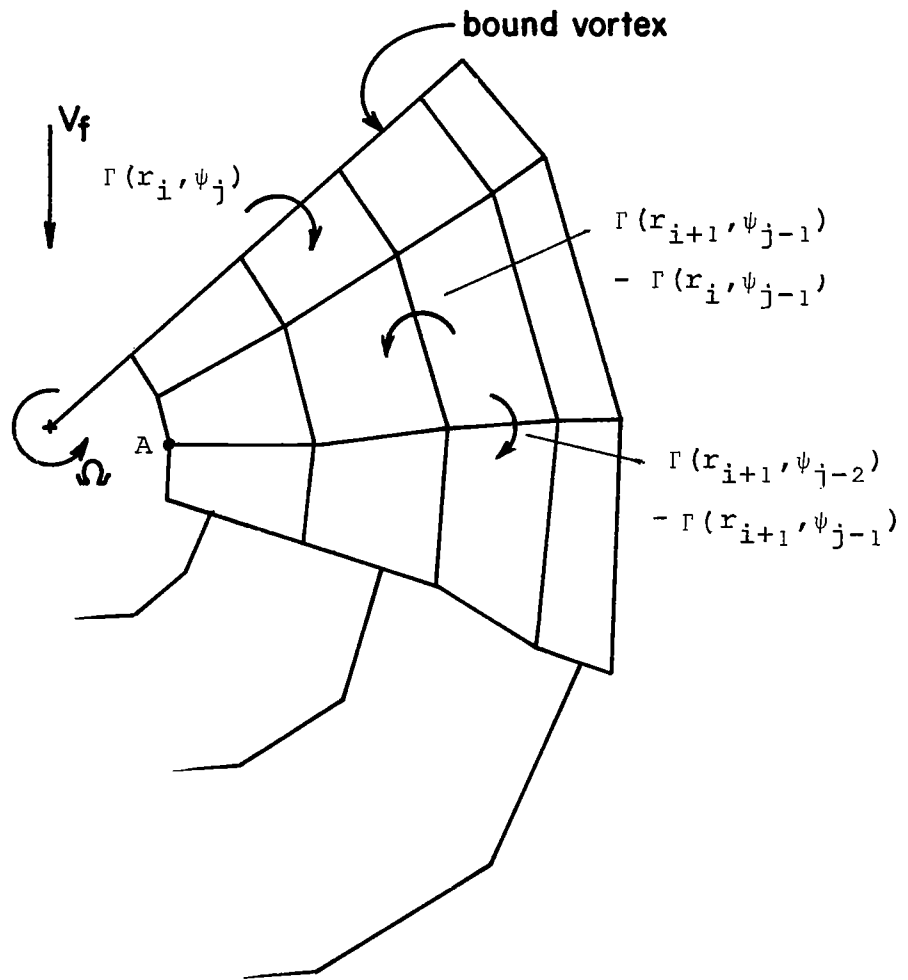
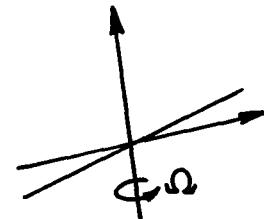
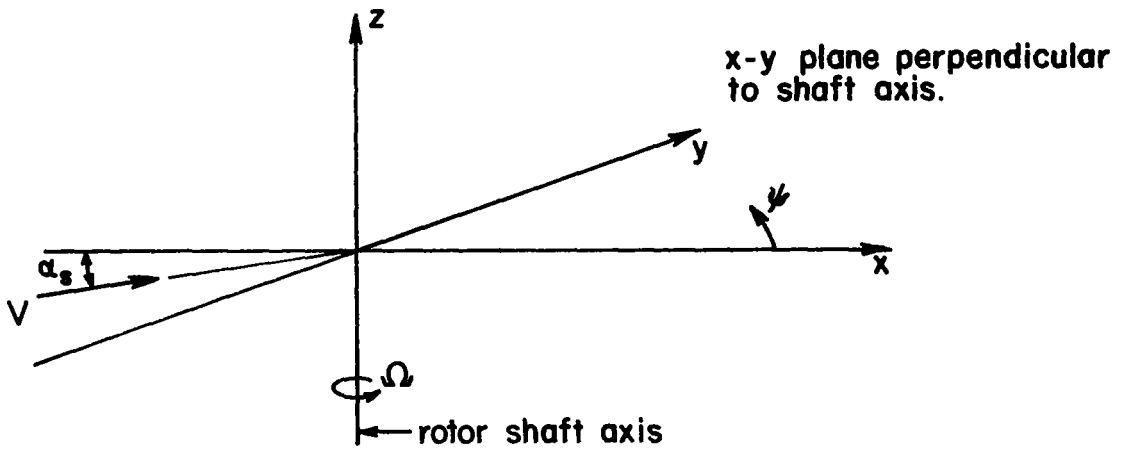


Figure 2. Wake model with combination of "full mesh" wake and "modified" wake of trailing vortices only

First rotor is located at coordinate system origin.



Second rotor location and rotation direction is determined by input.

Figure 3. Wake geometry and blade loads coordinate system

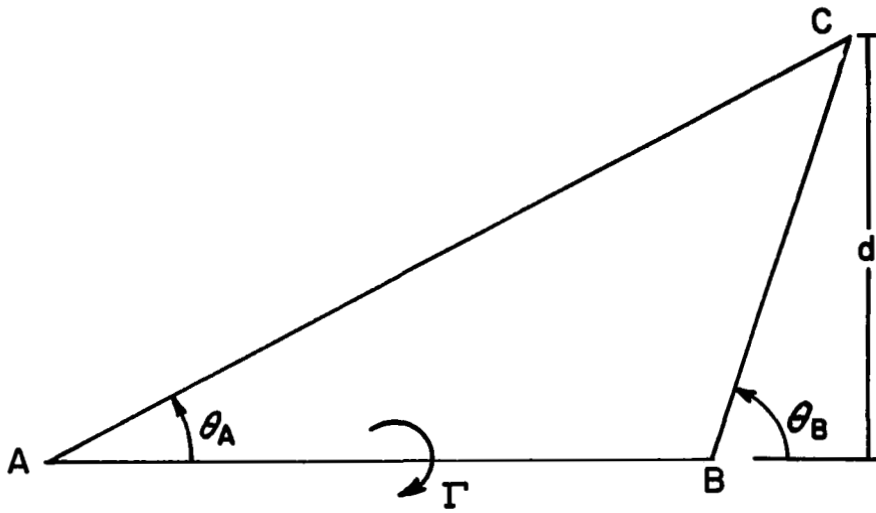


Figure 4. Vortex induced flow model

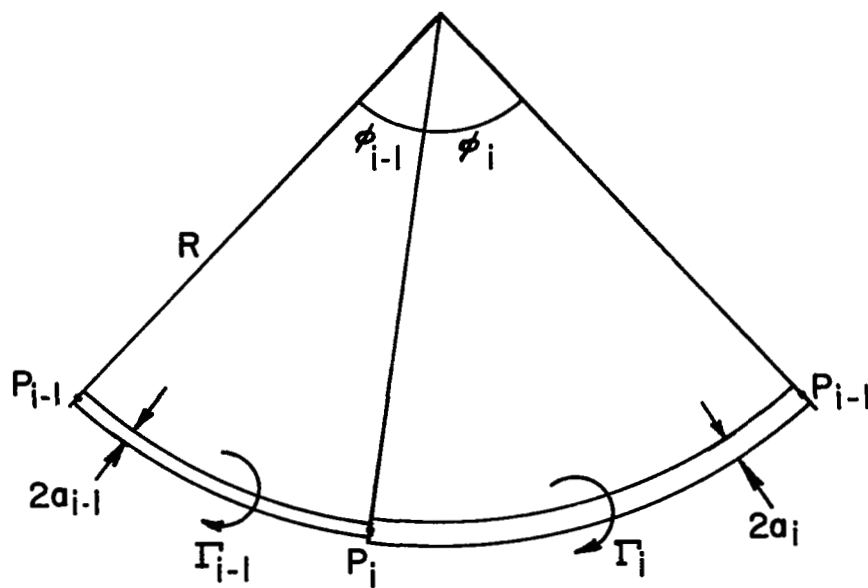


Figure 5. Vortex self-induced flow model

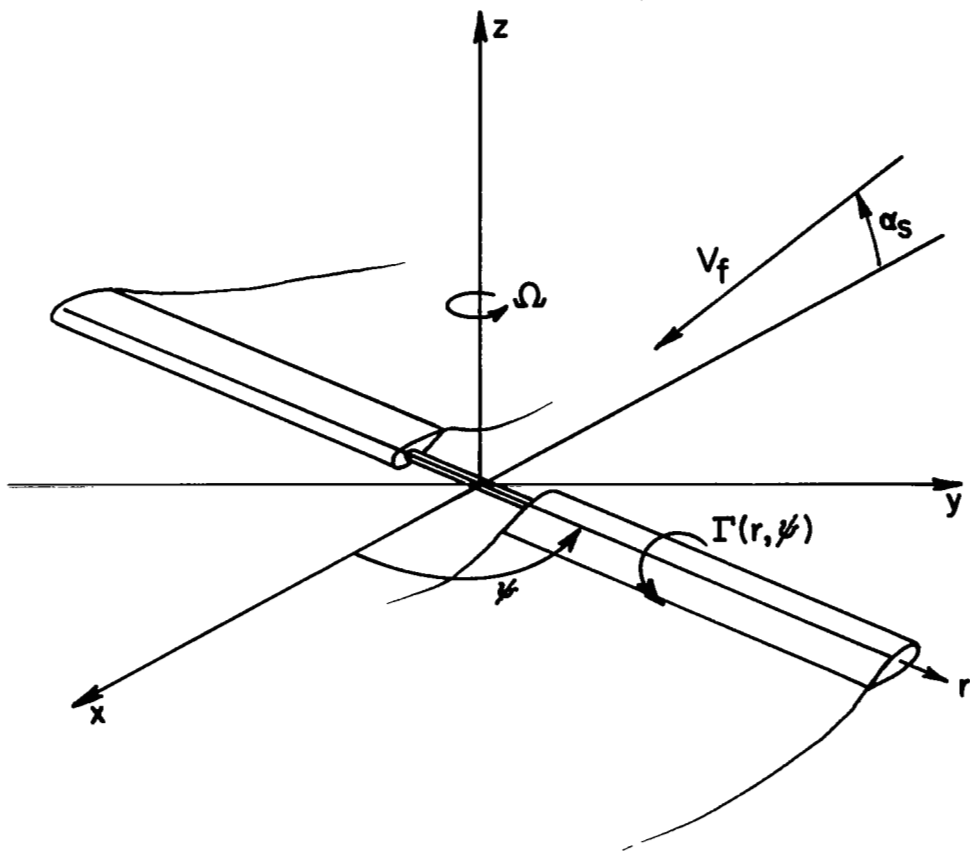


Figure 6. Blade aerodynamic coordinates

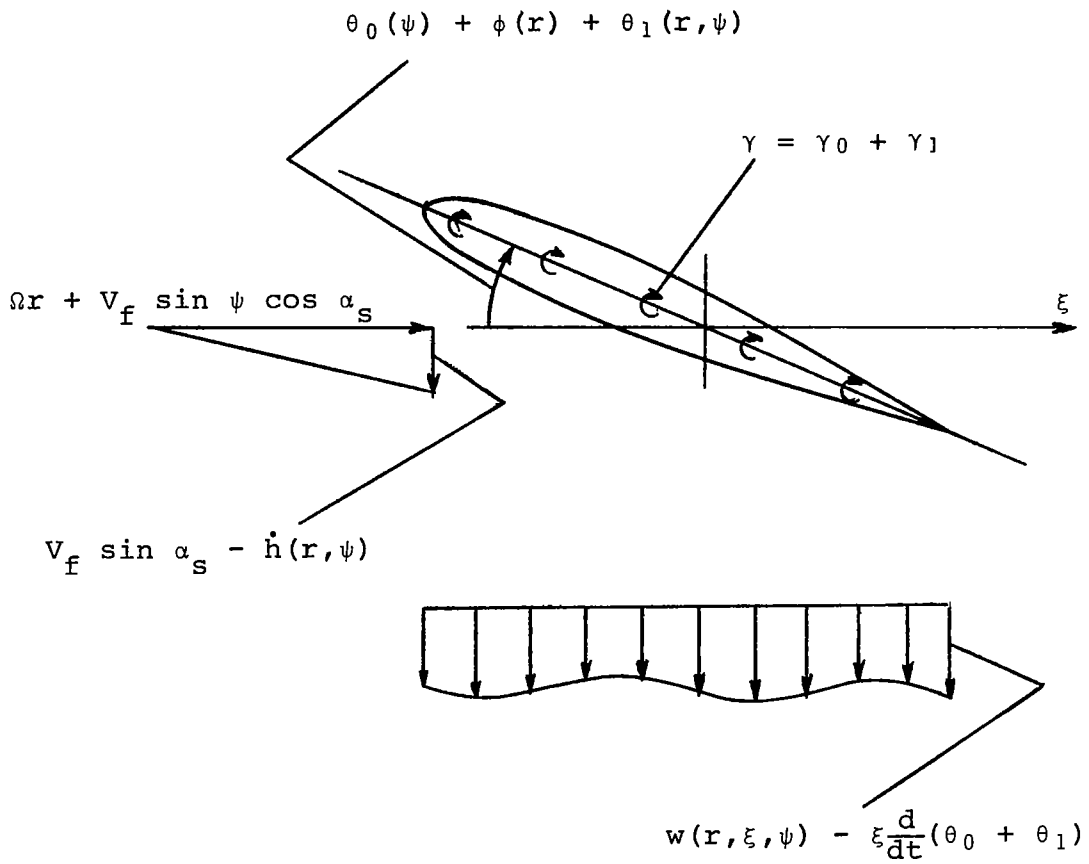
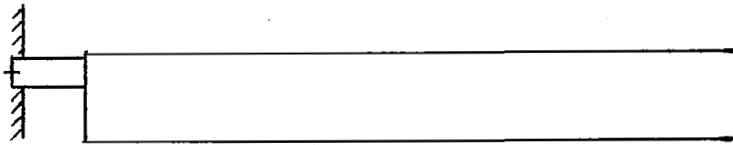
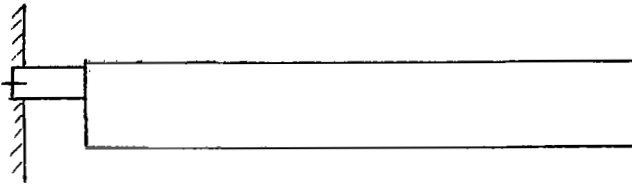


Figure 7. The flow at a blade section



Chord = 1.125 ft

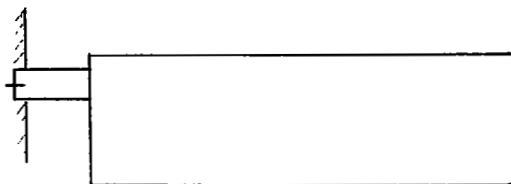
Blade 1, standard blade, $R = 210''$, $r_0 = 21''$



2a) Chord = 1.125 ft

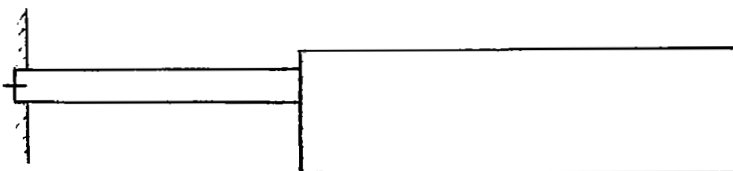
2b) Chord = 1.227 ft

Blade 2, tip radius = 0.85 standard tip radius, $r_0 = 21''$



Chord = 1.687 in.

Blade 3, tip radius = 0.70 standard tip radius, $r_0 = 21''$



Chord = 1.687 in.

Blade 4, airfoil root cutout to 0.40 tip radius, $R = 210''$,
 $r_0 = 84''$

Figure 8. Sketches of the four model blade configurations

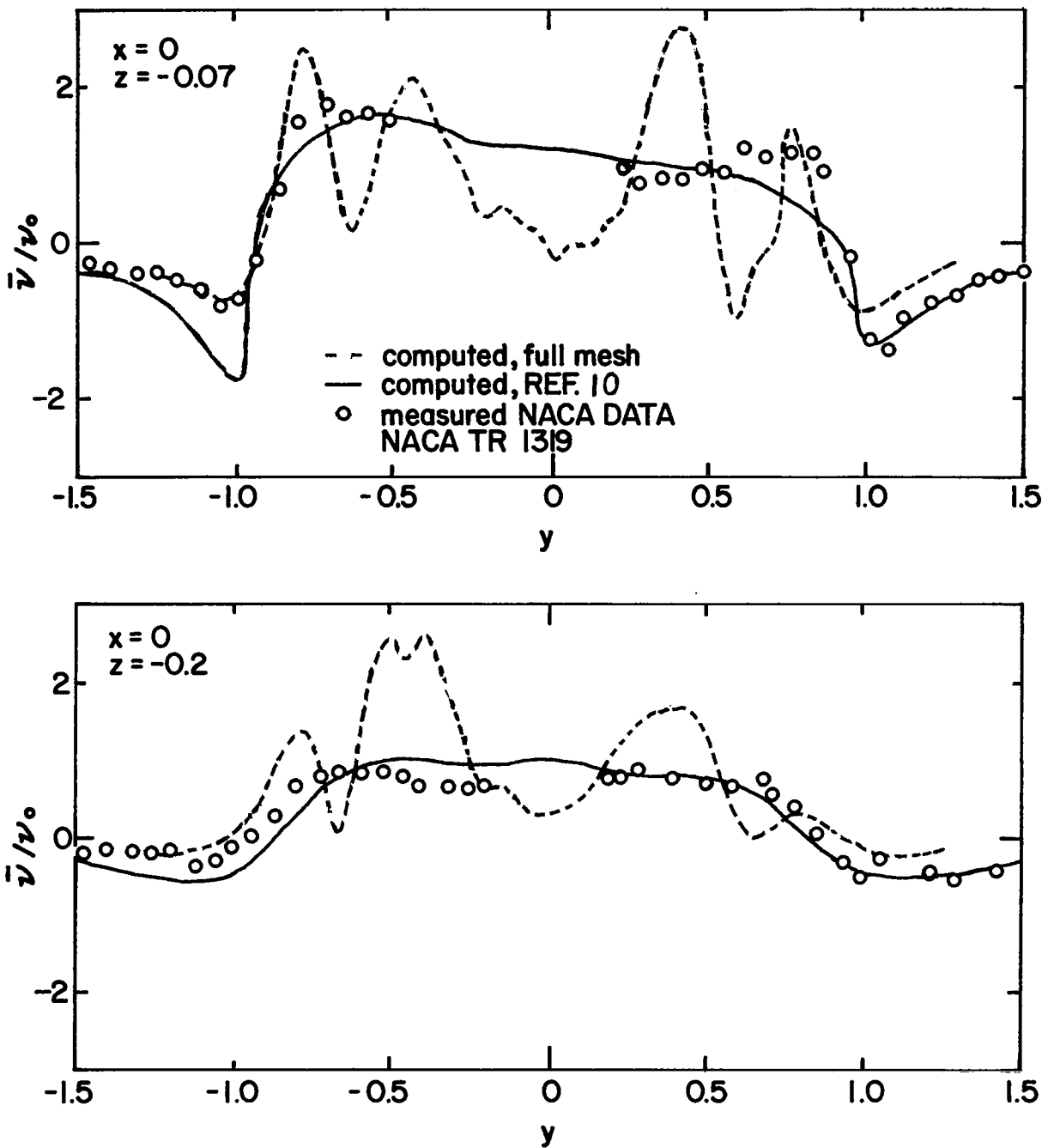


Figure 9. Comparison of computed and measured induced downwash below the rotor plane, $\mu=0.14$, $C_T=0.00371$, $x=0$

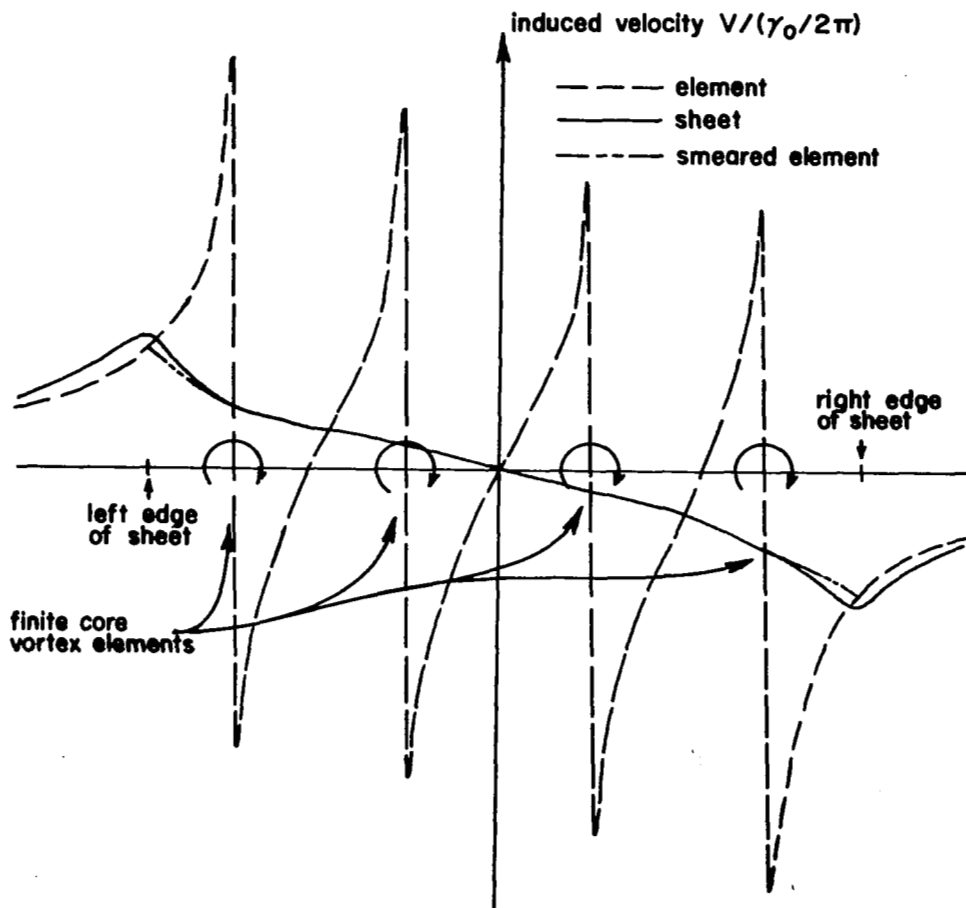


Figure 10. Induced velocity one fortieth of sheet width above sheet, using sheet, smeared core, and small core vortex elements.

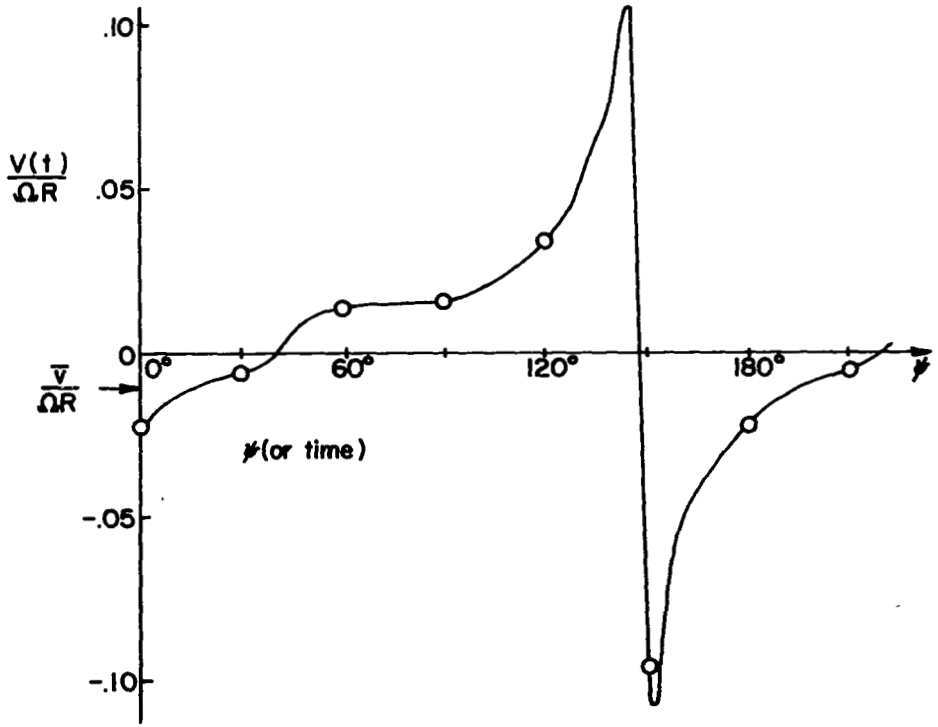


Figure 11. Unlimited $v(t)$

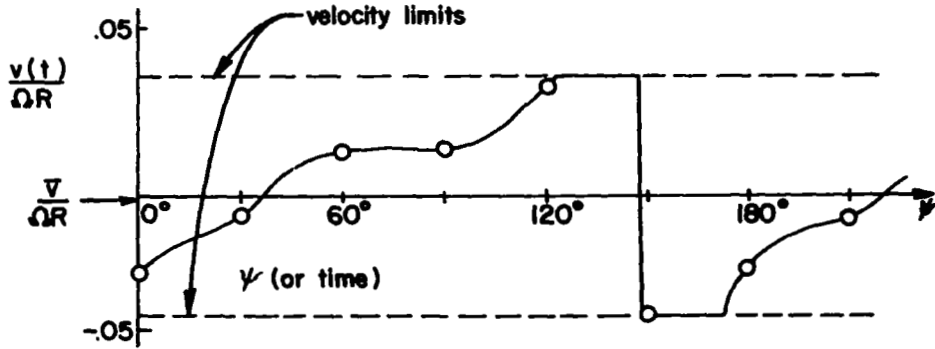


Figure 12. Limited $v(t)$

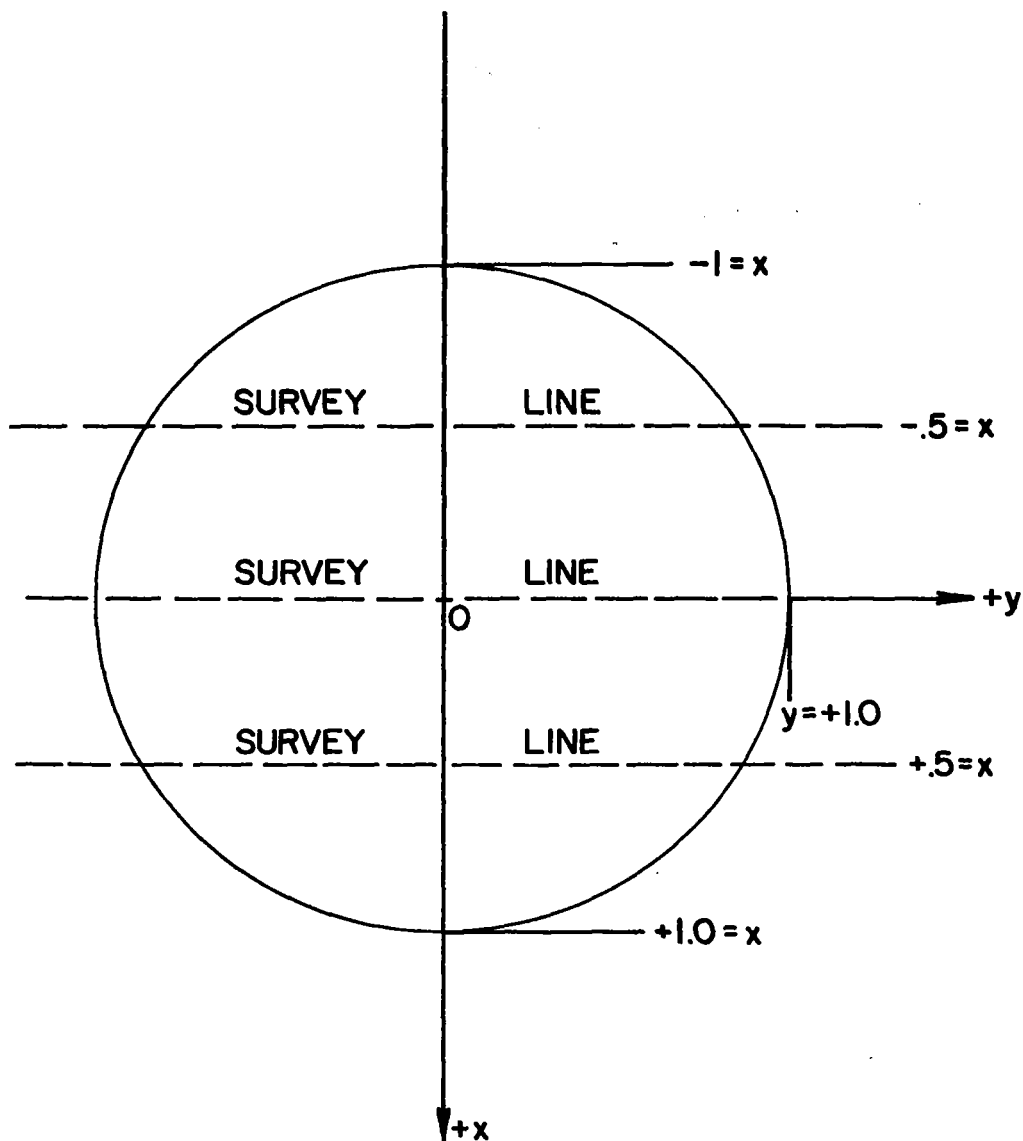


Figure 13. Wake survey positions, as seen from plan view, in rotor tip path plane coordinate system

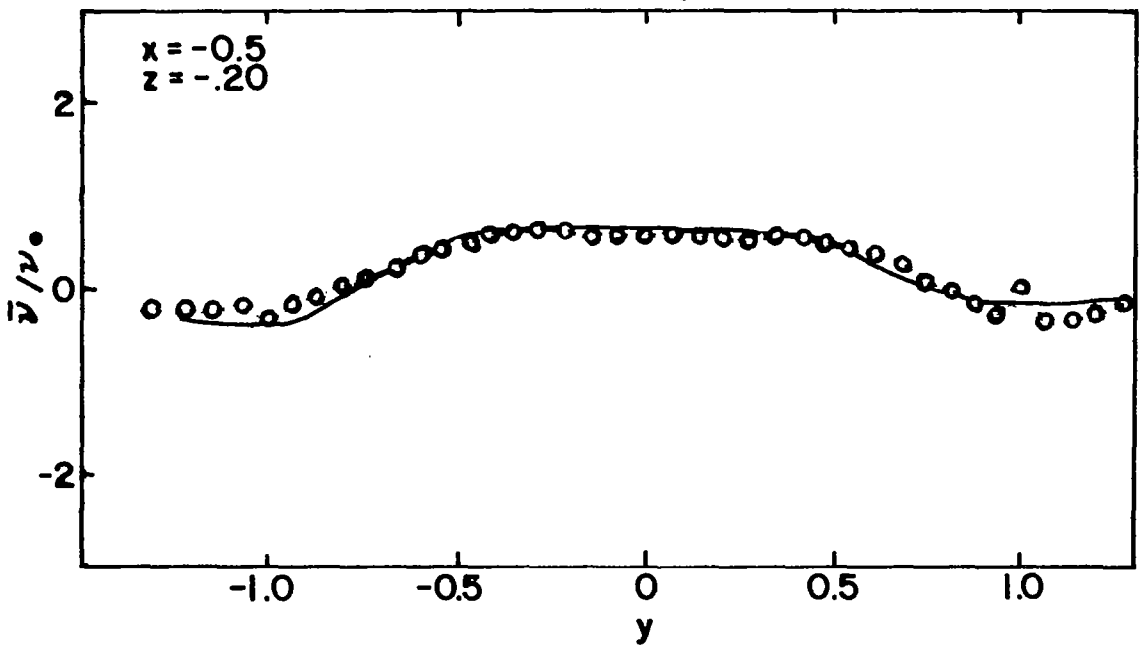
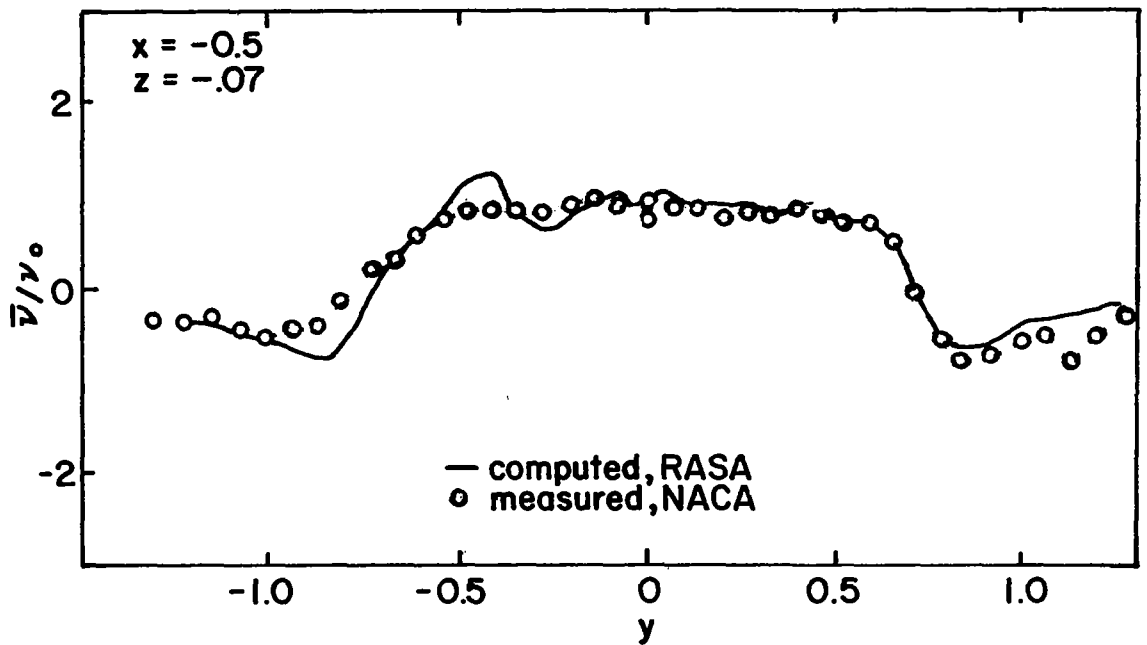


Figure 14. Comparison of computed and measured induced downwash below the rotor plane, $\mu=0.095$, $C_T=0.0032$, $x=-0.5$

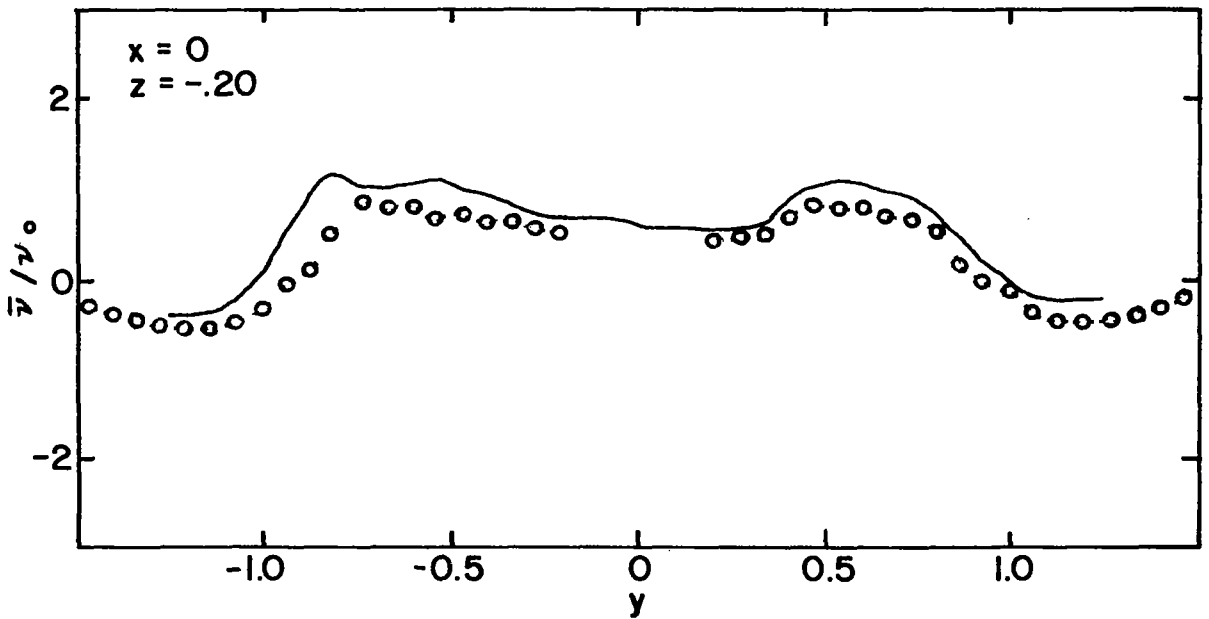
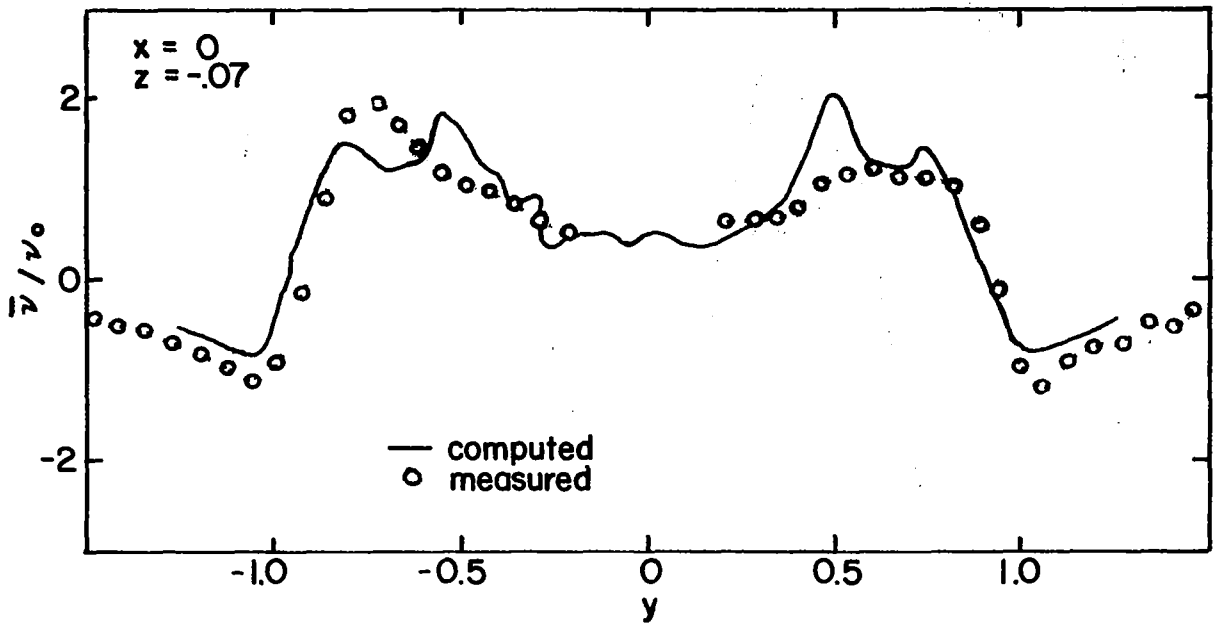


Figure 15. Comparison of computed and measured induced downwash below the rotor plane, $\mu=0.095$, $C_T=0.0032$, $x=0$

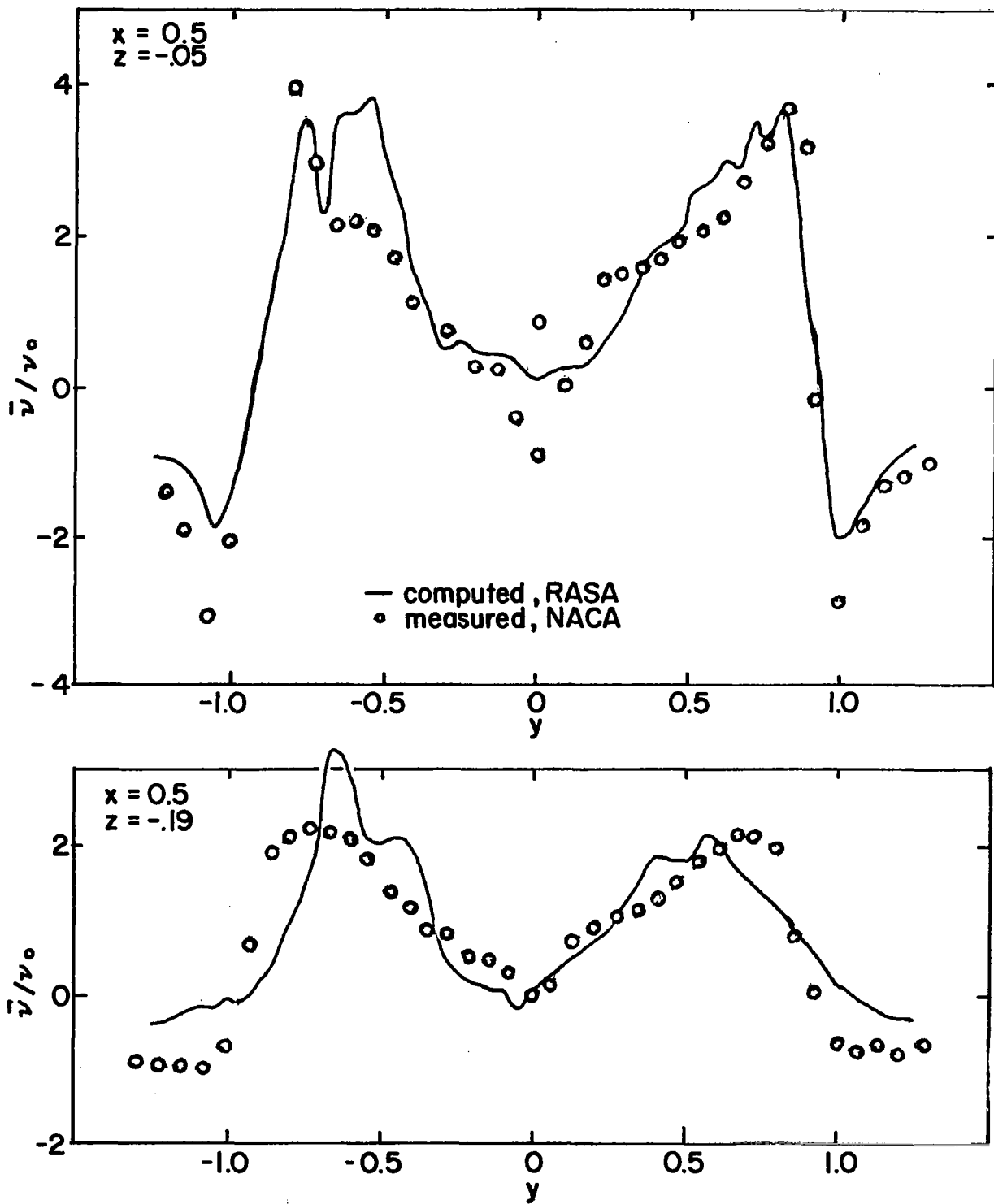


Figure 16. Comparison of computed and measured induced downwash below the rotor plane, $\mu=0.095$, $C_T=0.0032$, $x=0.5$

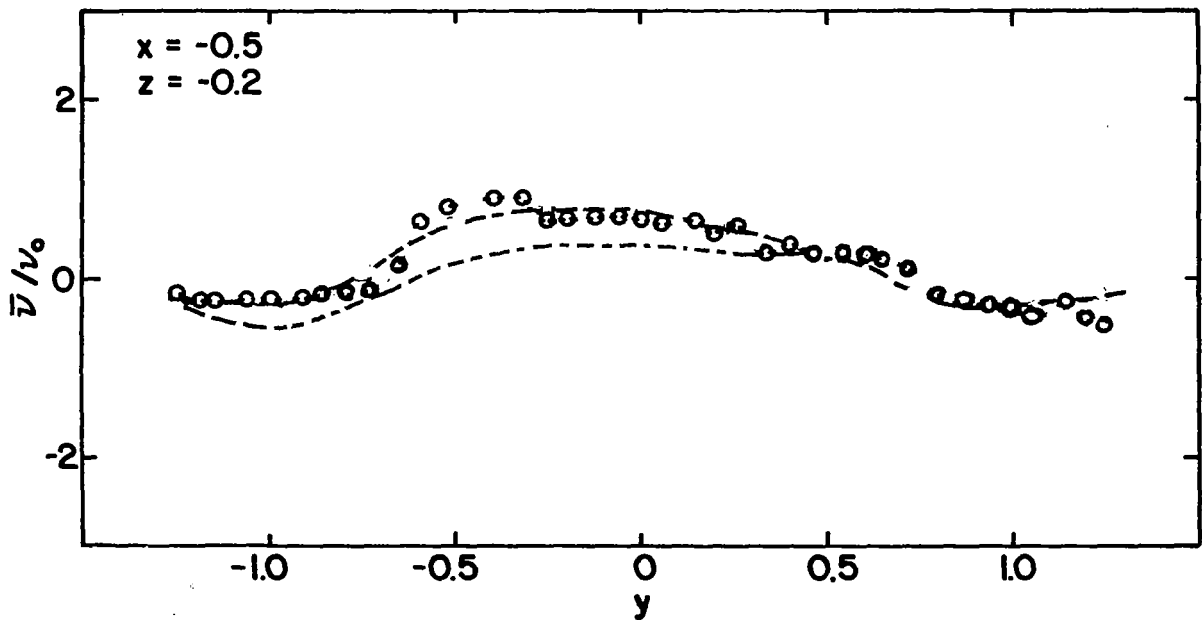
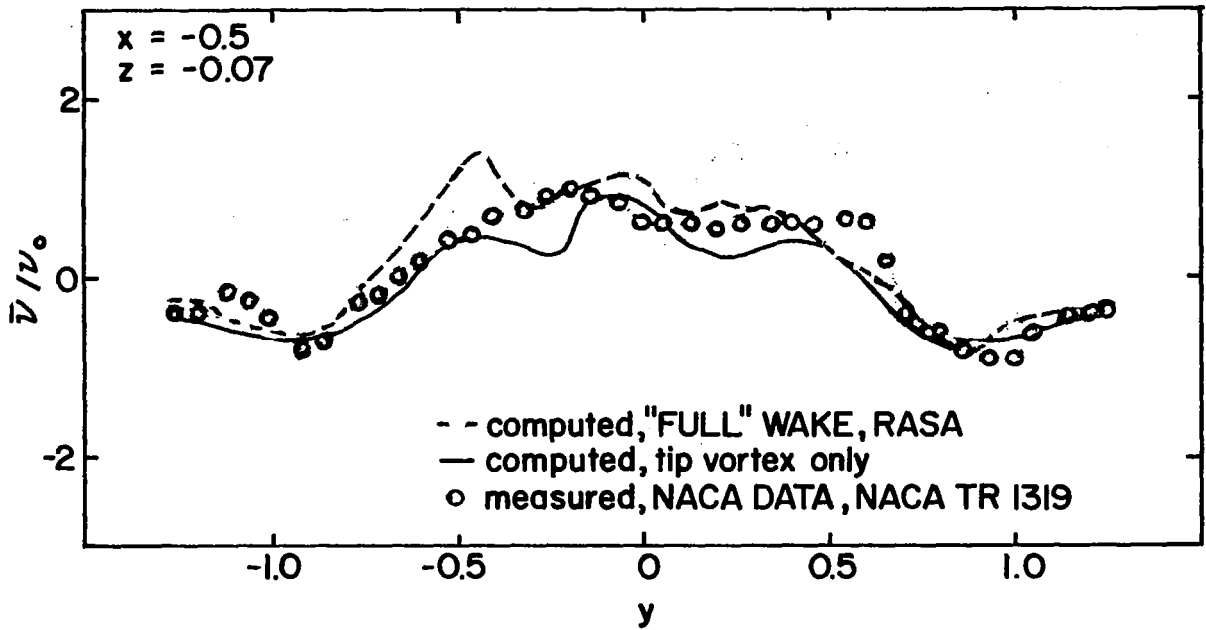


Figure 17. Comparison of computed and measured induced downwash below the rotor plane, $\mu=0.14$, $C_T=0.00371$, $x=-0.5$

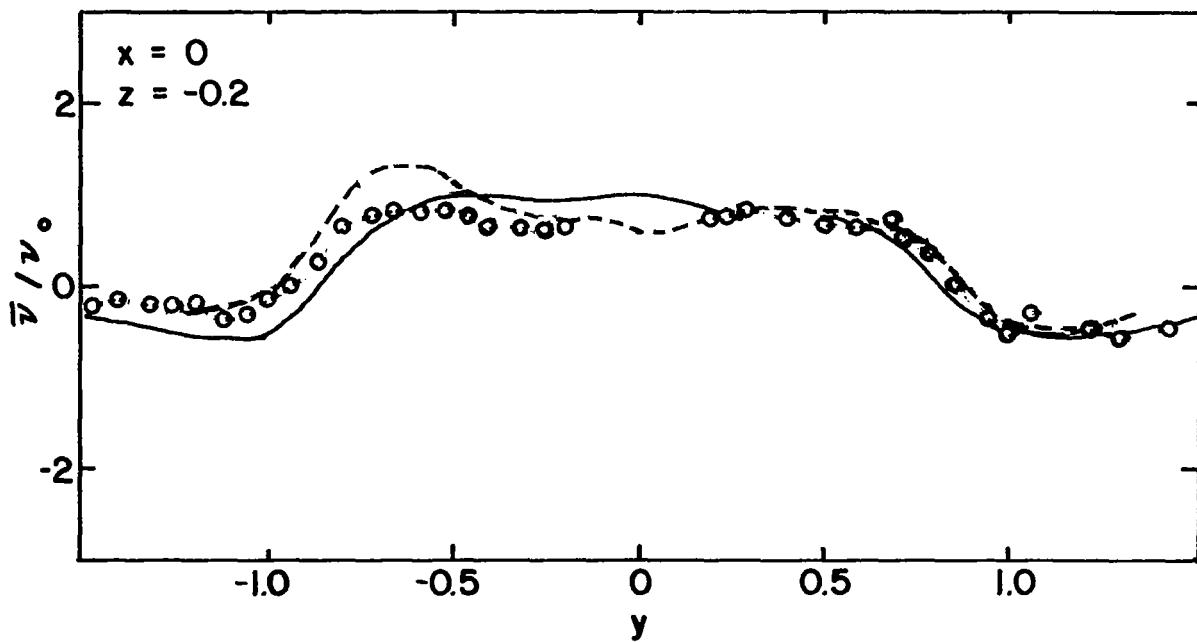
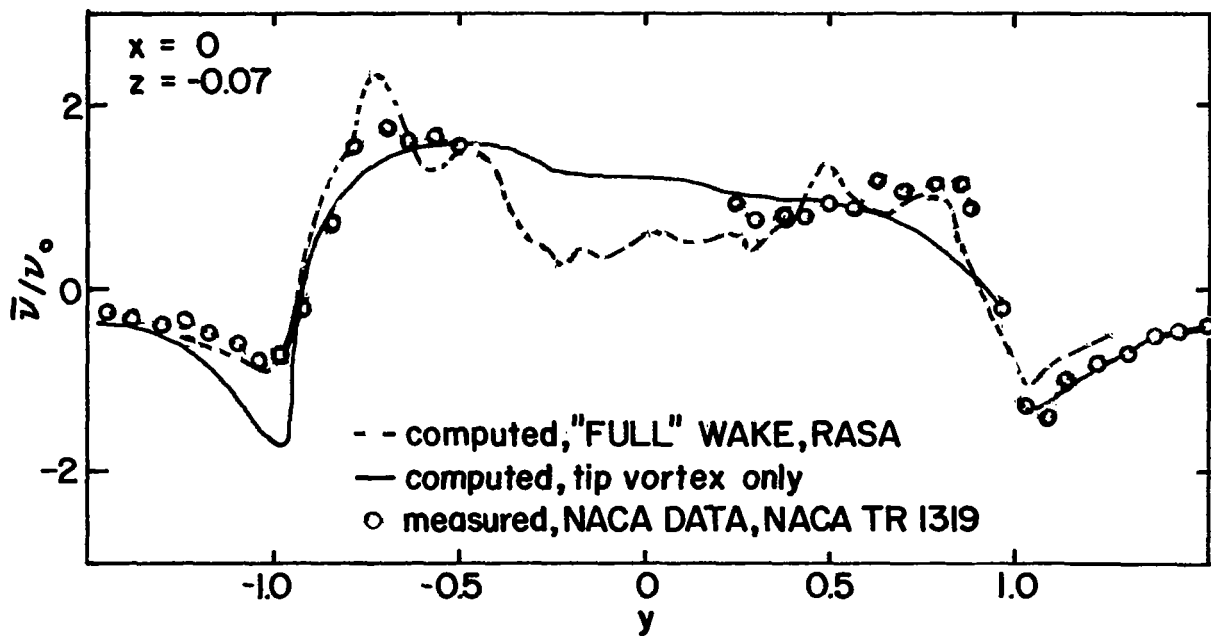


Figure 18. Comparison of computed and measured induced downwash below the rotor plane, $\mu=0.14$, $C_T=0.00371$, $x=0$

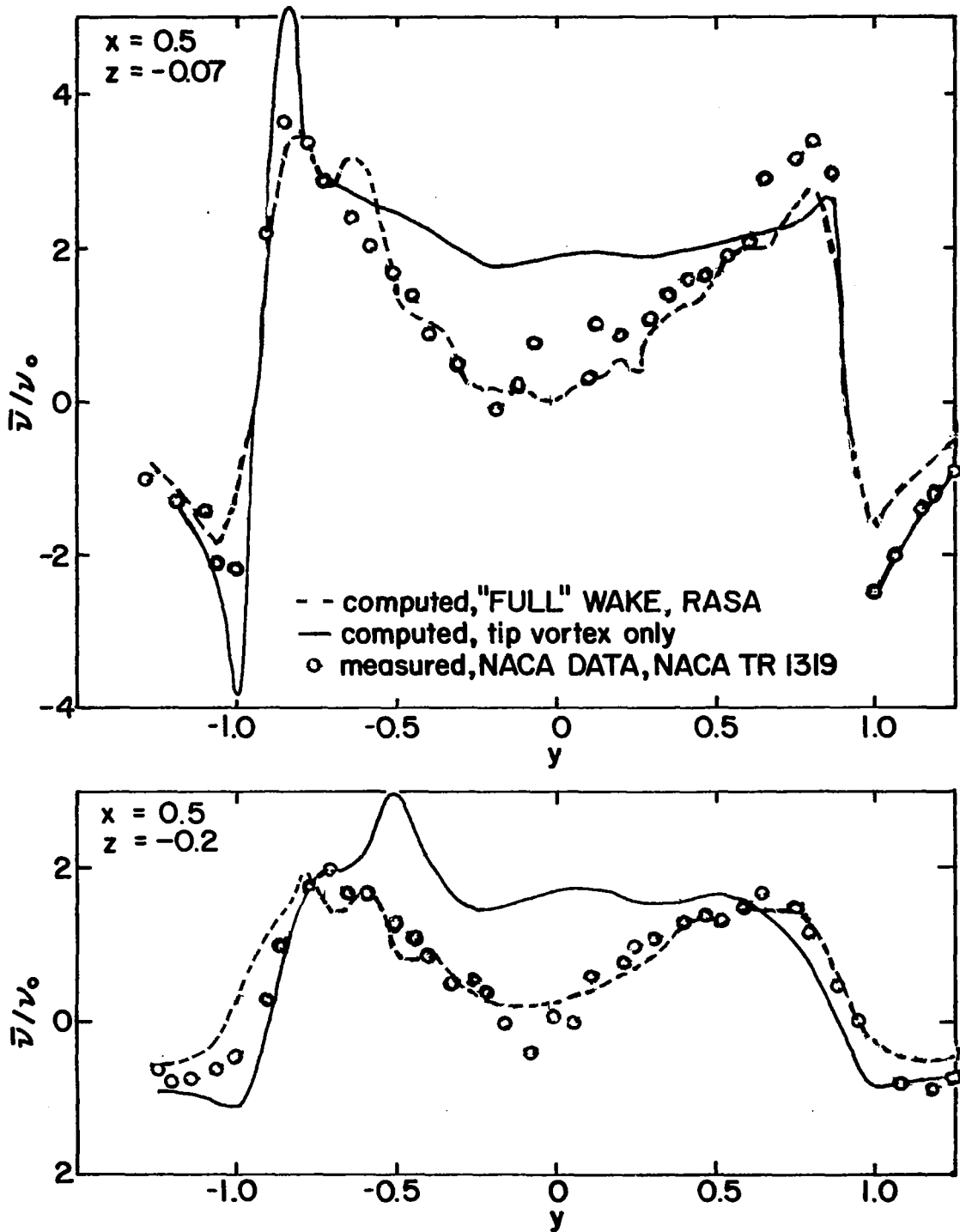


Figure 19. Comparison of computed and measured induced downwash below the rotor plane, $\mu=0.14$, $C_T=0.00371$, $x=0.5$

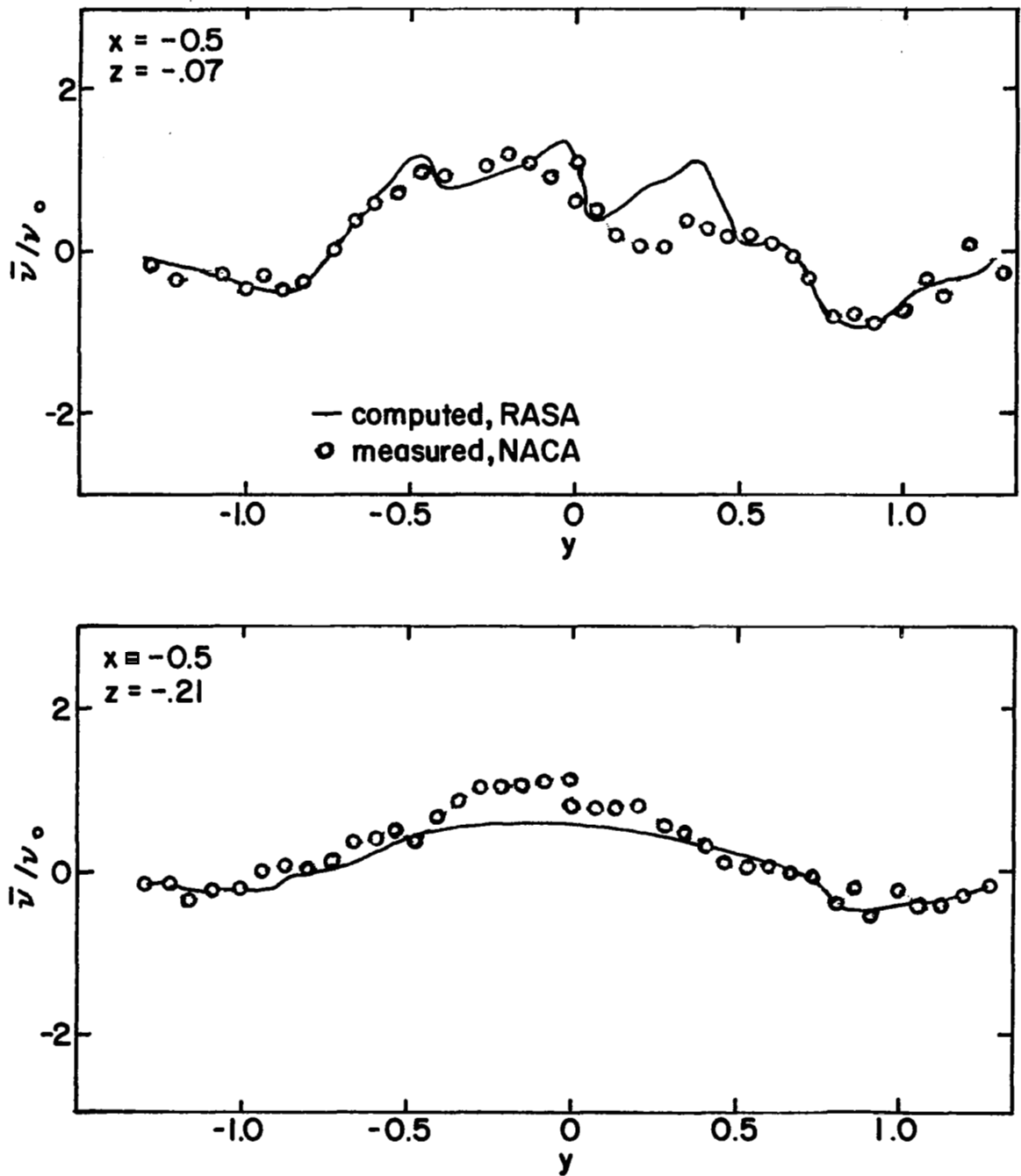


Figure 20. Comparison of computed and measured induced downwash below the rotor plane, $\mu=0.232$, $C_T=0.00321$, $x=-0.5$

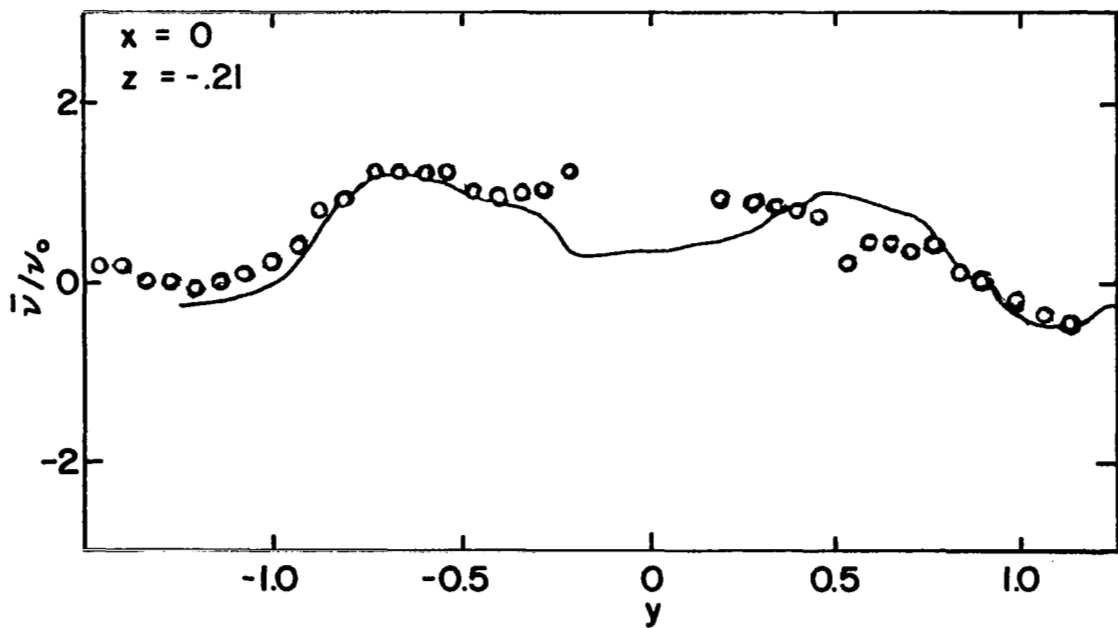
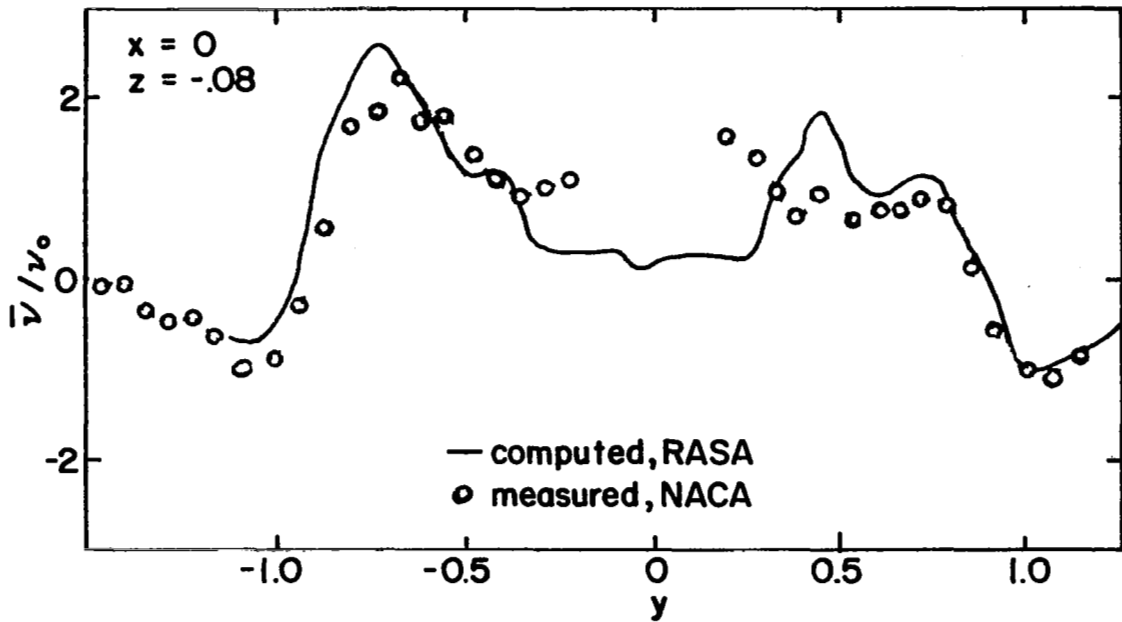


Figure 21. Comparison of computed and measured induced downwash below the rotor plane, $\mu=0.232$, $C_T=0.00321$, $x=0$

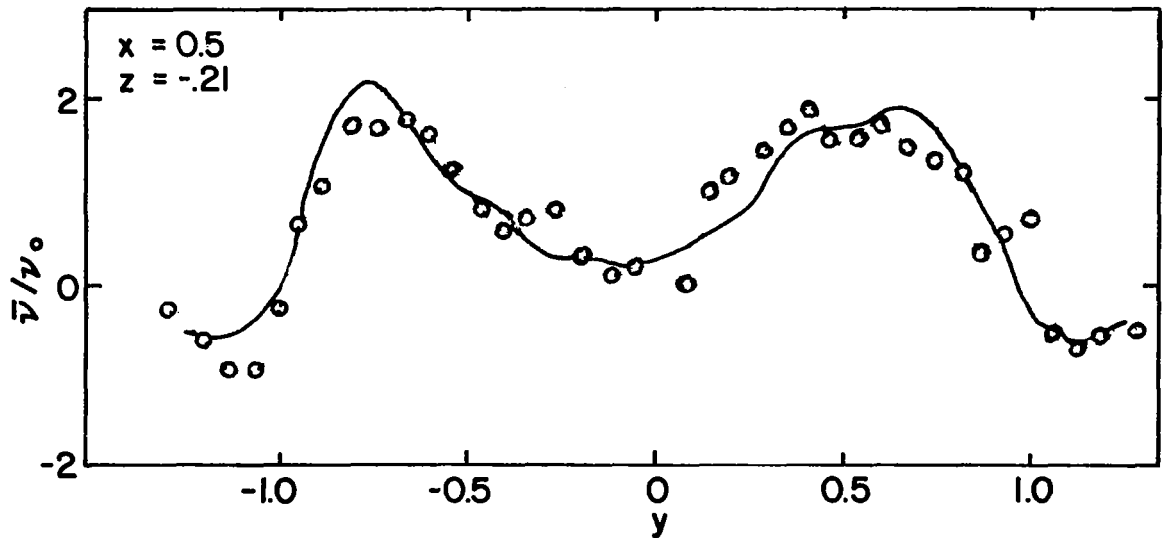
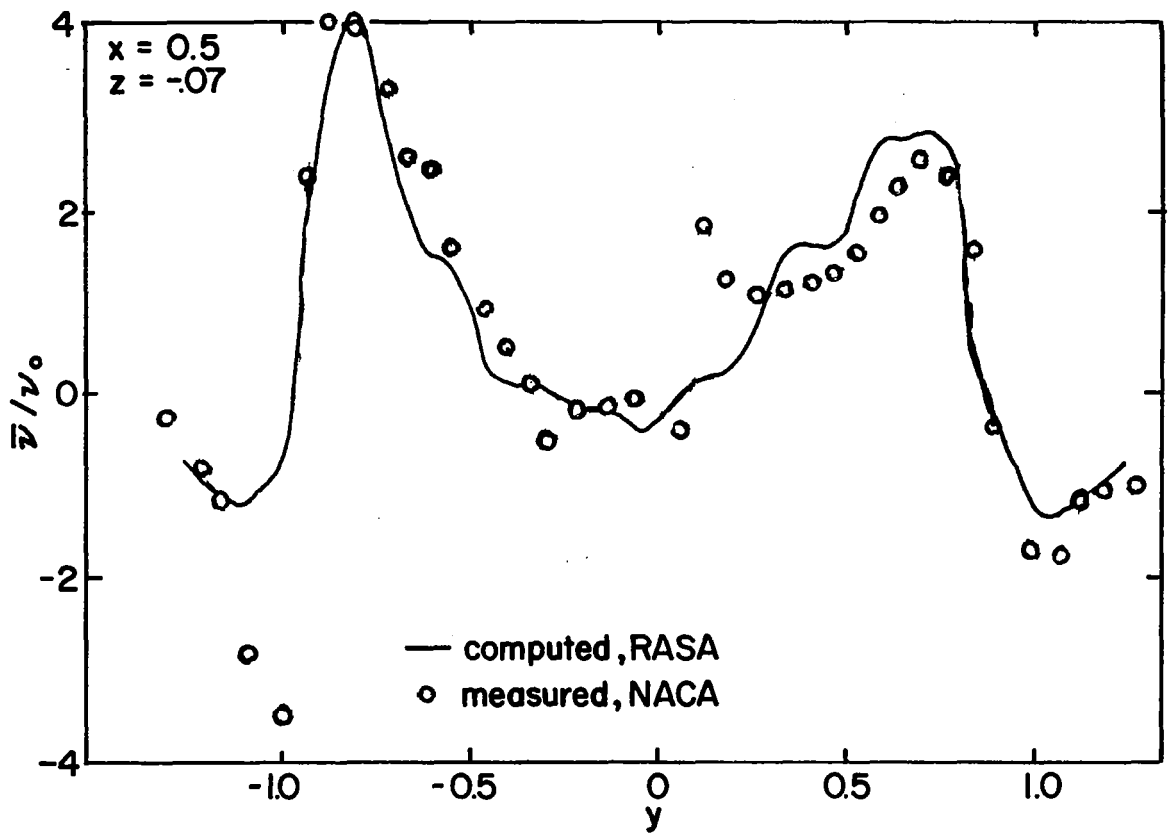


Figure 22. Comparison of computed and measured induced downwash below the rotor plane, $\mu=0.232$, $C_T=0.00321$, $x=0.5$

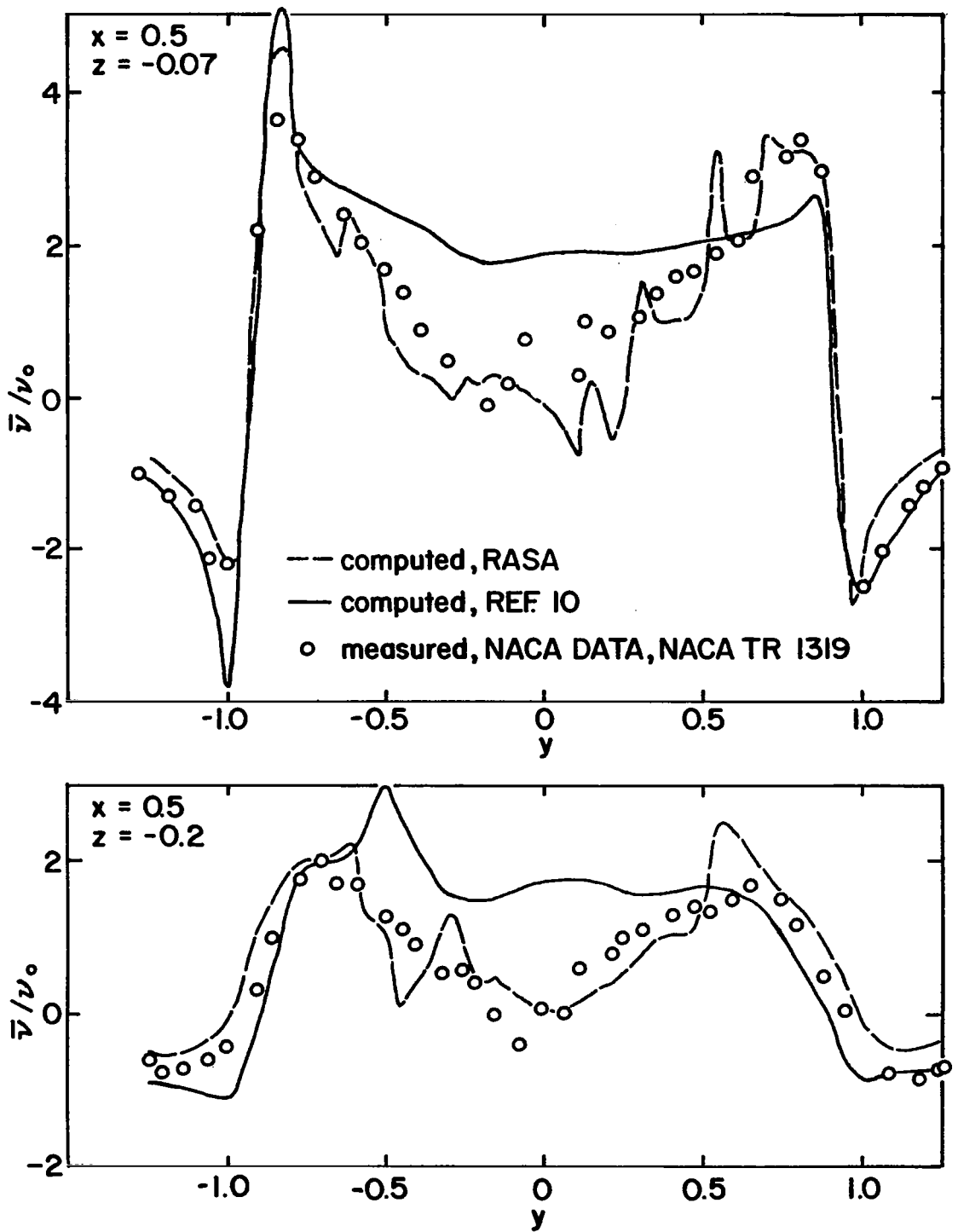
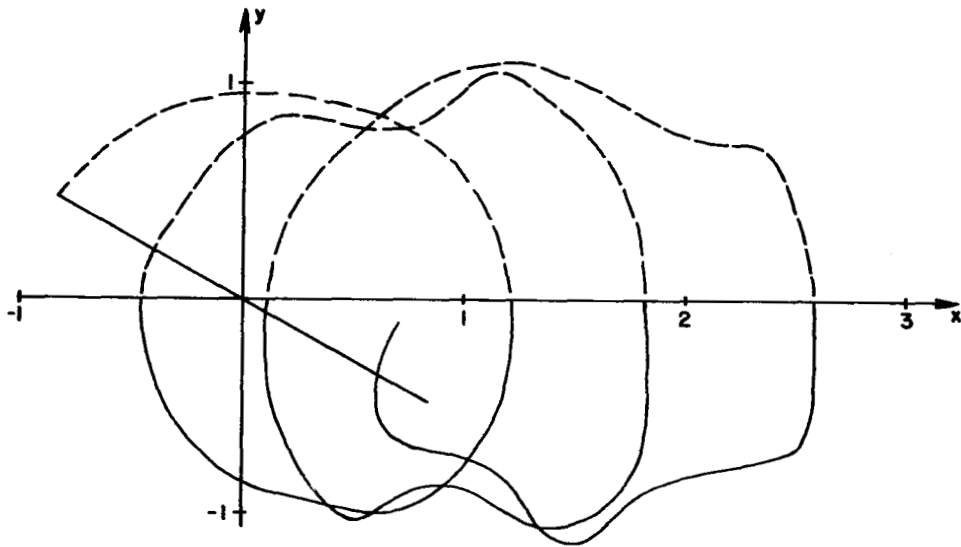
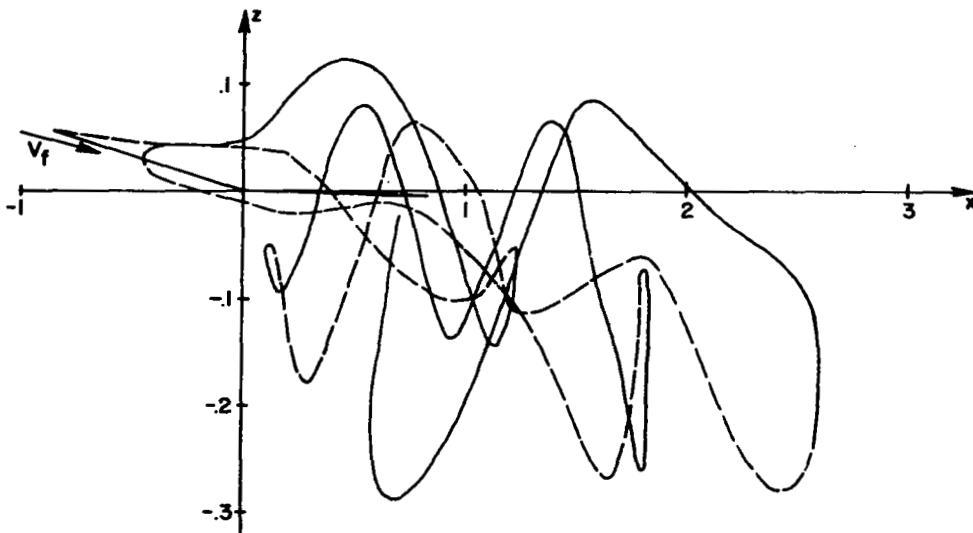


Figure 23. Comparison of computed and measured induced downwash below the rotor plane, $\mu=0.14$, $C_T=0.00371$, $x=0.5$

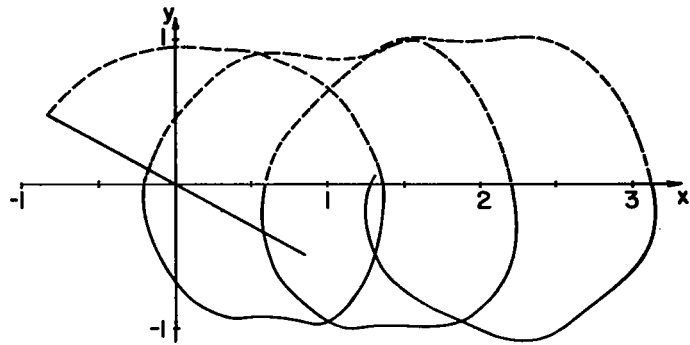


(a) plan view

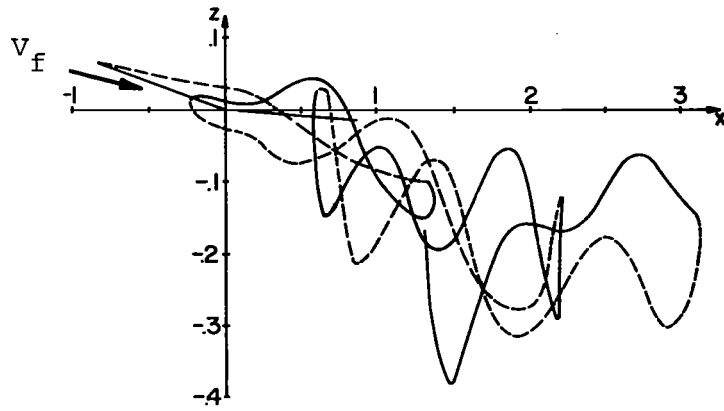


(b) side view

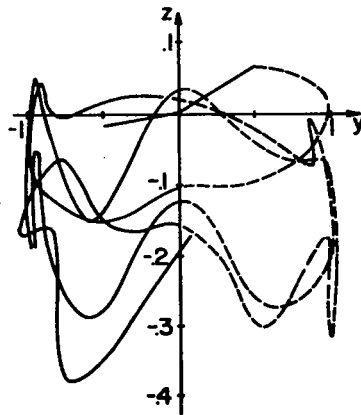
Figure 24. Single two-bladed rotor's tip vortex location, $\mu=0.097$, $\alpha_s=-3.1^\circ$



(a) plan view

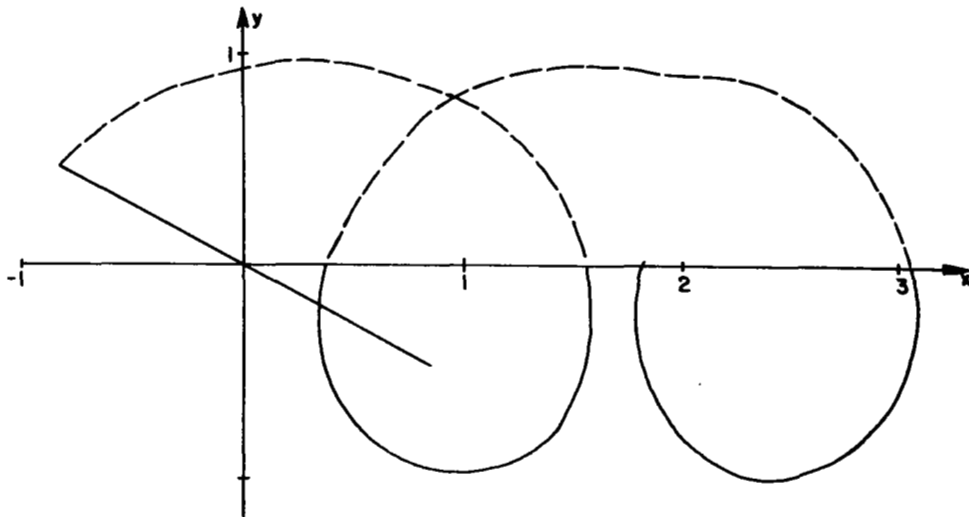


(b) side view

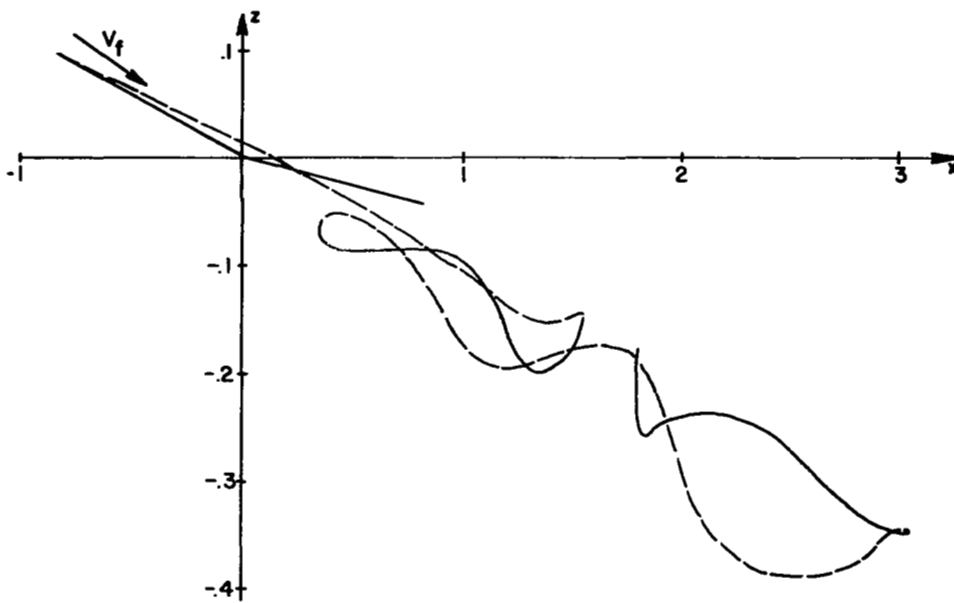


(c) rear view

Figure 25. Single two-bladed rotor's tip vortex locations, $\mu=0.141$, $\alpha_s=-5.1^\circ$



(a) plan view



(b) side view

Figure 26. Single two-bladed rotor's tip vortex location, $\mu=0.235$, $\alpha_s=-8.5^\circ$

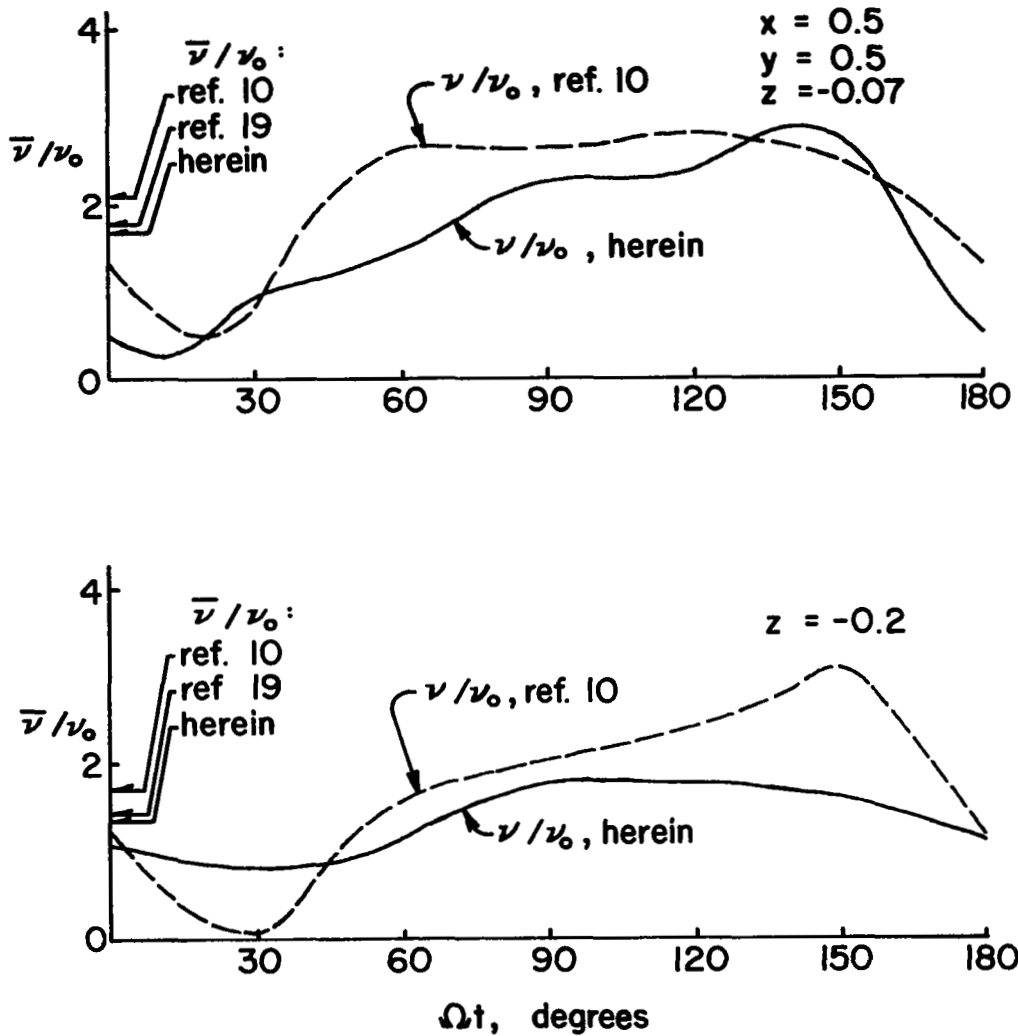


Figure 27. Computed induced downwash variation below the rotor plane

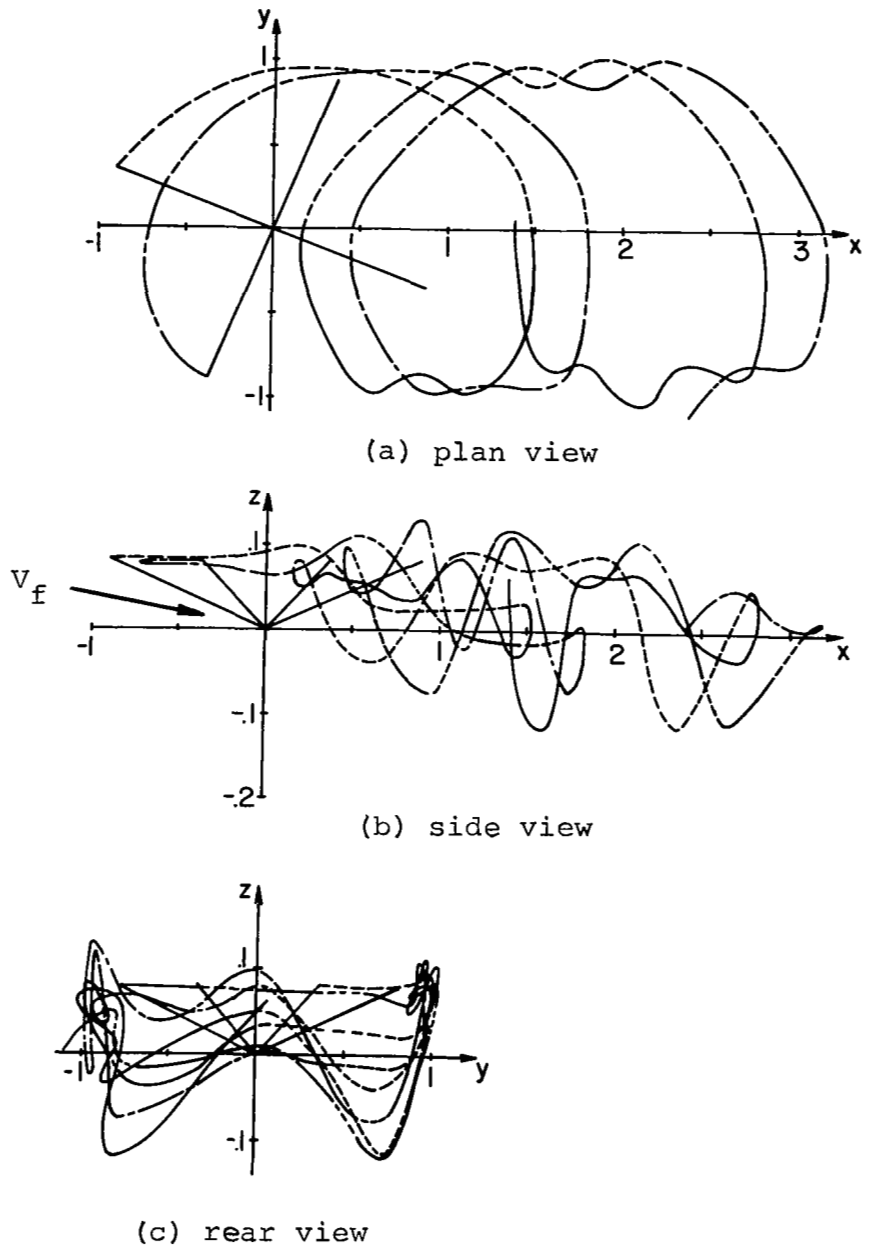
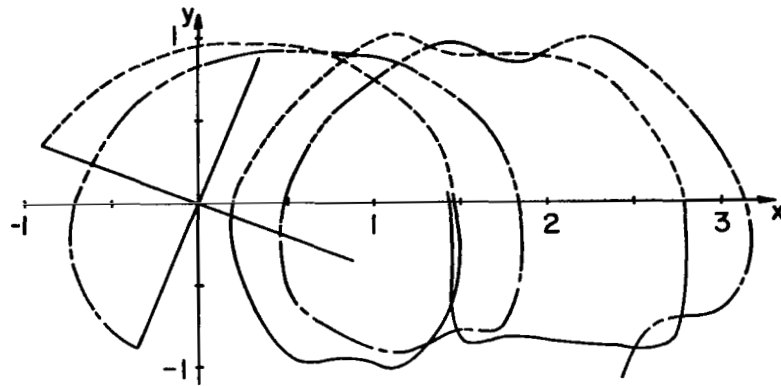
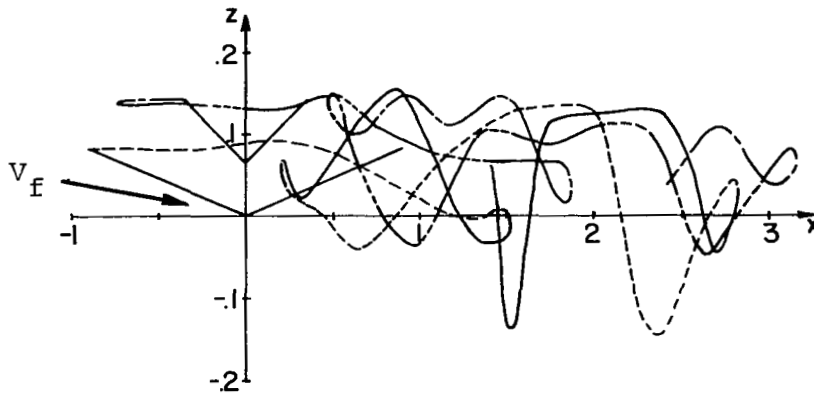


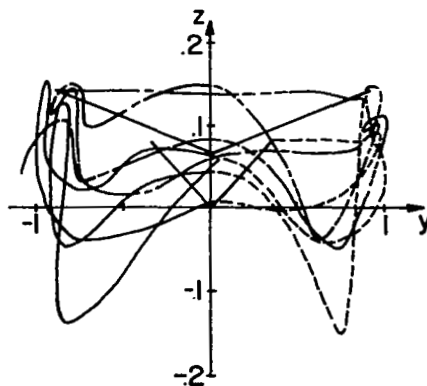
Figure 28. Two two-bladed rotors' tip vortex locations, $\mu=0.2$, $\Delta z/c=0$, $\Delta\psi=90^\circ$, $\alpha_s=-2.22^\circ$



(a) plan view



(b) side view



(c) rear view

Figure 29. Two two-bladed rotors' tip vortex locations, $\mu=0.2$, $\Delta z/c=1$, $\Delta\psi=90^\circ$, $\alpha_s=-2.22^\circ$

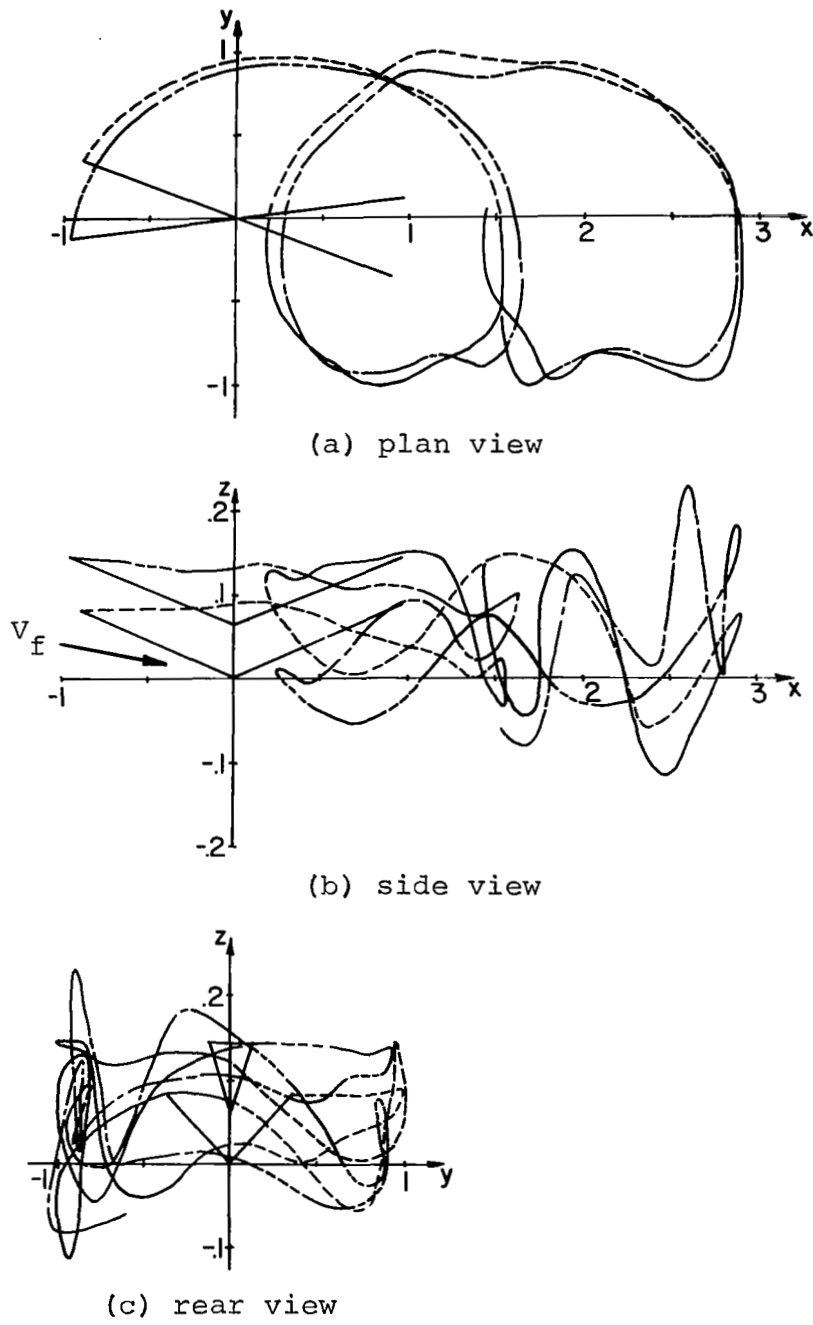
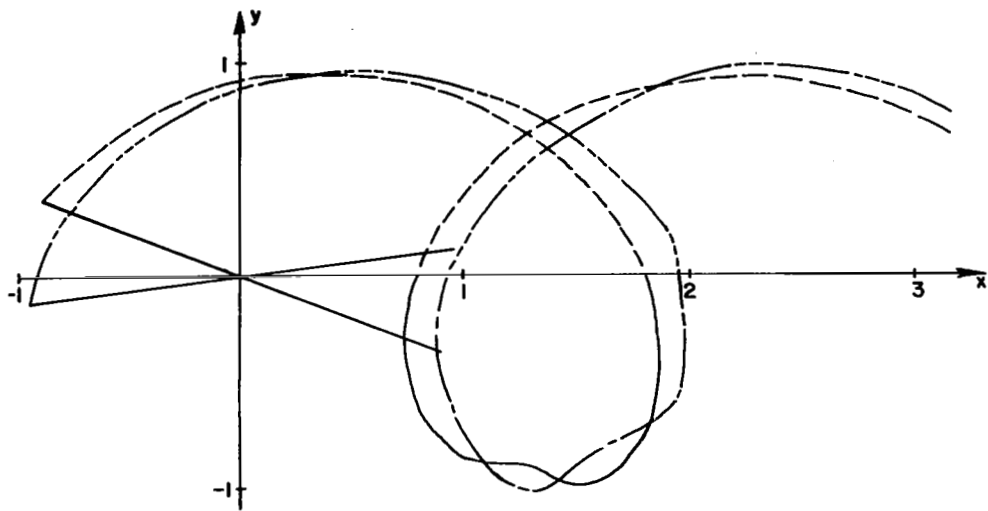
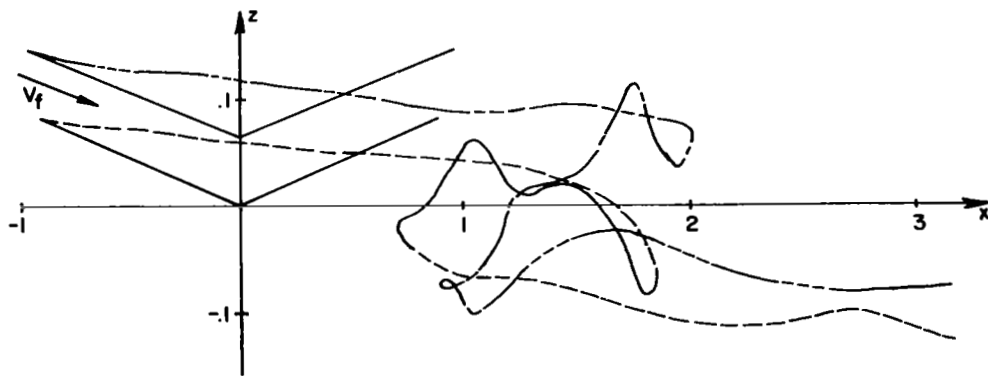


Figure 30. Two two-bladed rotors' tip vortex locations, $\mu=0.2$, $\Delta z/c=1$, $\Delta\psi=30^\circ$, $\alpha_s=-2.22^\circ$

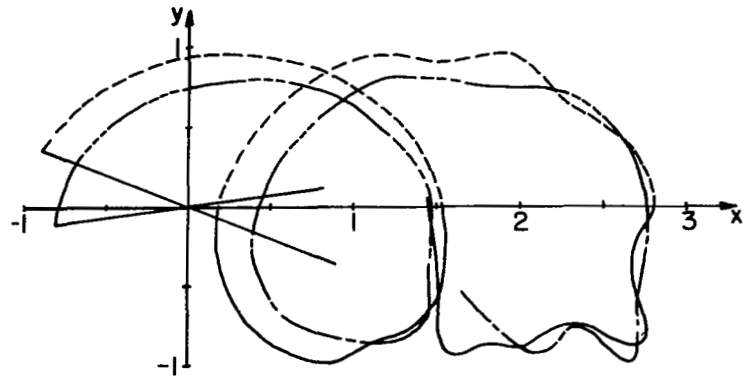


(a) plan view

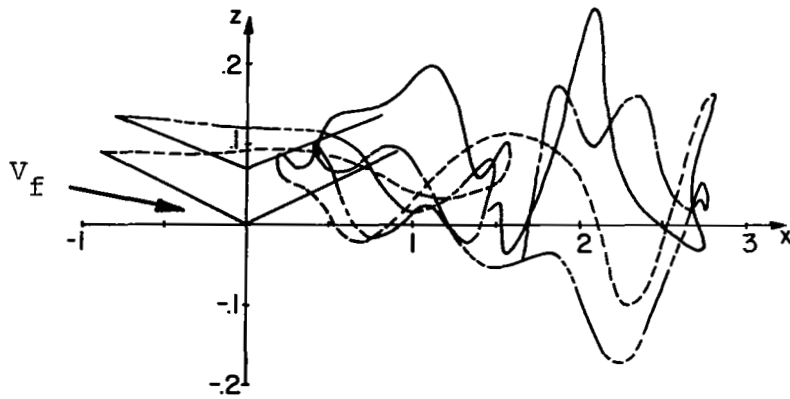


(b) side view

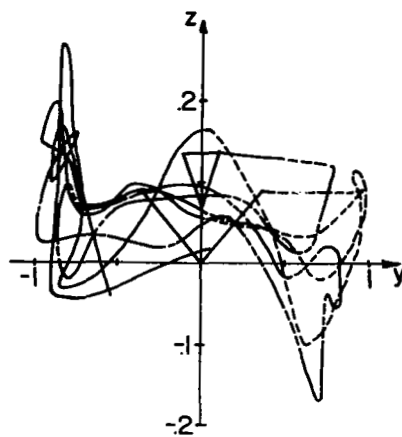
Figure 31. Two two-bladed rotors' tip vortex locations, $\mu=0.3$, $\Delta z/c=1$, $\Delta\psi=30^\circ$, $\alpha_s=-2.22^\circ$



(a) plan view

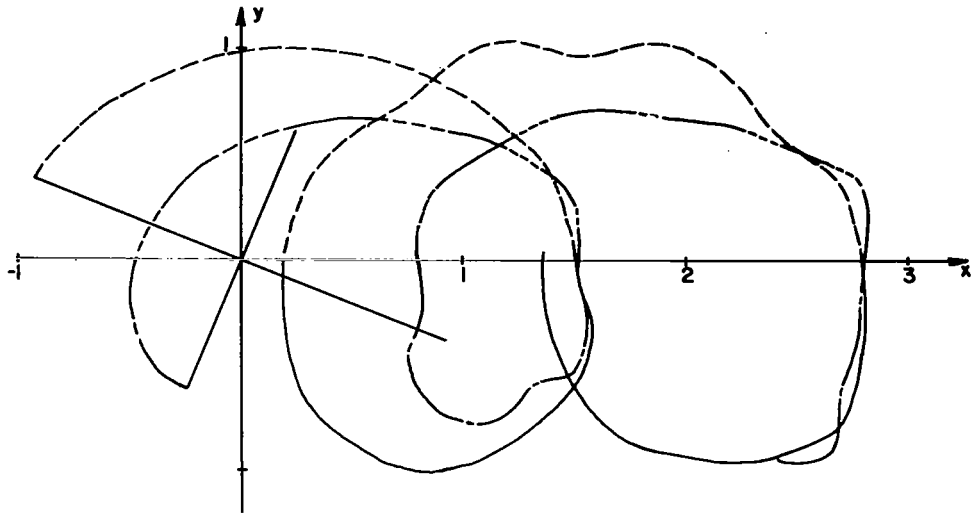


(b) side view

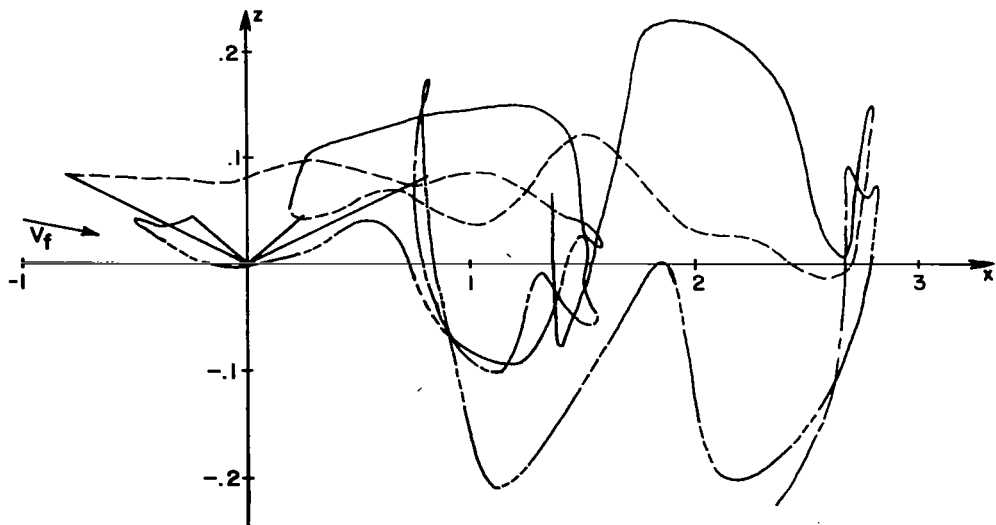


(c) rear view

Figure 32. Two two-bladed rotors' tip vortex locations, $\mu=0.2$, $\Delta z/c=1$, $\Delta\psi=30^\circ$, $\alpha_s=-2.22^\circ$, $R_2/R_1=0.85$

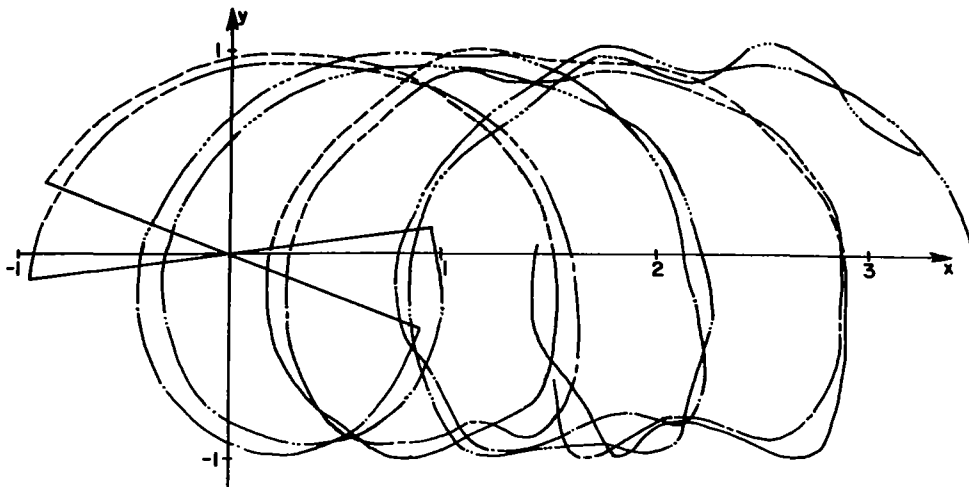


(a) plan view

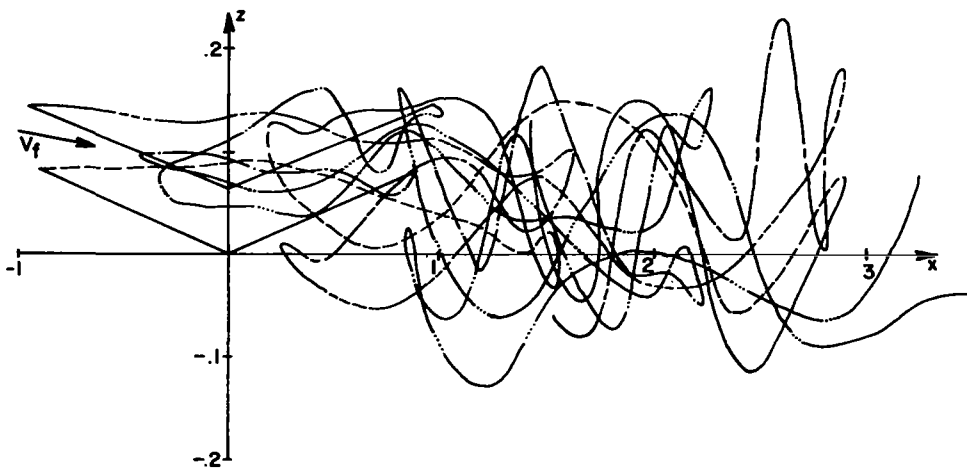


(b) side view

Figure 33. Two two-bladed rotors' tip vortex locations, $\mu=0.2$, $\Delta z/c=0$, $\Delta\psi=90^\circ$, $\alpha_s=-2.33^\circ$, $R_2/R_1=0.7$, rotor 1 cutout to $0.4 R_1$



(a) plan view



(b) side view

Figure 34. All tip vortex locations for two two-bladed rotors' tip vortex locations, $\mu=0.2$, $\Delta z/c=1$, $\Delta\psi=30^\circ$, $\alpha_s=-2.22^\circ$

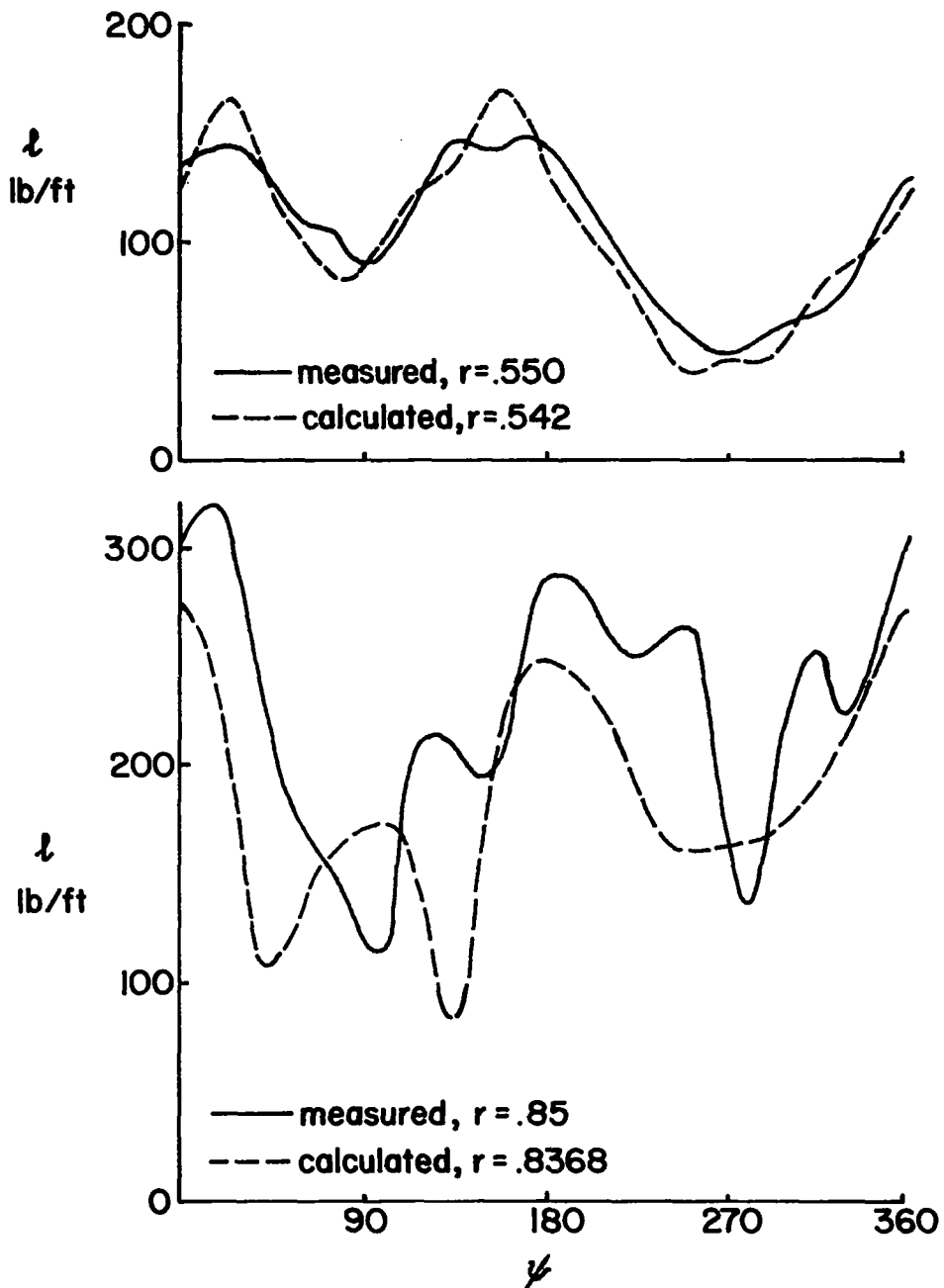


Figure 35. Blade airloads for H-34 helicopter, lb/ft versus azimuth, $\mu = 0.2$

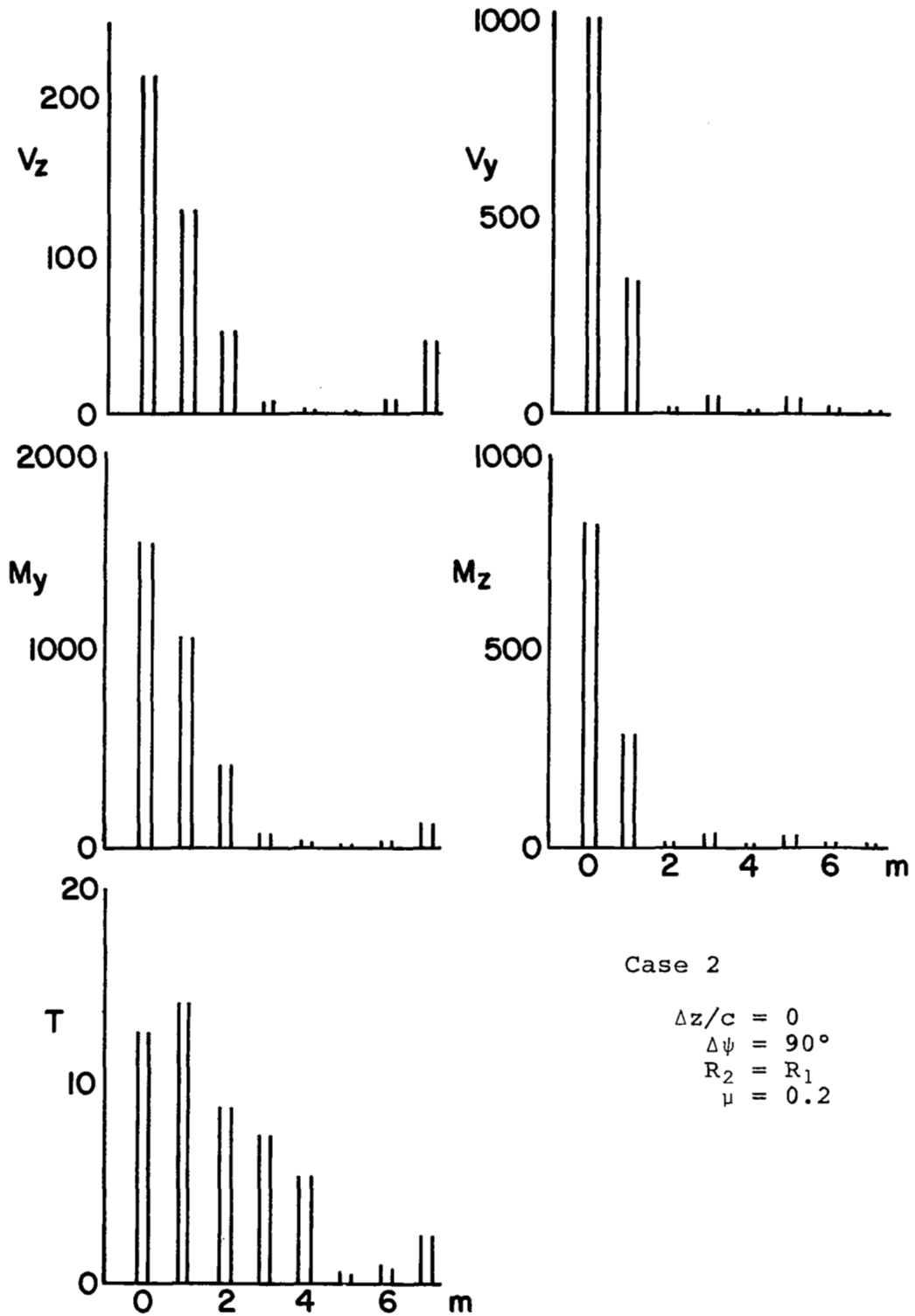


Figure 36. Blade shear and moment magnitudes versus harmonic number, m , for Case 2

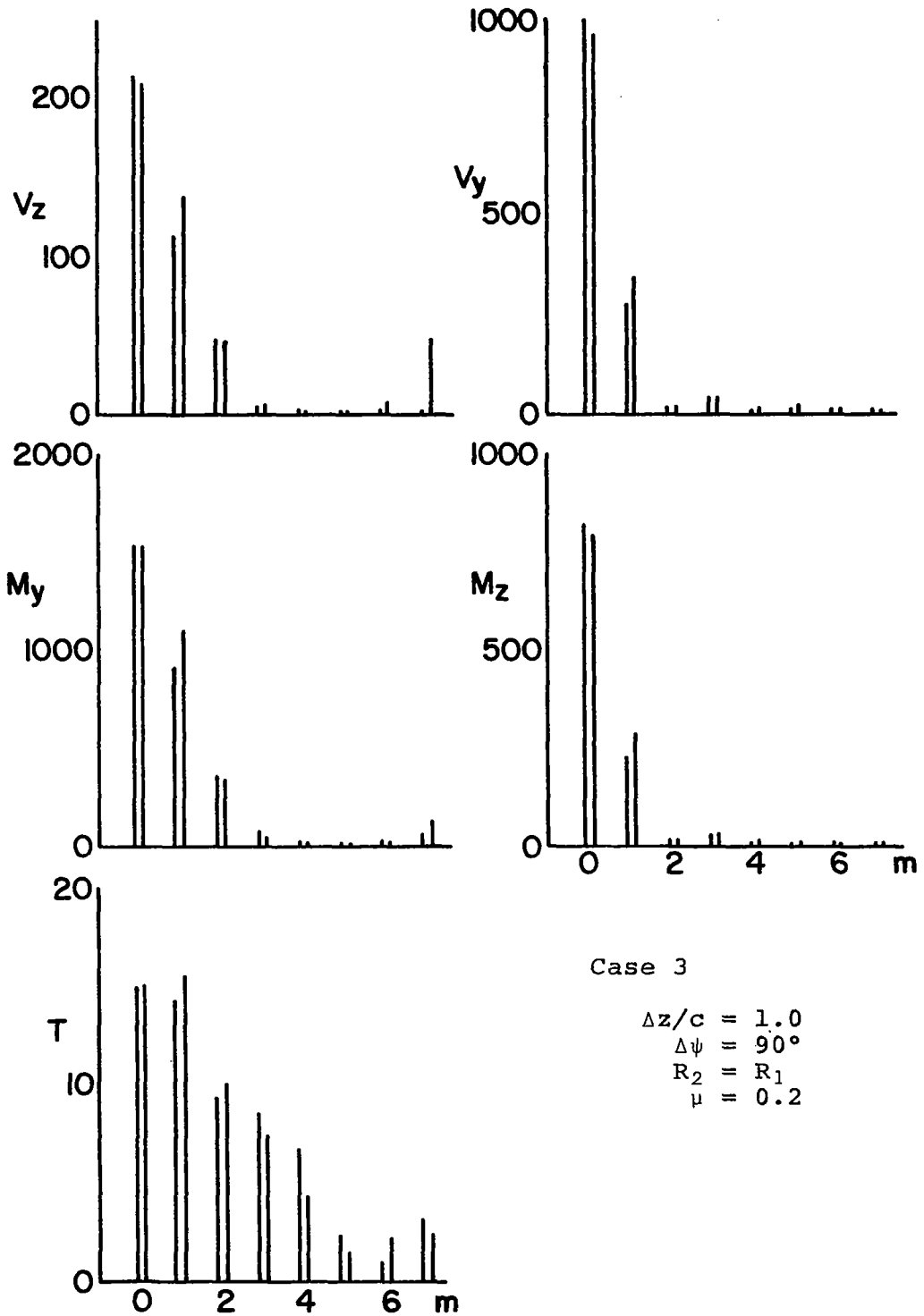


Figure 37. Blade shear and moment magnitudes versus harmonic number, m , for Case 3

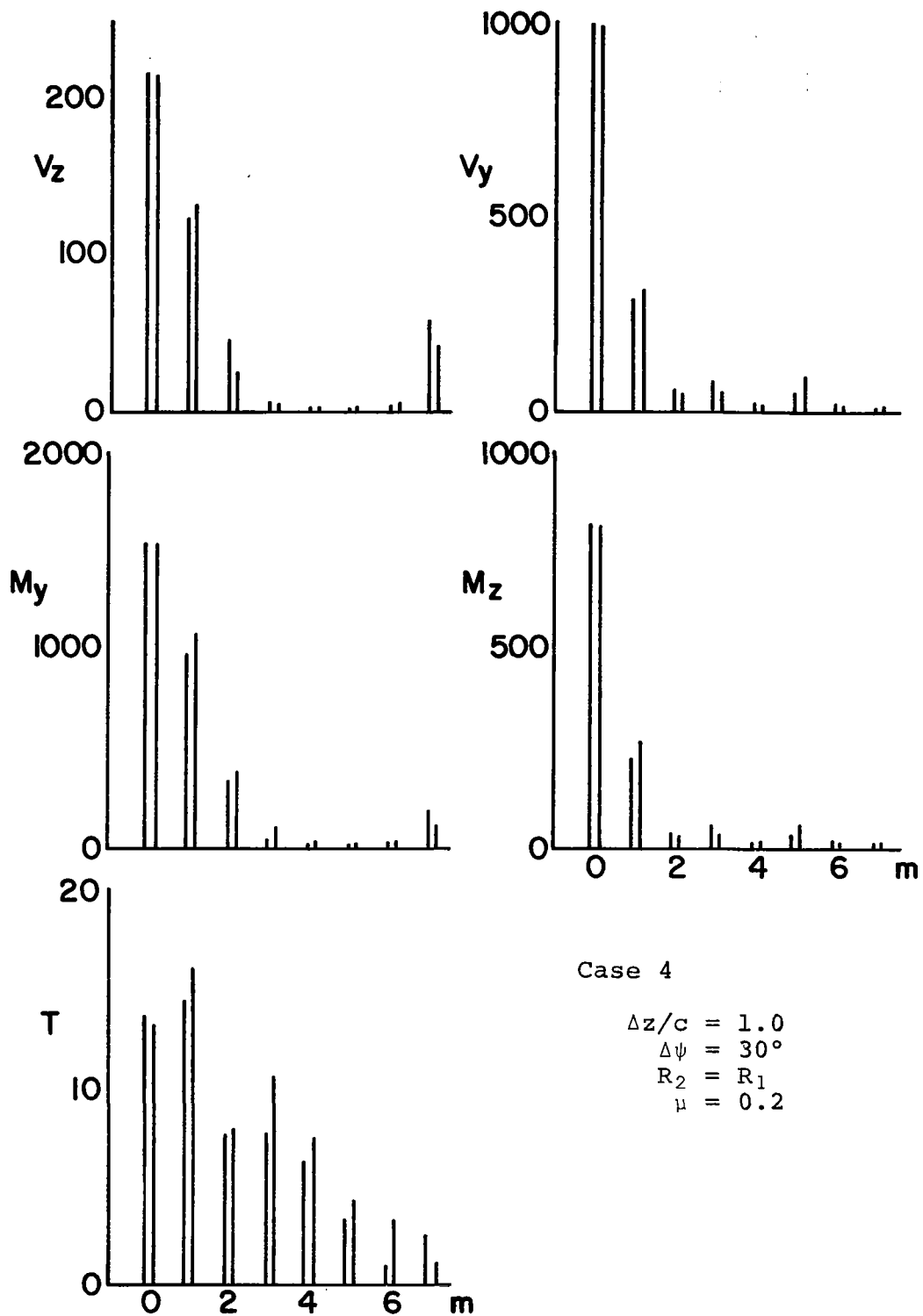


Figure 38. Blade shear and moment magnitudes versus harmonic number, m, for Case 4

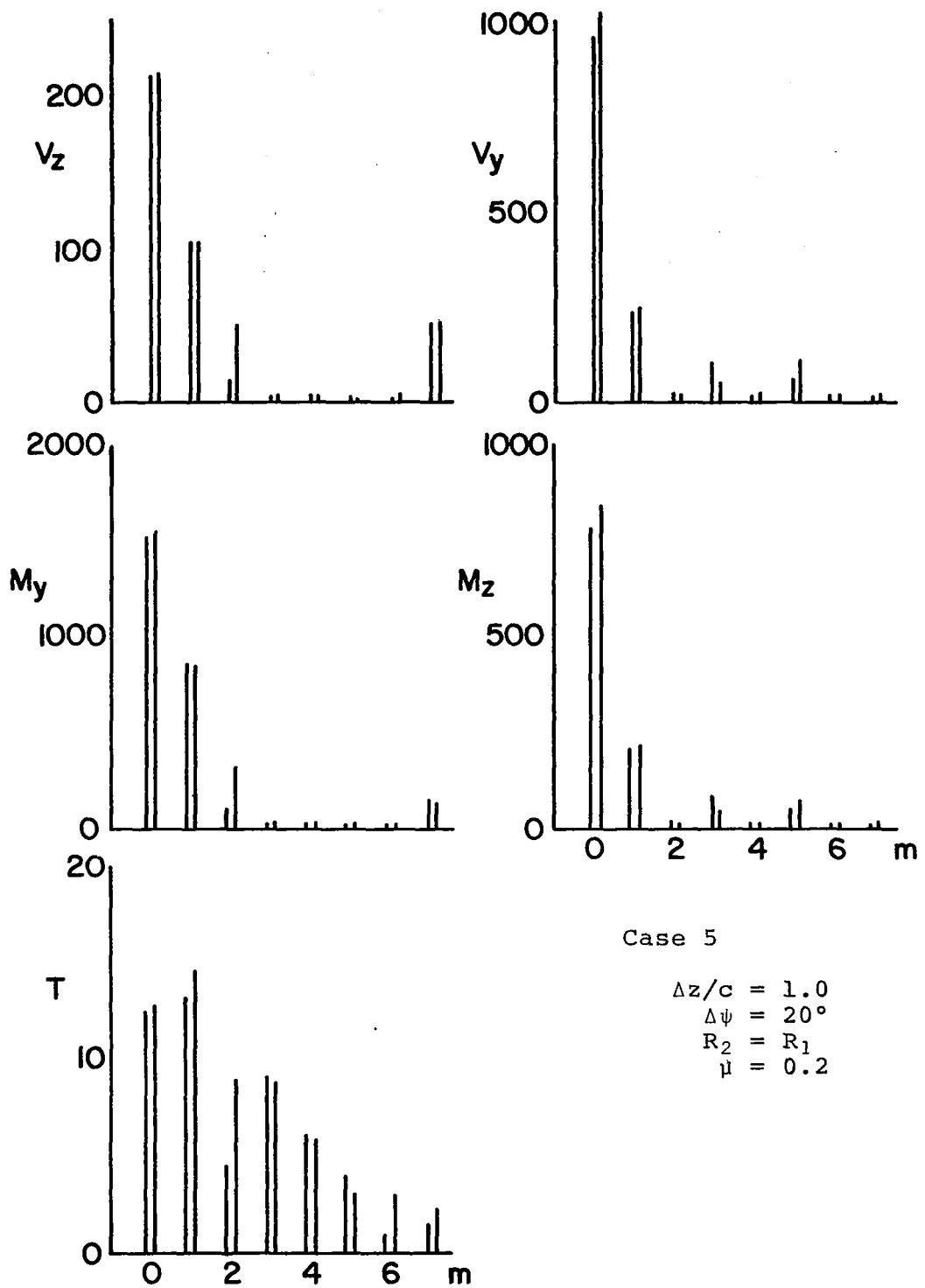


Figure 39. Blade shear and moment magnitudes versus harmonic number, m , for Case 5

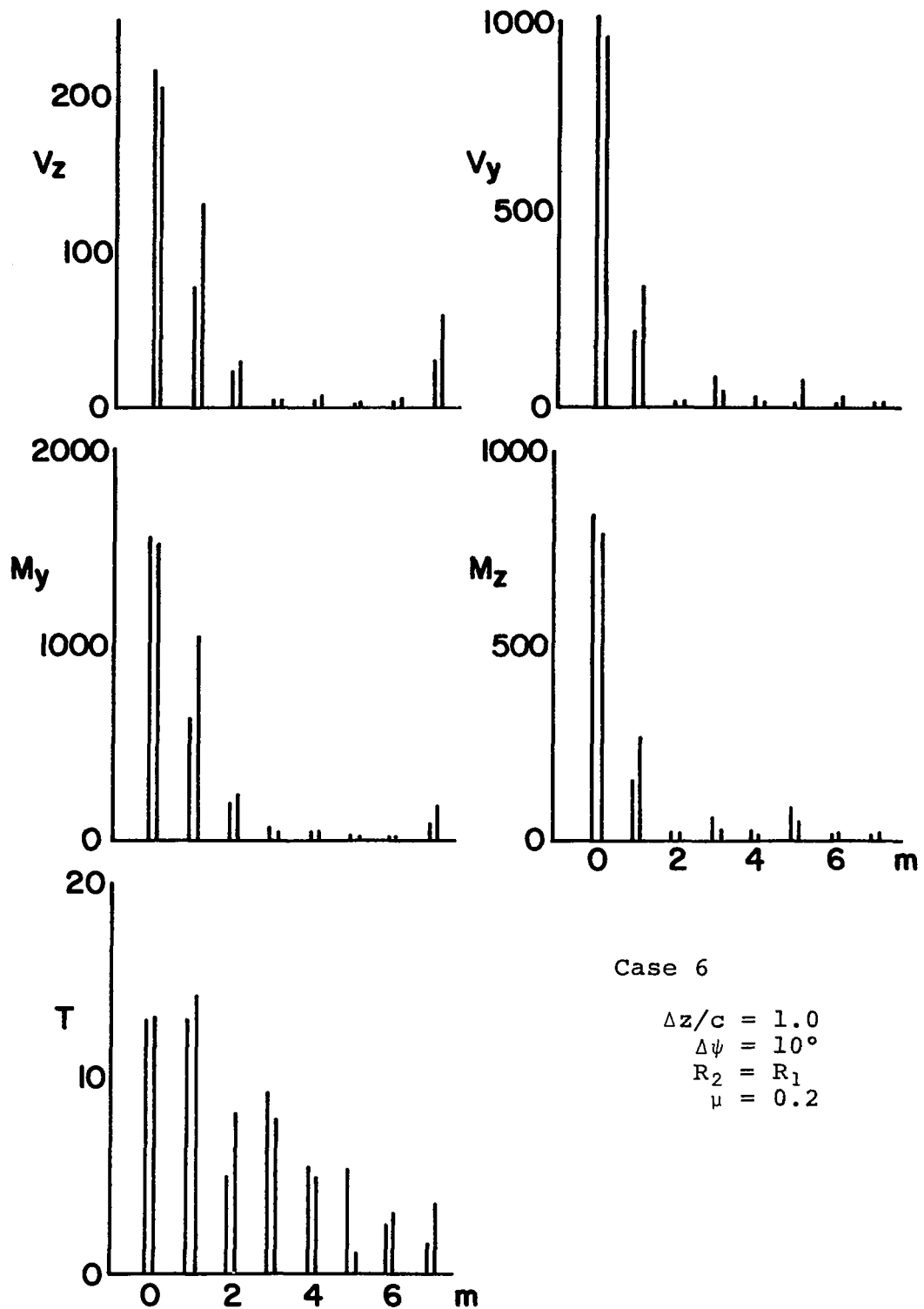


Figure 40. Blade shear and moment magnitudes versus harmonic number, m , for Case 6

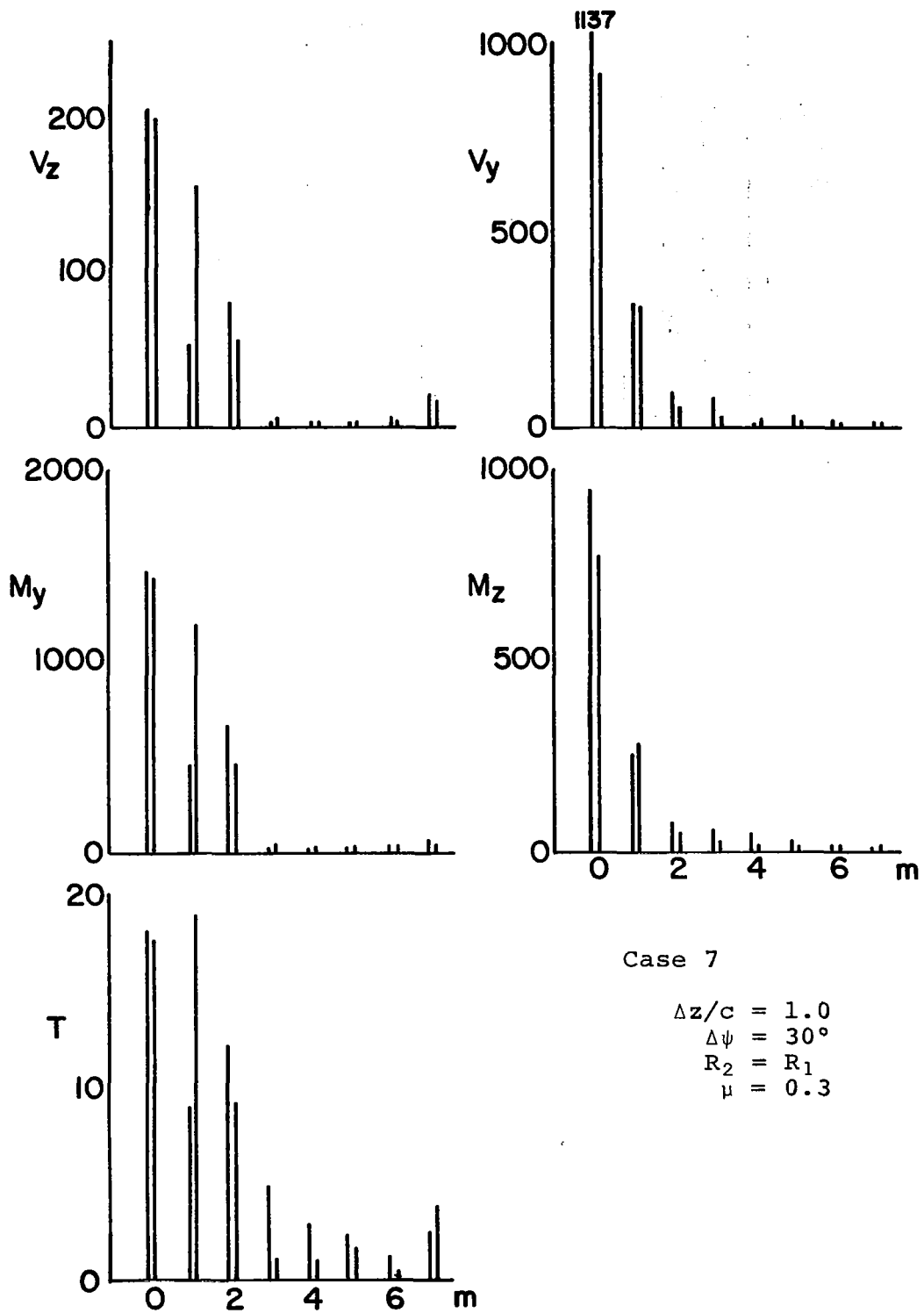


Figure 41. Blade shear and moment magnitudes versus harmonic number, m , for Case 7

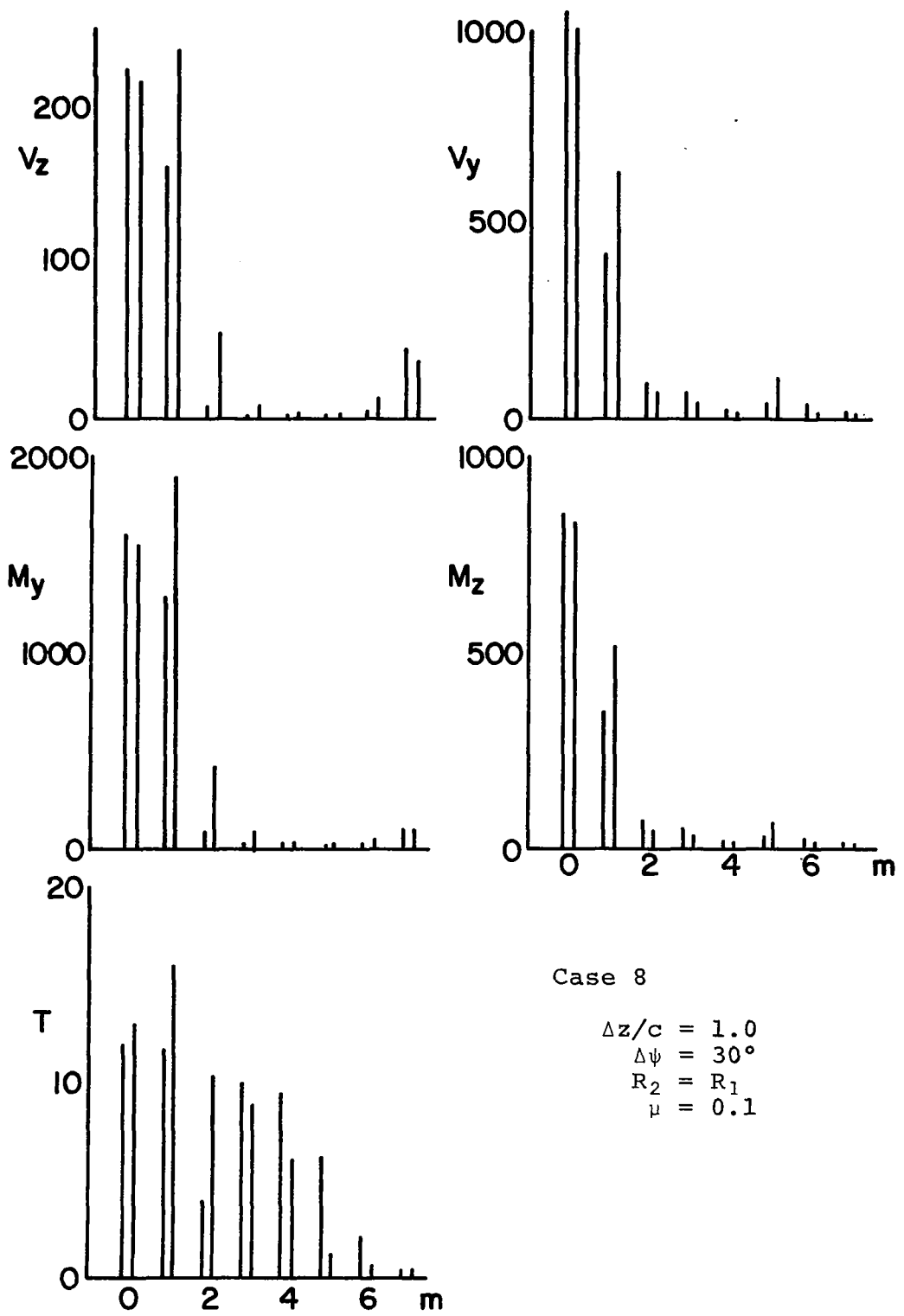


Figure 42. Blade shear and moment magnitudes versus harmonic number, m, for Case 8

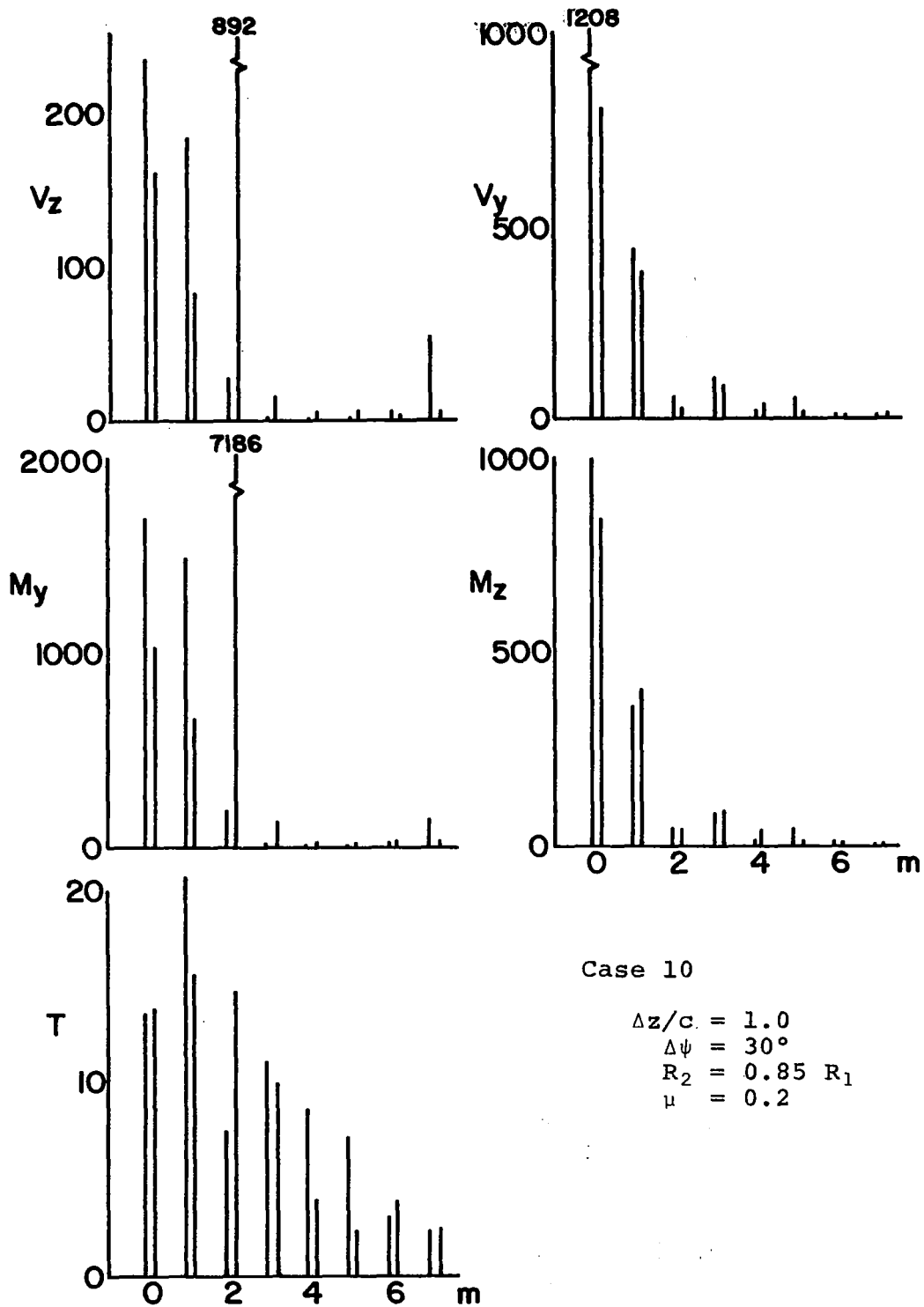


Figure 43. Blade shear and moment magnitudes versus harmonic number, m , for Case 10

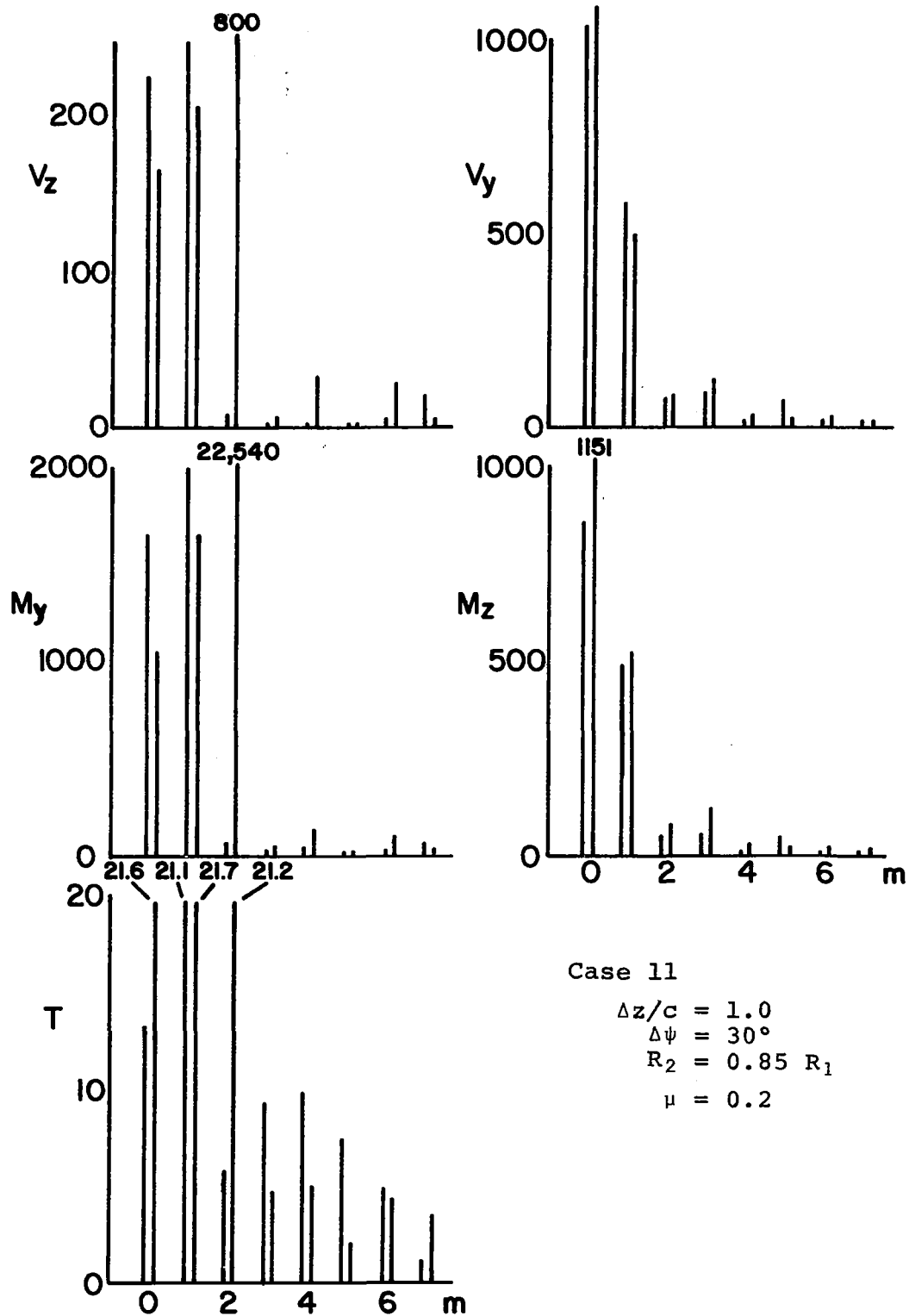


Figure 44. Blade shear and moment magnitudes versus harmonic number, m , for Case 11

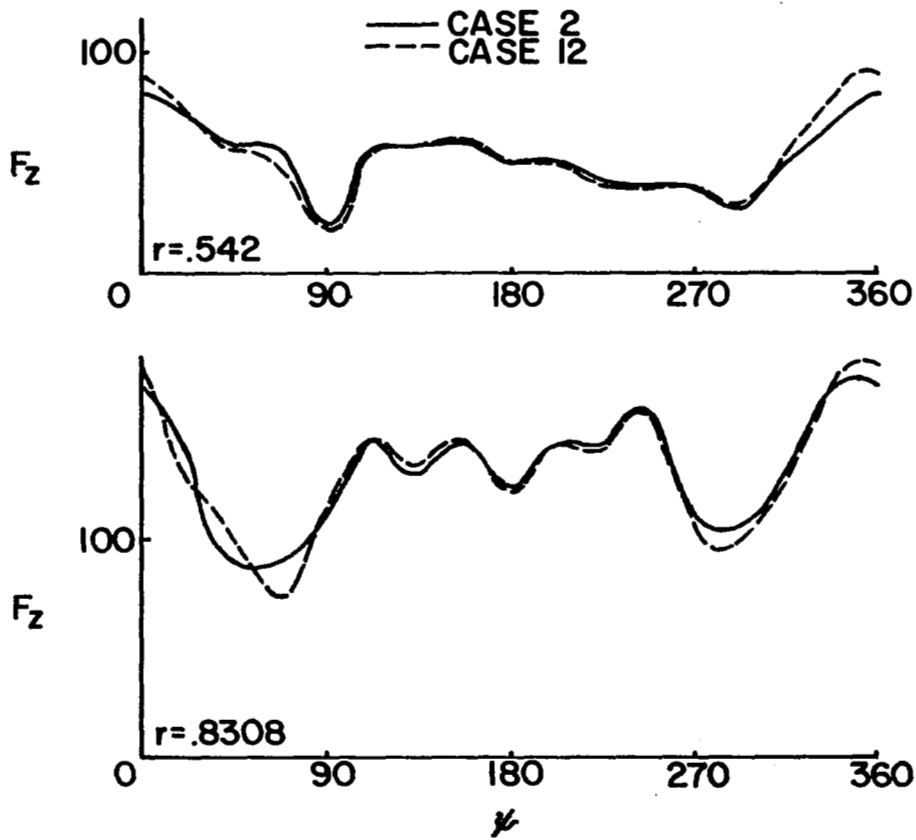


Figure 45. Airloads without and with blade motion effects in wake-induced velocity calculations, $\mu=0.2$

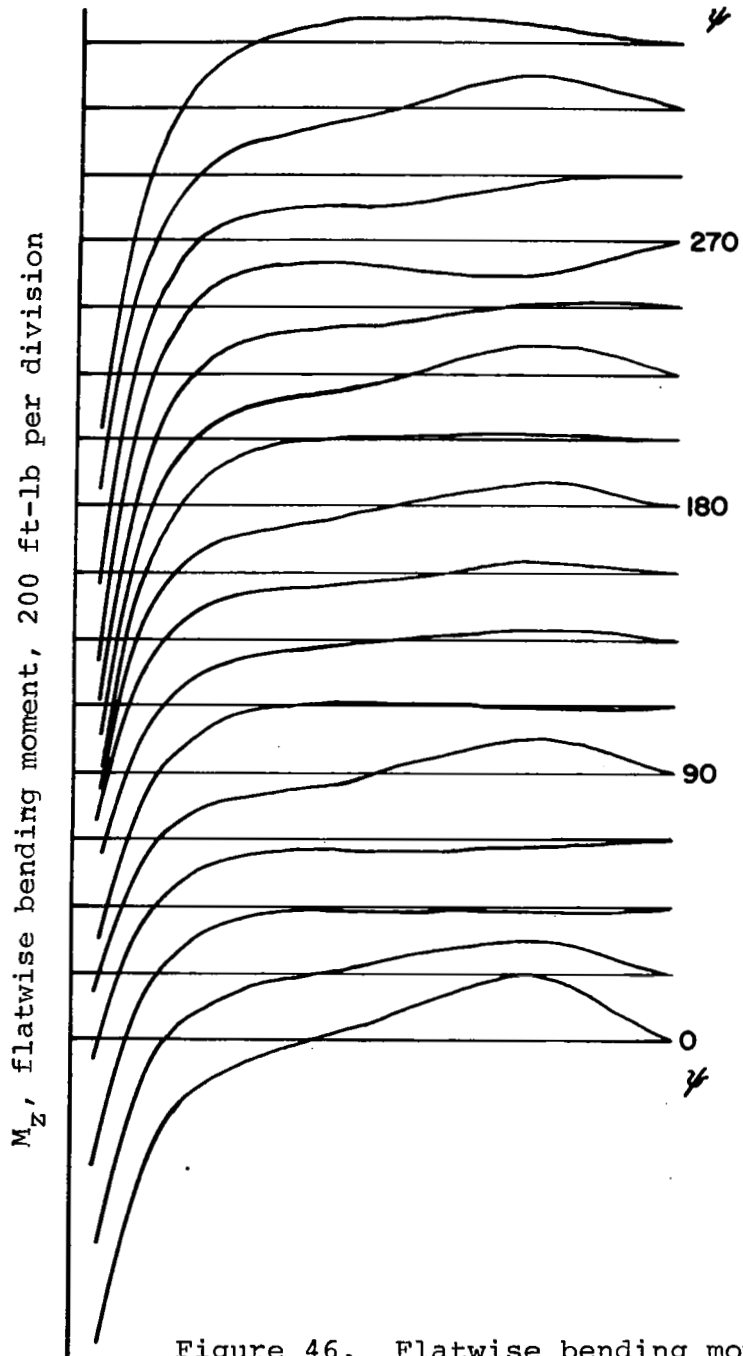


Figure 46. Flatwise bending moment, M_z , radial distributions versus azimuth for Case 2, rotors 1 and 2; $\mu=0.2$

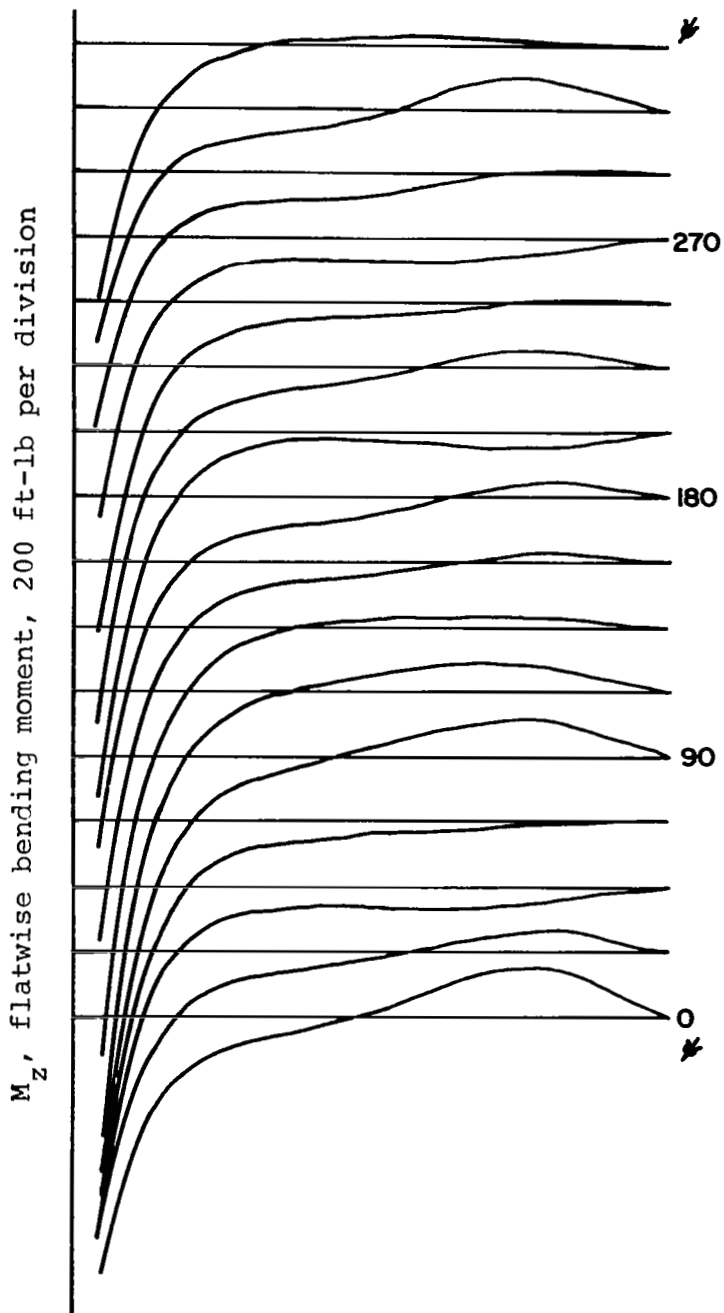


Figure 47. Flatwise bending moment, M_z , radial distributions versus azimuth for Case 7, rotor 1; $\mu=0.2$